ANALYSIS AND DESIGN OF A HIGH TEMPERATURE LIQUID METAL SOLAR THERMAL RECEIVER

A Thesis
Presented to
The Academic Faculty

by

Alfred DeAngelis

In Partial Fulfillment
of the Requirements for the Degree
Master of Science in Mechanical Engineering in the
School of George W. Woodruff School of Mechanical Engineering

Georgia Institute of Technology
May 2016

ANALYSIS AND DESIGN OF A HIGH-TEMPERATURE LIQUID METAL SOLAR THERMAL RECEIVER

Approved by:

Dr. Asegun Henry, Advisor
School of Mechanical Engineering
Georgia Institute of Technology

Dr. Shannon Yee
School of Mechanical Engineering
Georgia Institute of Technology

Dr. Samuel Graham
School of Mechanical Engineering
Georgia Institute of Technology

Date Approved: 27 April 2016

ACKNOWLEDGEMENTS

First and foremost, I would like to thank my parents for constantly supporting my development and maturation in an academic environment and, more importantly, in life. They along with my siblings are of invaluable significance on me, and I cannot overstate how appreciative I am for all four of them. I am incredibly grateful to have grown up with such a caring, loving family.

Second, I would like to thank my advisor, Dr. Asegun Henry. He is a source of knowledge not only on technical subjects, but professional ones as well. His expertise has been of immense benefit to me during my time at Georgia Tech. Dr. Henry is someone whom I look up to and aspire to be like.

Third, I would like to thank the many educators who have helped me along the way. Through their expertise in fields ranging from heat transfer to film studies, material science to philosophy, they have truly made me both a better-rounded engineer, and a better informed and more capable individual.

I would also be remiss not to mention the support of the many friends I have made over the years who have been such a positive influence in my life. Though too numerous to list individually, their encouragement is a source of inspiration and drives me to continuously push myself.

Finally, I would like to acknowledge two sources of funding that have afforded me the opportunity to research a subject about which I am quite passionate. The project on which I have worked is sponsored by APRA-E, Project No. DE-AR0000339. This

material is also based upon work supported by the National Science Foundation Graduate Research Fellowship under Grant No. DGE-1148903.

Freddy

TABLE OF CONTENTS

LIST OF TABLES

Page

LIST OF FIGURES

Page

LIST OF SYMBOLS

A	Area (m^2)
Br	Brinkman number
C	Material Compliance (1/Pa) Constant Used to Relate Mass to Mass Flowrate (s^2/kg)
C_{max}	Maximum Concentration
C_p	Heat Capacity (J/kg-K)
D	Diameter (m)
E	Young's Modulus (Pa)
g	Gravitational Constant (=9.81 m/s^2 at sea level at the equator)
g_z	Gravitational Constant in the z-direction (m/s^2)
h	Convective Heat Transfer Coefficient (W/m^2-K) Height (m)
h_{rad}	Radiative Heat Transfer Coefficient (W/m^2-K)
k	Thermal Conductivity (W/m-K)
L	Length (m)
m	Mass (kg)
$\dot{m}$	Mass Flowrate (kg/s)
n	Refractive Index
P_{O_2}	Partial Pressure of Oxygen (atm)
P	Pressure (Pa)
q''	Heat Flux (W/m^2)
q''_{rad}	Radiative Heat Flux (W/m^2)
R	Thermal Resistance (K/W)

r	Radial Position (m) Radius (m)
T	Temperature (K or °C)
t	Time (s)
U	Fluid Velocity Magnitude (m/s)
u	Velocity in *x*-direction (m/s) Displacement (m)
u_r	Velocity in *r*-direction (m/s)
u_z	Velocity in *z*-direction (m/s)
v	Velocity in *y*-direction (m/s)
w	Velocity in *z*-direction (m/s)
α	Coefficient of Thermal Expansion (1/K)
ε	Surface Emissivity Total Strain
$\varepsilon_{effective}$	Effective Emissivity
ε_{el}	Elastic Strain
ε_{th}	Thermal Strain
η	Efficiency
θ	Angle (rad) Non-dimensionalized Temperature
μ	Viscosity (kg/m-s)
ρ	Density (kg/m^3)
σ	Stefan-Boltzmann Constant (=5.67×10^{-8} $W/m^2\text{-}K^4$) Total Stress (Pa)
σ_t	Tensile Strength (Pa)
ϕ	Luminous Flux

LIST OF ABBREVIATIONS

AR	Anti-Reflection
CAD	Computer Aided Design
CFD	Computational Fluid Dynamics
CNC	Computer Numeric Control
CPC	Compound Parabolic Concentrator
CSP	Concentrated Solar Power
DAQ	Data Acquisition
DNI	Direct Normal Insolation
EM	Electromagnetic
HFSS	High Flux Solar Simulator
HTF	Heat Transfer Fluid
LCOE	Levelized Cost of Electricity
LMHTF	Liquid Metal Heat Transfer Fluid
MSF	Mechanical Support Frame
MCRT	Monte Carlo Ray Tracing
PV	Photovoltaic
TES	Thermal Energy Storage
TIR	Total Internal Reflection
USC	Ultra Supercritical
YSZ	Yttria-Stabilized Zirconia
ZTA	Zirconia-Toughened Alumina

CHAPTER1: INTRODUCTION

Background

Motivation for Improving Current Concentrated Solar Power

With the threat of climate change becoming an ever more pressing concern[1], carbon-neutral energy solutions are becoming an increasingly critical means of electricity production. Concentrated solar power (CSP) is a method of solar to electrical power conversion that uses concentrated sunlight to heat a material and then produce energy from that heat. Of the various CSP plant configurations, power-tower plants have the best potential for cost reduction, as these plants can reach higher operating temperatures than other configurations, thereby improving their efficiency[2].

Power-tower plants are composed of either three or four main components: heliostats, a tower based receiver, in some cases thermal storage, and a power block. The tower, storage tanks, and power block are generally located in close proximity and are surrounded by a field of 2-axis, sun-tracking mirrors termed heliostats. These four components can be seen in Figure 1.

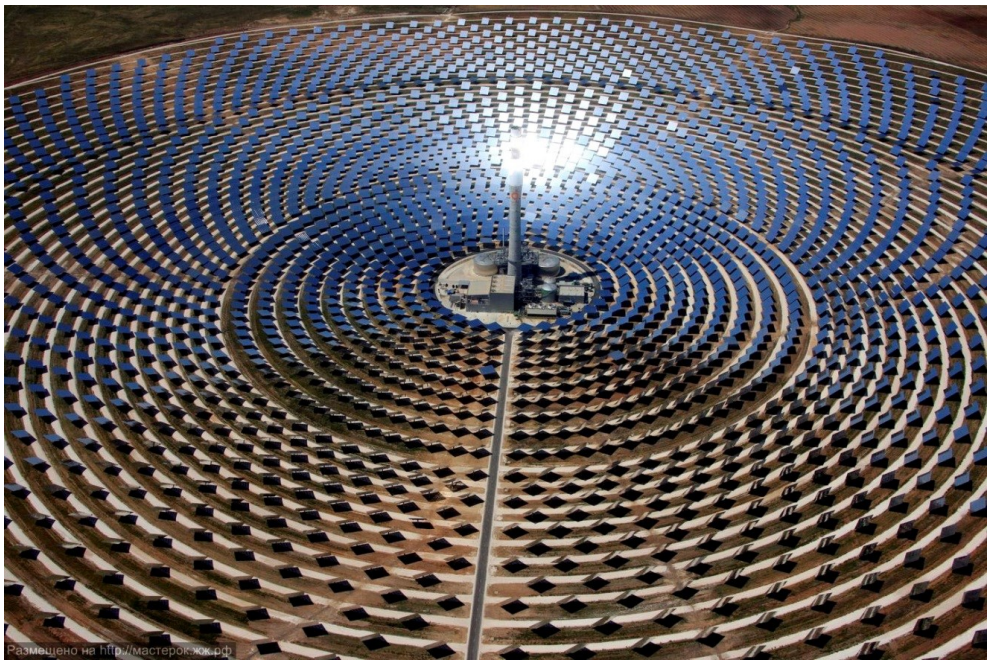

Figure 1. View of the Crescent Dunes plant[3]. The tower is visible at the center of the heliostat field. At the tower's base are two thermal storage tanks and the power block.

To convert sunlight to electricity, the heliostats first concentrate sunlight onto a solar receiver located at the top of the tower. The receiver absorbs the sunlight, converting it to heat, and the heat is transferred to a heat transfer fluid (HTF). The HTF is then either passed directly through the power block or through a heat exchanger, which in turn heats a working fluid that flows through the power block, converting the heat to work. The power block typically consists of steam based Rankine cycle turbines, similar to those used in coal or nuclear plants. The primary HTF can also be stored in thermal storage tanks and used at a later time, allowing the plant to produce electricity even if no sunlight is currently available.

Over the past few year, photovoltaics (PV) have proliferated due to the rapidly decreasing cost of manufacturing panels and the increase in panel efficiency[4,5]. As PV becomes cheaper and more efficient, CSP has become a less cost competitive means of solar power generation. However, CSP is not without its merits. Chief among them is that

CSP with integrated thermal energy storage (TES) allows for easily dispatchable production of energy, i.e. electricity generation even when the sun is not shining. PV can incorporate storage by using electrochemical batteries, but these batteries increase the system cost of PV to the point where it is no longer cost-competitive with CSP + TES[6,7]. However, once PV starts to comprise a significant percentage of a utility's generation portfolio, if storage is not incorporated, the utility cannot fully utilize the energy produced by PV[8,9]. Given a constant baseload from electricity sources such as coal and nuclear power, during the daytime, solar panels can produce additional electricity to the point that supply temporarily exceeds demand. In this case, utilities must curtail some of the electricity the solar panels have produced. On the other hand, even at high market penetration, significant reduction in solar curtailment rates can be realized when CSP with TES is used alongside PV to generate electricity as compared to when solar energy is harvested without TES[10]. These reductions in curtailment rates result in a higher fraction of useable solar energy for a given energy production capacity, thereby reducing the levelized cost of electricity (LCOE) of both PV and CSP. However, within the United States, even subsidized CSP is only cost competitive with traditional fuel sources in regions with high direct normal insolation (DNI)[11,12], typically located in the southwest portion of the country[13]. Thus, reducing the cost of CSP could potentially alter the energy sector, not only because it would result in CSP reaching cost-parity with other sources of energy, but also because it would allow further market penetration of intermittent energy sources such as PV.

There exist several avenues to reduce CSP costs[2], but one of the most effective ways is to improve the plant efficiency, as LCOE scales with the inverse of the net

system efficiency. Producing more electricity for the same capital cost is one of the most effective approaches to reducing LCOE, because it reduces every component's cost. When comparing the efficiency of different components in the plant, the biggest source of inefficiency in a CSP plant is the conversion of heat to electricity in the power block, which is limited by the second law of thermodynamics[14]. Thus, one of the only ways to dramatically improve the system efficiency is to operate at higher temperatures, so that the heat engine can operate more efficiently. The work in this thesis is focused specifically on the goal of raising the operating temperature of a CSP plant to temperatures in excess of 1,000°C. Doing so leads to a marked increase in thermodynamic efficiency of the power block, as operating temperatures above 1,000°C allow for a combined Brayton-Rankine cycle to be employed [15]. Current CSP plants are limited to 565°C and must therefore operate using a less efficient Rankine power cycle[16-19]. The thermal to electric efficiency of a Rankine cycle at these temperatures is limited to ~40%[20,21], while the efficiency of a Brayton-Rankine cycle run at temperatures in excess of 1,000°C can be as high as 60.1%[22]. The current limitation on operating temperature is due primarily to two issues: (1) stability limitations of the HTF and chemical compatibility issues with associated containment materials, and (2) limitations due to increased heat loss from the system, particularly from the receiver. Avenues for addressing both issues are discussed in the following chapters.

Ongoing Attempts to Achieve Higher Operating Temperatures

Finding a suitable HTF to use in a CSP plant operating at extreme temperatures (>1,000°C) is difficult for a number of reasons. Several media are being researched as high-temperature HTF's, such as molten salt, air, steam, and solid particles[15], but they

all have drawbacks that constrain the maximum temperatures to well below 1,000°C. In the few instances where a temperature in excess of 1,000°C is obtained, the receiver efficiency is so low that it offset any gains that would be realized in the power block, or the receiver relies on expensive, exotic materials.

Molten salt, typically a mixture of $NaNO_3$, KNO_3, and other nitrates[23,24], has been adopted as a HTF for use in CSP, particularly for plants with thermal storage such as Crescent Dunes and Gemasolar[25]. However, these salts are quickly corrode stainless steels above 565°C[23] at which point chromium diffuses from the surface of the steel to grain boundaries, no longer protecting the steel from attack by the salt. The salts themselves are also only stable up to 600°C before they begin to convert from nitrates to nitrites[26], though ongoing efforts exist to develop salts that can be used at 700°C[16]. Fluoride salts are another option, but they are corrosive to almost all metals, other than relatively expensive nickel alloys[27-29]. These salts can be used at temperatures up to 1,000°C[30], but the cost of the containment materials, as well as the salts themselves, make them impractical for use at a utility scale[31].

Direct steam generation is another option for power production and is well known as the technology used by the Ivanpah plant, which is currently the largest power tower CSP plant in the world[32]. However, steam is a poor candidate for reaching temperatures above ~600°C[33,34]; at such temperatures, supercritical steam requires expensive nickel alloys[35] due to significant corrosion/erosion of steel turbine blades[36]. Furthermore, thermal storage of a gas phase requires unreasonably large volumes, due to its 10-1,000 x lower density than condensed phases (i.e. a liquid or gas).

Though it suffers from the same issue of low energy density as steam, air has also been considered as another option for a high temperature HTF. In addition to its low density, air has the lowest thermal conductivity of any of the aforementioned HTF's. This low conductivity in combination with air's increase in viscosity at higher temperatures can lead to stagnation zones, which in turn results in regions of the receiver that are significantly hotter than the bulk of the receiver, i.e. "hot spots"[37,38]. Simulations of these receivers have demonstrated that, if not appropriately addressed, such hot spots can potentially lead to runaway temperatures and failure of the receiver[39-41]. Nonetheless, air based receivers have attained some of the highest temperatures of any CSP receiver so far. Karni *et al.*[42] designed a receiver termed the "DIAPR" which was able to reach efficiencies of 79% with an exit temperature of ~1,200°C. However, this receiver relied on a design that used a secondary concentrator to increase concentration from 300 to 10,000 suns[43]. Achieving such high concentrations requires highly columnated light with a maximum angular spread of 12°[43]. Furthermore, the secondary concentrator is itself only ~90% efficient[43], leading to an overall receiver efficiency of 71%. In a separate set of experiments, Karni *et al.*[44] created a "Porcupine" receiver, which reached outlet temperatures of 830°C with 87% efficiency. Though these results are promising, the peak temperature was still below 1,000°C. Kribus *et al.*[40] were able to reach a temperature of 1,000°C using an air-based receiver, but they were unable to measure the receiver efficiency. More recently, Hischier *et al.*[45] simulated an air-based receiver that operates with 78% efficiency at 1,000°C. Nonetheless, such receivers fail to attain a temperature >1,000°C at an efficiency of >80%, making them unsuitable for use in an industrial application.

Falling particle receivers are currently one of the most promising options for exceeding 1,000°C. In these designs, ceramic particles are heated as they fall down a tower. The use of ceramics allows extreme temperatures to be reached without decomposition or chemical incompatibility of the HTF. Furthermore, the fact that the particles are solid allows for efficient thermal storage compared to gaseous HTFs. However, there do exist drawbacks to falling particle receivers. In particular, convective and radiative losses tend to be high in falling particle receivers, due to the high surface area to volume ratios of the particles, which is in turn due to their small size. For this reason, heat transfer to the particles at concentrations necessary to achieve extreme temperatures has proven to be difficult[37]. Furthermore, since the particles are typically not actively driven to flow at a certain speed and instead gravity is used, it may be difficult to achieve high receiver efficiencies below the peak solar input (e.g., low efficiency upon high turn-down ratio). For fluid based receivers, driven by a pump, such a penalty is much less significant, because one can simply flow the fluid at a slower rate to match the reduced incident light, while maintaining high receiver efficiency. However, for a solid particle based system with only a single constant driving force for the flow (e.g., gravity), achieving such flexibility may become problematic. Nonetheless, Siegel *et al.* tested a falling particle receiver *in situ*, but it was not optimized for the solar receiver used, and efficiencies were <70% at an exit temperature below 900°C[46]. One very promising result was obtained by Bertocchi *et al.*[47], who attained an operating temperature of 1,483°C with an efficiency of 88.5%. However, the particles used in the receiver were high-purity (99.8%), carbon nanoparticles with a diameter less than 600 nm[47]. Simply producing the particles requires a custom laboratory setup, as the

properties of commercially available forms of carbon black were unacceptable[48]. Furthermore, these particles were gradually oxidized by the CO_2 in which they were suspended to form CO, which lead to a loss of particle mass over time[47]. Thus, at present there does not appear to be a simultaneously cost effective and high performance pathway to reaching temperatures of 1,000°C and beyond.

To address these problems, we have proposed using a liquid metal heat transfer fluid (LMHTF) for a power tower receiver. A LMHTF offers three main benefits: (1) It is a condensed phase with a thermal conductivity more than an order of magnitude greater than non-electrically conductive HTFs (typically 10-100 W/m-K vs. ~ 0.1-1 W/m-K for non-electrically conductive fluids, such as molten salt[49]), which reduces the chances of developing hot spots that could cause failure due to thermal stresses. (2) Liquid metal viscosities are typically on the order of 1 mPa-s, similar to that of water. In combination with the high thermal conductivity of the LMHTF, these properties greatly reduce parasitic losses[50]. High thermal conductivity enhances heat transfer to the liquid to such an extent that conduction, rather than convection, is the dominant mode of heat transfer, eliminating the need to flow the fluid at a high velocity to create turbulence for higher heat transfer, as is typically required for non-electrically conductive fluids. This high thermal conductivity also makes molten metals a good candidate for use at the laboratory scale, as no other single phase HTF can achieve a convective coefficient similar to that of a liquid metal in the laminar regime. At the same time, losses due to flowing the fluid are further minimized, because of low the viscosity necessary when flowing the LMHTF. (3) Certain liquid metals have boiling points above 2,000°C, rendering them stable at the temperatures of interest. Additionally, the ability to pump liquids through sealed pipes

allows for more geometries than a falling particle receiver, as the movement of particles is constrained by gravity, and flowrates cannot be altered as easily and instantaneously as with a pumped fluid.

In spite of the advantages offered by LMHTF's, their potential use for CSP has been largely absent from the literature. What few papers do discuss LMHTF's often focus on sodium[51,52], which is limited to operating below its boiling point of 883°C. The lack of discussion of LMHTF's is primarily because they are more expensive than traditional HTF's[53] and have much lower specific heats, on a per unit mass basis, than many other HTF's[54]. Furthermore, they are in general extremely corrosive of metal containment materials[55-61] and have therefore been considered impractical. Because of the high cost of LMHTF's, their use can only be justified through higher efficiencies of the solar plant. Singer *et al.*[62] have demonstrated through simulations that using LMHTF's to reach operating temperatures of 700°C and running an ultra-supercritical (USC) steam Rankine cycle can potentially improve efficiency to ~55%. However, efforts to develop such an efficient USC cycle are still years away due to the requisite high temperatures and pressures, which in turn necessitate the use of expensive nickel alloys[33]. Alternatively, combined cycles operating at efficiencies approaching 60% have already been built and successfully demonstrated. Thus, the ability to attain temperatures >1,000°C could significantly and more immediately improve the efficiency of power cycles used in CSP plants.

Because of the operating temperatures at which such a plant would operate, radiation can quickly become the dominant source of heat loss, due to its scaling with the fourth power of temperature, according to the Stefan-Boltzmann law

$$q''_{rad} = \sigma\varepsilon(T_1^4 - T_2^4) \quad (1)$$

where T_1 is the temperature of the receiver, and T_2 is the ambient temperature of the environment. Thus any design intended to achieve temperatures in excess of 1,000°C must be careful to manage radiative losses, particularly when designing the solar receiver, which is directly exposed to the environment.

Solar Receivers

There are two primary classes of receivers: external receivers and cavity receivers. The difference between these two receivers can be seen in Figure 2. Broadly speaking, an external receiver is any receiver in which the optically absorbing surface of the receiver is exposed directly to the environment, with no insulation between to prevent heat from escaping the receiver. Often, this setup consists of several panels arranged cylindrically, where each panel is comprised of a bank of vertical tubes through which a HTF flows (see Figure 3). These panels are directly exposed to the environment, and are illuminated by light reflected off of heliostat mirrors. Cavity receivers, on the other hand, are designed to mimic a blackbody cavity. There is a small aperture through which light enters the cavity, and it heats a HTF as the HTF is flowed through/behind the cavity walls. Because the fluid is in a cavity, rather than being exposed directly to the environment, there is potential for decreasing the amount of heat lost to convection and reradiation.

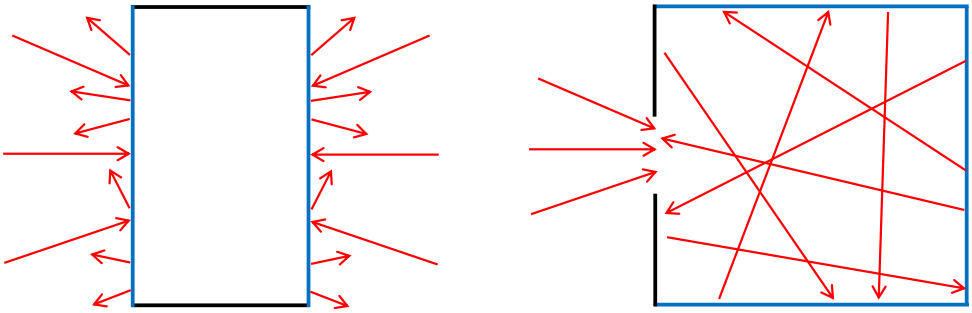

Figure 2. Illustration of the difference between an external (left) and cavity (right) receiver. Incident and reflected/reradiated light shown using red arrows. Blue lines are surfaces that would potentially be composed of tubes through which a HTF would flow, while black lines depict surfaces through which a HTF would not flow.

Figure 3. A solar panel being installed at the Crescent Dunes plant[63].

Some investigation into the performance of cavity receivers has been performed in the past; however much of the work has been focused on cavity receivers that use a gaseous (i.e. air or steam) HTF[39,40,42,44,45,64-67]. Other work has investigated cavities using salt as the HTF[68,69], but temperatures in this case are limited to well below 1,000°C. None of this work comprises a cavity receiver utilizing a liquid HTF at temperatures >1,000°C.

Amongst existing plants, only external receivers are used, because they greatly reduce spillage[15,70-72]. (Spillage occurs when light strikes an area adjacent to a target; in the case of a cavity receiver, this issue would occur if the spot size were larger than the aperture or if the spot was not aligned with the receiver aperture.) At the extreme temperatures at which LMHTF's are candidates for use however, external receivers would lose too much heat through reradiation to be practical (see Figure 4). Thus a cavity design is necessary to reduce losses due to reradiation.

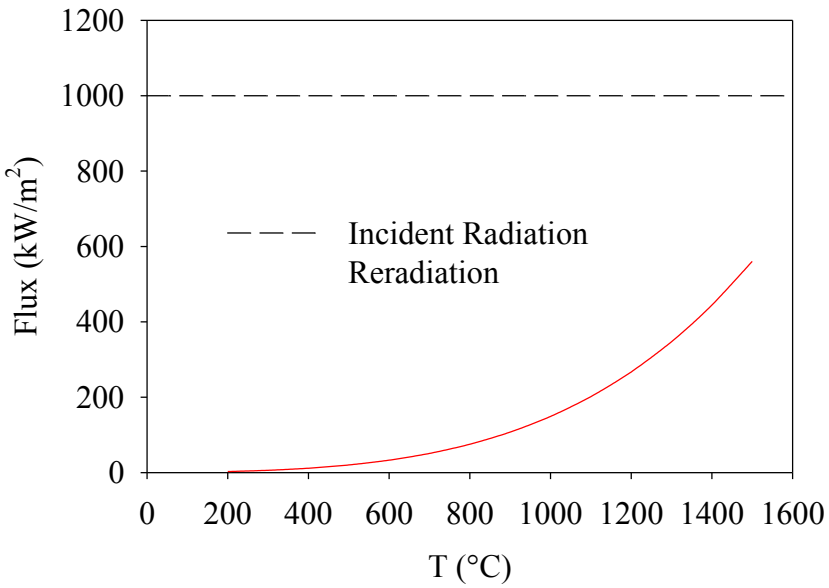

Figure 4. Comparison between the flux incident on a receiver vs. the reradiative flux coming off a receiver at different temperatures. Incident flux (typically ~1,000 kW/m^2) is fixed by the heliostat field, while reradiative flux is proportional to temperature to the fourth power.

Receiver Efficiency

Before addressing proposed solutions to the materials and efficiency issues, it is important to first define the efficiency of the receiver. Here, efficiency, η is defined as

$$\eta = \frac{\int_{T_{inlet}}^{T_{outlet}} \dot{m} C_p(T) dT}{\int \phi(r,\theta) dA} \quad (2)$$

where T_{inlet} is the inlet temperature of the HTF, T_{outlet} is the average outlet temperature of the HTF, $\dot{m}$ is the mass flow rate of the HTF, $C_p(T)$ is the specific heat of the HTF as a function of temperature, $\phi(r,\theta)$ is the spatially dependent radiant flux coming into the cavity through an aperture, given in kW/m^2, and A is the area of the aperture. Thus, the efficiency measures the amount of heat transferred to the working fluid (measured as an increase in its enthalpy) divided by the total incident solar energy.

The maximum theoretical efficiency for a receiver is given by Steinfeld as

$$\eta_{max} = 1 - \frac{\sigma T^4}{\phi} \tag{3}$$

where σ is the Stefan-Boltzmann constant, T is the blackbody temperature of the receiver, and ϕ is the average flux of light coming through the receiver aperture[73]. This value assumes conductive losses through the receiver walls and convective losses from the receiver are zero; thus IT is often seen as an upper limit. However, this simple expression also assumes the entire cavity is at a single temperature, which is often the case in thermochemical applications, but not in CSP. Instead, the flowing HTF is sensibly heated from a lower to higher temperature and does not exist at a constant temperature in the receiver. The fact that the temperature is lower in some locations within the receiver can potentially be exploited to reduce reradiation. This and other potential routes to achieving high efficiency at high temperature will be explored in subsequent chapters.

Outline of Remaining Chapters

Having identified issues with existing receiver technologies, and having defined a figure of merit by which to evaluate various receiver designs, we can begin to design a high performance, high temperature receiver. Our goal was to design and test a small

scale receiver that is capable of converting incident radiation to heat with an efficiency ≥80% and a HTF outlet temperature of ≥1,350°C. Testing using a small scale receiver allows the effectiveness of a receiver design to be determined before a full scale design attempted. The remaining chapters of this thesis will discuss the modeling used to design the receiver and will also discuss much of the ancillary work necessary to test a small scale receiver.

Chapter 2 considers design constraints for both small scale and large scale receivers. Chapters 3 and 4 discuss the methods we used to model small scale receivers, and the results of that modeling, respectively. Chapter 5 describes the setup of several components of the system used to test a small scale receiver, and it presents the results we have obtained so far from our experimental setup, including data used to validate the modeling discussed in Chapters 3 and 4. Chapter 6 lists several considerations to account for when designing a large scale receiver. Finally, some concluding remarks are presented in Chapter 7.

CHAPTER 2: RECEIVER DESIGN CONSIDERATIONS

There are two regimes in which we are interested in testing a solar receiver. The first regime is the 5-10 kW range, where the high flux solar simulator (HFSS) at Georgia Tech operates. The HFSS at Georgia Tech consists of an array of xenon arc lamps that focuses highly concentrated light onto a small region. A typical HFSS (such as that shown in Figure 5) consists of seven lamps, each contributing roughly 1 kW of light, concentrated to a spot size of approximately 6 cm, with a peak flux at the center >5,000 kW/m^2[74]. For comparison, the flux of sunlight on the surface of the earth is at maximum around 1 kW/m^2[75].

Figure 5. Picture of the HFSS at the University of Minnesota[76].

The second regime of interest for receiver operation is at a utility scale. Here, the receiver power input is on the order of 1-100 MW. Additionally, the sun provides an intermittent input to the receiver, unlike the constant power provided by a solar simulator,

and transient effects become more important; transient effects are further discussed in Chapter 6.

The design of such a receiver differs greatly depending on the scale involved due primarily to two considerations: cost and performance. To minimize costs, a large scale receiver should be made of pre-existing products (such as tubes), rather than custom machined geometries. However, for a small scale experimental receiver, a design consisting of hundreds, or even dozens, of tubes is impractical to manufacture. In our experience, using such a number of tubes requires an extensive number of bonds between parts, each of which becomes a potential point of failure within the receiver. At small scales, constructing the receiver from a few continuous pieces is simpler and requires fewer joints between parts, which in turn means a lower chance of a liquid metal leak forming. Because the design of the receiver in this case is less motivated by economics, a more complex custom design can be constructed with thicker walls, yielding a more robust final part that will survive during handling.

Small Scale Receiver Considerations

At the laboratory scale, constraints on the design of a receiver depend largely on what is easiest to implement and fabricate. Although there is some motivation to make components in a cheap and efficient manner, this concern is secondary to designing a proof of concept high temperature, high efficiency receiver. Several other factors can greatly affect receiver performance, and determining which factors matter and to what extent is critical to design a high efficiency receiver. In the following sections, we introduce factors we hypothesized may be critical to the performance of the receiver, then show how these factors influenced our decisions when designing a receiver.

Material Selection

The first factor to consider is what materials will be used in the system, which does not present an immediately obvious solution. For reasons detailed previously, we believe a liquid metal is the best option to use as a HTF. However, there are numerous liquid metals available for use as a HTF, each with various benefits and drawbacks. At a laboratory scale, the liquid metal we select should ideally be a single element. This requirement limits the number of possible chemical reactions that can occur, as compared to a substance such as a eutectic salt mixture, which is not only composed of several elements, but also different compounds. When using a single element, the configurational entropy of the system is more limited, because there exist fewer total chemical species available to form compounds, as compared to using a compound composed of several elements. This reduction in the total entropy of the system reduces, and potentially eliminates, any driving force for a reaction to occur. Apart from being a single element, the HTF should have a low melting point (as close to room temperature as possible if not below it) and a high boiling point to allow for a large range of operating temperatures. Because the liquid metal will be used in a laboratory environment, it is also preferable that it be non-toxic and that it not react violently with common materials such as air, water, other metals, etc.

For these reasons, we have selected tin as our HTF. Tin has a melting point of 232°C, which is low compared to most other metals, and it boils at 2602°C (at 1500°C, its vapor pressure is $<10^{-4}$ atm). Tin's unusually low melting temperature makes it much easier to work with compared to other potential liquid metal candidates, such as aluminum (melting point: 660°C). Furthermore, tin is not toxic, unlike lead or mercury,

and it does not react violently when in contact with water or oxygen at elevated temperatures, unlike alkali metals such as sodium.

There are three main disadvantages to using tin. One is its high density (~6900 kg/m^3) and the resultant large hydrostatic pressures that occur, particularly within a tower configuration. However, at laboratory scales, this issue is less problematic. Second is its low specific heat (~0.2 kJ/kg), which necessitates a comparatively larger amount of material required on a per-mass basis for thermal storage. Again, this is not an issue at laboratory scales, but at the utility scale, the increase in tank weight, in combination with tin's cost of \$7-9/kg[77] (compared to \$0.5-1 kg for nitrate salts[78]) makes tin uneconomical as a thermal storage fluid. Finally, tin corrodes nearly all other metals, including stainless steel, which is largely why it has not been pursued previously; thus selecting an appropriate containment material is critical.

Because steel and most other metals are incompatible with tin, the materials selection process for containment materials focused on alternatives to metals. Any material selected must be stable at all temperatures < 1,400°C and ideally should be completely inert with respect to tin. Furthermore a material with a high thermal conductivity is desirable to enhance the rate of heat transfer to tin in the receiver. High thermal conductivity also reduces temperature gradients within the material, which in turn reduces thermal stresses in the receiver. Furthermore, it is preferable if the material has high machinability, as it allows for easier fabrication of custom parts.

The material that we determined best fits these criteria is graphite, for a number of reasons. First, graphite does not form any known compounds with tin, and it does not sublimate until 3642°C. Between the high boiling point of tin and graphite's high

sublimation temperature, we are ensured that we are not limited by the materials we are using when attempting to reach elevated temperatures. Additionally, unlike many oxide refractories, graphite has a high thermal conductivity (100-150 W/m-K) and is easily machined.

The kinetics of both graphite and tin oxidation are sufficiently fast that they would cause the system to fail at elevated temperatures. Tin will oxidize significantly above its melting point[79-81], while graphite oxidation kinetics become significant above ~500°C[82]. Therefore, the entire experiment must be contained within an inert environment. While inert containment could be a significant issue when designing a full scale power plant, we believe that a structure could be built similar to a containment building used in nuclear power plants, shown in Figure 6.

Figure 6. Picture of a nuclear containment structure (concrete dome in the center of the image)[83].

Geometry Considerations

With the material of both the HTF and the receiver itself determined, the next design parameter to consider was the receiver geometry. Several questions arose when considering geometry, many of which did not have an obvious answer prior to building the full 3D model discussed later.

Chief among these questions is how to trap light in such a manner that the heat from the incident light is transmitted to the HTF, rather than simply being reflected or reradiated back to the environment. The distribution of light from the HFSS on the inner surfaces of the cavity receiver can significantly affect the temperature profile of the receiver, and this distribution is in turn affected by the geometry and reflectivity of various surfaces within the receiver. Thus, the shape of the receiver, as well as its optical properties, must be studied carefully to determine what aspects of the geometry have a significant effect on receiver performance.

Furthermore, fabrication (i.e. designing parts from which to make the receiver and determining how they fit together) is a critical issue to address before a final design is settled upon. We determined that, due to the small size of the receiver, it should be composed of as few pieces of graphite as possible, while still allowing for an assembly that could be performed with reliable joints. Using fewer graphite pieces means fewer bonded joints, which reduces the risk that molten tin will leak between the assembled components. (This concept is covered extensively in Appendix D.) An addendum to this constraint is that only geometries that can be fabricated are worth considering. For example, a geometry that incorporates a hollow sphere would require a process such as 3D printing, which is currently impractical for a refractory such as graphite. This

consideration effectively precludes the use of a single monolithic piece of graphite for the receiver.

Thermal Stresses

An additional factor to consider is the expected thermal stresses in the receiver. As compared to a utility scale receiver, a laboratory scale receiver is on the order of 30x30x30 cm, and the temperature increase is quite large (about 1,000°C). Because thermal stresses are a function of factors such as stress concentrators and the temperature distribution within the receiver, the geometry of the receiver has the potential to significantly alter the magnitude of these stresses. Furthermore, stresses scale with the magnitude of thermal gradients, i.e. the difference in temperature between two locations divided by the distance between them. For both large and small scale applications, the temperature difference is essentially the same, but the length scale over which the temperature difference occurs differs by more than an order of magnitude. Thus, thermal stresses in the small scale receiver are expected to be an order or magnitude larger than in the full utility scale implementation. However, without further study, it is not clear if any geometry would allow for thermal stresses below the material's fracture strength whereby it would immediately fail.

Thermal stresses are worth emphasizing, because of the relatively small scale and the large difference in temperature experienced by graphite. Additionally, graphite is a brittle material and has critical stress intensity factor, K_c, of only ~1 MPa-$\sqrt{\text{m}}$[84] and a tensile strength of around 50 MPa (though the tensile strength does increase between room temperature and 1,350°C by 20-40%, depending on the grade of graphite[85]). Therefore, thermal stresses must be carefully considered, and while graphite shows very

little susceptibility to fatigue under normal circumstances[86], it is ideal to remain well below the tensile strength of graphite to avoid thermal stress fracture. In our case, we elected to design our receiver with a minimum factor of safety of 3.

Cavity Convection

Taking into account the above considerations, we can design a receiver with appropriate materials and optimize it to minimize radiative losses and thermal stresses. However, even once a receiver geometry has been finalized to address all these constraints, the question of losses due to natural convection from the cavity remains. The extent of convection from the cavity is an important one to quantify, as losses due to convection through the aperture of the receiver will reduce the receiver efficiency. Not only do these losses negatively impact the performance of the receiver, but hot gases escaping the receiver could be potentially problematic if allowed to escape to parts of the system that should remain cool, such as the hermetic seals on the window immediately in front of the receiver. While some studies regarding natural convection within cavities do exist in the literature[87,88], they generally cover very particular situations, oftentimes involving a two-dimensional rectangular cavity[89,90]. Thus, they are not expected to provide accurate estimations of the convection through the aperture of our cavity receiver. To predict the convection from the cavity requires computational fluid dynamics (CFD) simulations to determine the velocity profile. This profile can then be used to solve for the heat leakage and to guide the development of a mitigation strategy for a worst-case scenario.

Large Scale Receiver Considerations

When constructing a full scale receiver, cost and performance become the dominant design constraints. The entire design process is ultimately determined by each sub-system's impact on the LCOE, as it is the metric used to determine the minimum price at which electricity can be sold; reducing the LCOE of a technology makes it more competitive with other technologies. Thus, while many considerations remain the same between small and large scale receivers, other factors come into play that significantly affect the design process of the receiver.

Materials Selection

At the utility scale, the criteria for selecting materials from which to construct the receiver differ somewhat as compared to materials requirements at a smaller scale. At the utility scale, it is necessary that receiver components are simple geometries that are easy to machine, or geometries that are already mass produced, which minimizes cost. The receiver material should also be resistant to thermal fatigue, as it will be cycled thousands of times over its ~30 year lifetime. Furthermore, the material should be resistant to thermal shock. This resistance is particularly important in the case that the receiver is operating at its maximum temperature and a cloud suddenly passes overhead. In this scenario, the receiver will cool quickly and in a non-uniform manner.

Many performance related requirements for material selection do remain similar to those at laboratory scale, such as high thermal conductivity and a high absorptivity in the visible and near-infrared region of the EM spectrum[91]. The material must also be compatible with the HTF selected. Once again, graphite fits all the criteria presented here.

For the same reasons listed in the preceding section, we have identified tin as a HTF candidate for a full scale industrial receiver. While tin is prohibitively expensive to use as a medium for thermal storage, the amount required to use in the receiver is minimal and would not have a substantial effect on the overall plant cost[50]. To incorporate TES, a cheaper, more energy dense aluminum-silicon alloy could be used for thermal storage. However, aluminum is not compatible with graphite, which is desirable to use for the receiver, since aluminum quickly corrodes graphite to form Al_4C_3[92,93], so tin remains a necessary component of the full scale design. Alternatively, however, the receiver could be constructed from a material such as silicon carbide, or graphite that has been coated so that it is compatible with an aluminum-silicon alloy. Doing so would simplify the overall plant design, but would not drastically reduce costs, as the need for a tin to aluminum-silicon heat exchanger has minimal impact on system cost and performance[50].

Geometry Considerations

As mentioned previously, the primary factor to consider when determining the geometry of the receiver is whether or not the design is possible to construct using predominantly prefabricated parts. In the event that a part is not readily available on the market, it should be simple and straightforward to produce to keep fabrication costs to a minimum. Furthermore, all parts, whether prefabricated or custom, should be appropriately sized, as unnecessarily large parts will quickly drive up costs. For instance, from our experiences contacting suppliers, a cluster of several small diameter tubes is generally cheaper than a single larger diameter tube.

As with small scale receivers, thermal stresses are an important factor to consider, as they not only affect material selection, but the geometry of the receiver as well. A utility scale receiver is much larger than a small scale prototype, so it is expected that thermal stresses will be approximately an order of magnitude lower. Nevertheless, because the receiver will undergo several thousand thermal cycles, it is best to keep any thermal stresses in the receiver to a minimum. Thus, a design that eliminates severe temperature gradients and complex geometric features that can act as stress concentrators is highly preferable.

As with the small scale receiver, the cavity should be designed to limit re-radiation. Because of the extreme temperatures (>1,350°C) at which the receiver will be operating, reradiation can cause efficiency to drop significantly. Thus, it is beneficial to minimize the view factor between the hottest portions of the receiver and the ambient environment.

Summary

Several parameters affect the design of receivers at both small and large scales. While material selection is limited due to the extreme temperatures involved in this application, we have nevertheless identified tin as a HTF and graphite as a containment material suitable to use in both small and large scale applications. Also common to both small and large scale receivers is the consideration that must be given to thermal stresses, particularly because graphite is brittle and has a critical stress intensity factor and tensile strength that are 1-2 orders of magnitude lower than metals. Fatigue life and resistance to thermal shock are factors that are particularly important at utility scale, as the receiver will be used continuously for several years, and the thermal input into the receiver (i.e.

the sun) is more variable than a solar simulator. Furthermore, natural convection from the cavity is of particular concern at the laboratory scale, because not only does convection lead to further losses, but hot gases escaping the cavity could potentially overheat other components of the experiment.

CHAPTER 3: MODELING METHODS

With the primary constraints laid out, we began to design the receiver, first through modeling, then through experimental testing. Our first step was to determine what factors most affect the performance of the receiver. Here, we present five cavity receiver designs and describe the effect altering parameters such as geometry and material properties have on the efficiency of the receiver. To quantify these effects, the receivers were simulated using a three-step method: (1) Monte Carlo ray tracing (MCRT) was used to model the incident light from the HFSS and determine the flux of incident light on the inner walls of the receiver for a given geometry; (2) thermal modeling combined the results of the MCRT with heat transfer simulations to determine the efficiency of the receiver; (3) the results of the thermal modeling were used to determine the thermal stresses within the receiver to evaluate the risk of failure. MCRT was performed using LightTools software, in collaboration with researchers at the Institute for Optics at the University of Rochester, while the thermal and structural modeling was performed using finite element modeling in COMSOL Multiphysics. The results from LightTools were then imported into COMSOL using an in-house code written in MATLAB, and the COMSOL heat transfer and stress analyses were subsequently used to evaluate the performance.

Receiver Models

This section details the progression of five LMHTF receiver designs we considered, starting with the “U-tube receiver”, then progressing to the “cone receiver”, the “inverted cone receiver”, the “cup receiver”, and finally the “cup-cone receiver”,

which we settled upon as our final receiver geometry. These designs attempt to satisfy three primary design criteria: (1) minimize the chance of receiver failure due to effects such as thermal shock, thermal fatigue, or undesired reactions between materials, (2) maximize the conversion efficiency from sunlight to thermal energy, and (3) maintain a liquid metal outflow temperature of at least 1,350°C. The target temperature 1,350°C was a nominal target based on milestones negotiated with ARPA-E. In reality there exists an optimal peak operating temperature that maximizes the performance and reliability of a CSP plant and minimizes cost. Several considerations that would determine the optimal peak temperature are the cost/performance tradeoffs associated with reaching higher optical concentrations and the performance/reliability tradeoffs associated with operating the heat engine at higher temperatures. There is no particular reason 1,350°C must be the target temperature; the receiver could conceivably operate at lower or higher outlet temperatures. However, this nominal temperature was initially chosen, because it allows for the use of SiC fabricated with residual solid silicon that would not melt until 1,414°C. Thus, for such a material the maximum operating temperature would be about 1,350°C, so as to avoid the melting of silicon. In the end, however, SiC was not used in the experiments, but the nominal target of 1,350°C was carried forward since there was little justification to change it.

The basic operating principles of the five receiver designs presented here are the same. Surfaces in the receiver are heated by incident radiant energy. Tin is heated by flowing across the opposite side of these surfaces (the side not heated directly by radiation). Knowing the temperature change between the inlets and outlets in combination with the mass flowrate allows the efficiency of the receiver to be calculated

using Equation (2). Cross-sections of each receiver geometry, as well as color map temperature profiles of these cross-sections, are presented in the following sections.

At one point, mullite was considered as an option to use alongside graphite, and many simulations were carried out with this option in mind. However, we ultimately elected not to use mullite in the receiver, as we found no benefit in its use.

For every receiver discussed here, light enters through the aperture at the top of the cavity. Another trait common to each of the five receivers is the two types of insulation that surround the receiver. The inner layer is a high temperature zirconia insulation capable of withstanding temperatures in excess of 1,500°C. The zirconia is surrounded by a low temperature microporous insulation that can only tolerate temperatures up to 1,000°C but has a thermal conductivity roughly one order of magnitude lower than that of zirconia (0.01-0.05 W/m-K[94] vs. 0.2-0.5 W/m-K[95]).

U-Tube Receiver

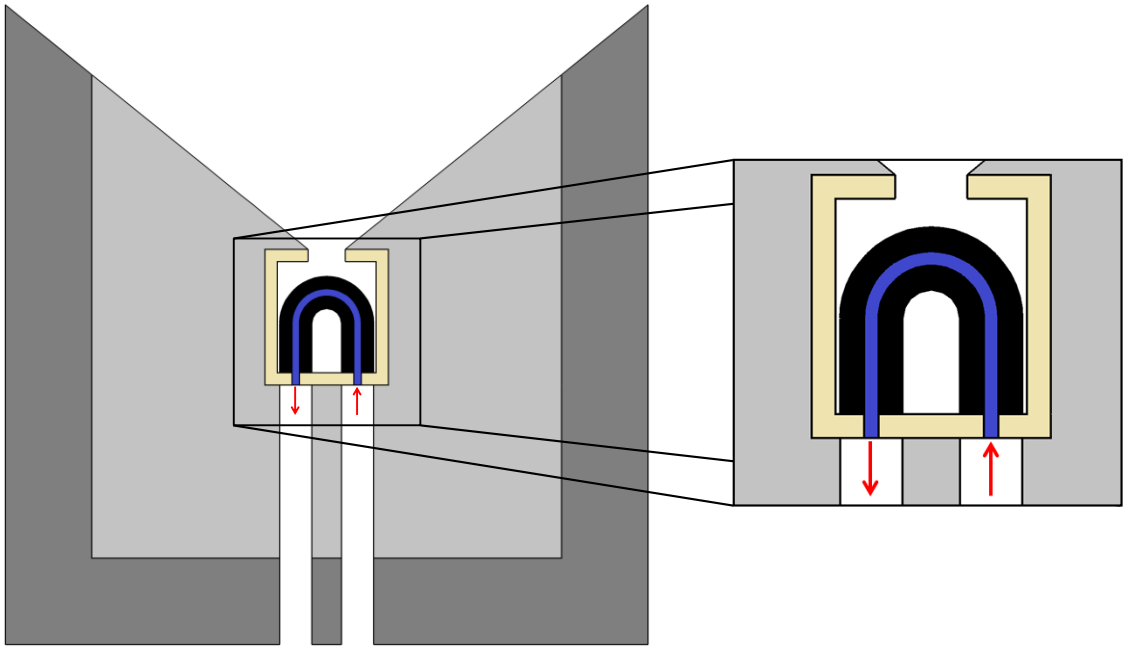

Figure 7. Cross section of the U-shaped tube receiver. Outer insulation is shown in dark gray, inner insulation in light gray, mullite in beige, graphite in black, and tin in blue. Direction of tin flow shown with red arrows.

The U-tube receiver consists of a cylindrical cavity with a U-shaped pipe within the cavity through which tin is flowed. This geometry was the first and simplest choice we considered, though it was not expected to be particularly efficient, since it does not provide sufficient surface area over which to heat the tin. However, the computational time required to simulate this receiver is low due to the simplicity of the fluid flow profile. For this reason, we used this receiver geometry as a base case to conduct parametric sweeps over different parameters (described in further detail in Chapter 4), before attempting to optimize the geometry itself.

Cone Receiver

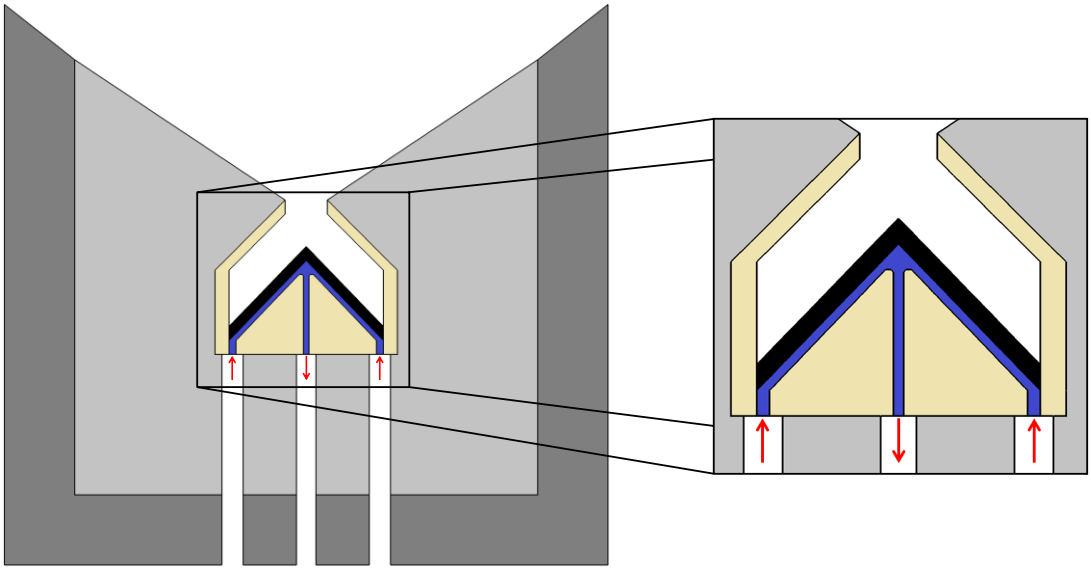

Figure 8. Cross section of the cone receiver. Outer insulation is shown in dark gray, inner insulation in light gray, mullite in beige, graphite in black, and tin in blue. Direction of tin flow shown with red arrows.

The cone receiver consists of two concentric cones with tin flowing between them; the outer cone is heated directly by radiation. In the original design, cold tin flows up through the center of the inner cone from the base to the apex, then down the face of the cone, until it reached the outer edge of the base of the cone, where it exits the receiver. The first design iteration was developed in an attempt to keep the tip of the outer cone cool by rapidly flowing the tin up through the center of the inner cone. The reasoning for cooling the tip was its close proximity to the receiver aperture. Because of its proximity, the view factor of the cone tip to the aperture, and therefore to the environment, is high. If the tip can be sufficiently cooled, it could potentially lead to a reduction in reradiative losses. However, we were unable to cool the tip sufficiently and instead created a temperature gradient of ~1,000°C/cm, which in turn leads to extreme thermal stresses. We eventually elected to reverse the path along which the tin flowed, which reduced the temperature gradient in the cone tip by an order of magnitude.

Inverted Cone Receiver

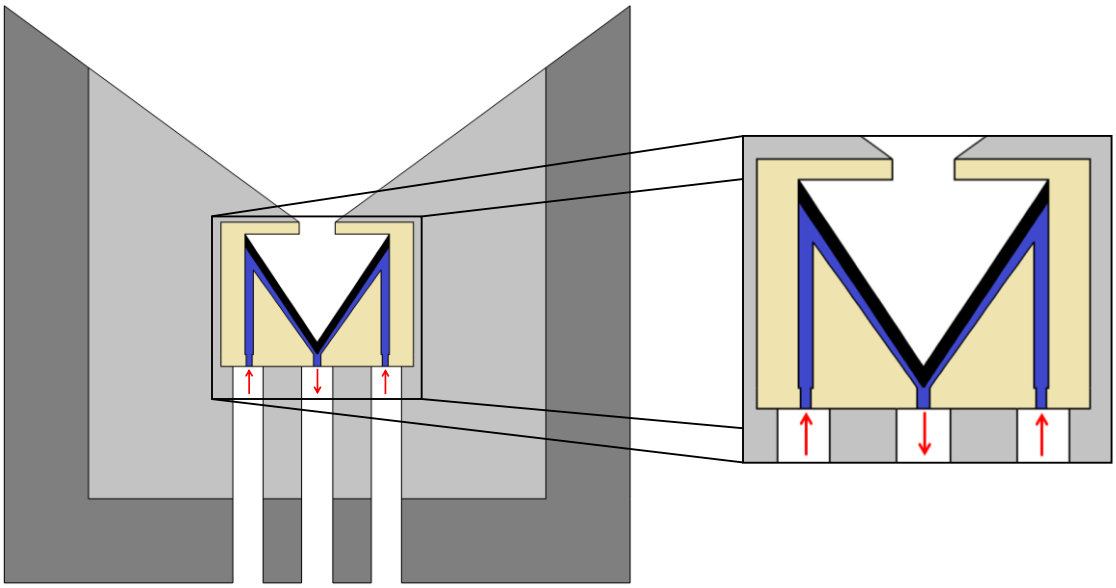

Figure 9. Cross section of the inverted cone receiver. Outer insulation is shown in dark gray, inner insulation in light gray, mullite (or another refractory) in beige, graphite in black, and tin in blue. Direction of tin flow shown with red arrows.

The inverted cone receiver was developed to address problems presented by the cone receiver. In particular, the inverted design was created to reduce the large thermal stresses developed in the cone receiver that persisted even after reversing the direction of flow.

The inside of the inverted cone receiver is a cone-shaped bowl. Similar to the original cone design, the bowl is nested within another bowl of the same shape, and tin is flowed between the two. Tin enters the receiver at its base near the outer cavity walls and flows up the sides of the receiver before flowing down between the "faces" of the inverted cones. The inner cone is heated directly by radiation, and heat is conducted through the inner cone to the tin.

Ultimately, we elected to abandon the inverted cone design, because it, along with the cone and U-tube receivers, developed stresses that are well in excess of graphite's tensile strength.

Cup Receiver

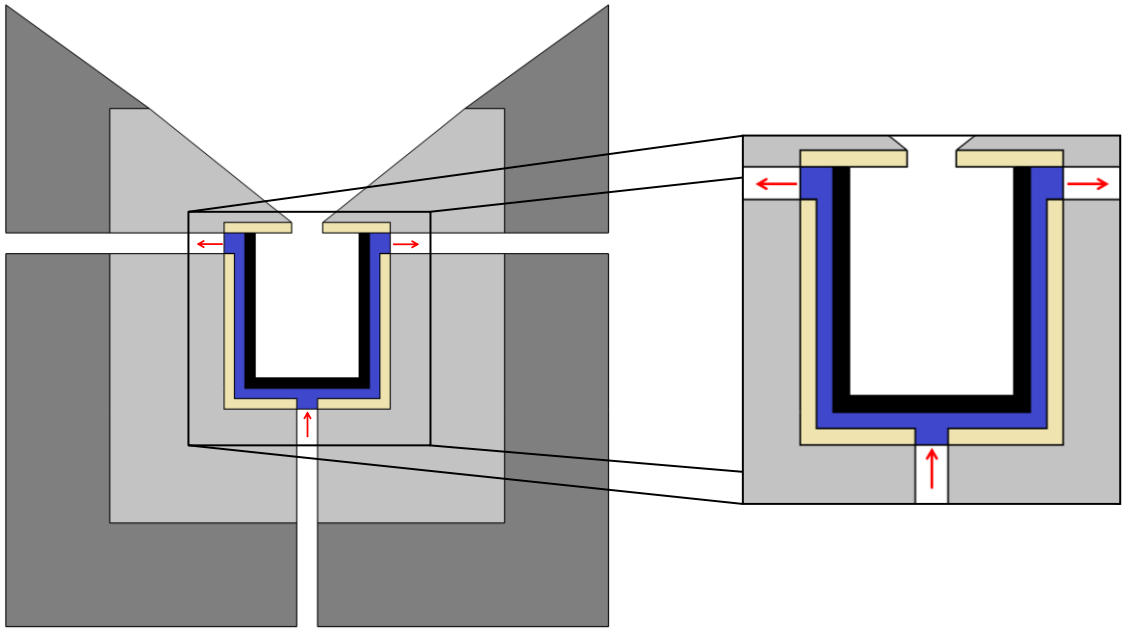

Figure 10. Cross section of the cup receiver. Outer insulation is shown in dark gray, inner insulation in light gray, mullite in beige, graphite in black, and tin in blue. Direction of tin flow shown with red arrows.

The cup receiver consists of two nested cups, with tin flowing between the two. Light enters an aperture through the "lid" of the cup and is absorbed by the inner cavity. Tin flows into the receiver at its base and up the side walls, exiting at the top of the walls, near the lid. This general design is the one we elected to construct, though we modified the design somewhat, which lead to the cup-cone geometry.

Cup-Cone Receiver

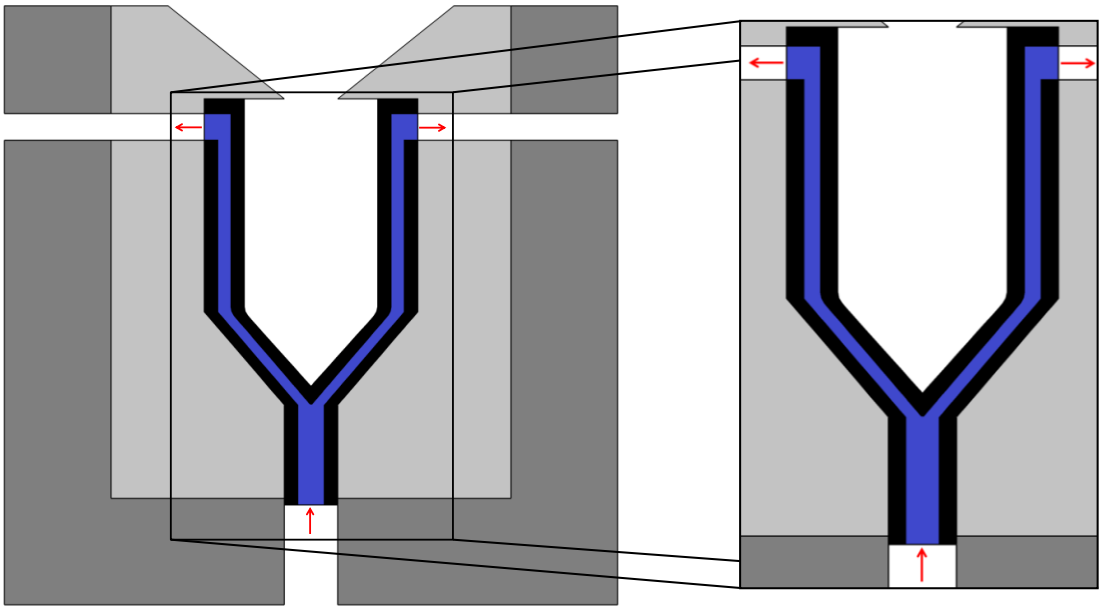

Figure 11. Cross section of the cup-cone receiver. Outer insulation is shown in dark gray, inner insulation in light gray, graphite in black, and tin in blue. Direction of tin flow shown with red arrows.

There are three primary differences between the cup and cup-cone designs. The first difference is that the entire receiver is made of graphite. This decision was made to keep the design as simple as possible, and because we realized there is no real benefit to using a ceramic other than graphite. Mullite has a thermal conductivity of approximately 5 W/m-K, which we believed may be useful to limit conduction of heat within the receiver. However, we found that the effect of using mullite was rather minimal. The second difference between the cup and cup-cone designs is a taper added to the inlet region of the receiver. This taper leads to a longer flow path, which in turn decreases the thermal stresses in the receiver, due to the lower temperature gradient. Without the tapered inlet, the thermal stresses developed are in excess of graphite's tensile strength, which would cause the graphite to fail. The third difference is the elimination of a "lid" to the receiver. It was found that near the aperture of this "lid", the thermal stresses are

considerable, as light that spills onto the aperture surfaces causes a local hot spot, and the heat cannot be easily dissipated. The cup-cone design eliminates this lid, instead using only insulation to keep light trapped in the receiver cavity. The cup-cone receiver is the design that was ultimately fabricated for testing, and we believe it is optimally designed for the experimental conditions to which the receiver will be subjected.

Monte Carlo Ray Tracing Methods

The first step necessary to accurately determine the receiver efficiency is to perform MCRT. Ray-tracing simulations were performed by the Moore Group under Dr. Duncan Moore at the University of Rochester in Rochester, NY. A CAD file of both the receiver and of the HFSS at the University of Minnesota was created in the CAD software SolidWorks and then imported into the MCRT program LightTools. The HFSS consists of six XBO® 6500W/HSLA OFR OSRAM lamps arranged in a hexagonal pattern around a seventh central lamp. As noted previously, these lamps deliver approximately 6.25 kW to a spot roughly 6 cm in diameter. The flux at the center of this spot is in excess of 5,000 kW/m^2, with an average flux of about 2,500 kW/m^2 over the full 6 cm diameter. Although the HFSS at the University of Minnesota is not being used for this project, it is very similar to the HFSS at Georgia Tech, and the geometry and performance of both is quite similar. Furthermore because a model for the HFSS (see Figure 12) at Minnesota had been published previously and was easily accessible, it was used for the MCRT modeling.

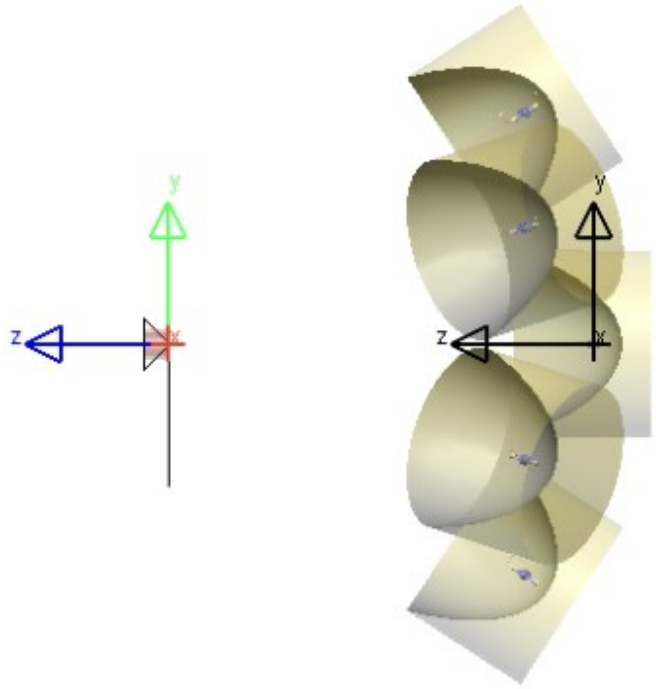

Figure 12. Typical LightTools MCRT model. The receiver is shown on the left as a red, semi-transparent cylinder (partially obscured by arrows), while the HFSS lamps are shown on the right.

Due to how LightTools is coded, the MCRT described here accounted for the absorptivity of the receiver surfaces by using probabilistic attenuation, rather than probabilistic absorption. That is, if a ray struck an opaque surface with a reflectivity of 0.4, the ray would reflect off the surface 100% of the time, but with only 40% of its incident energy. If probabilistic absorption were instead used, the ray would reflect off the surface 40% of the time, but with 100% of its incident energy. If a sufficient number of rays are traced, the result of either method is expected to be identical.

Once the MCRT was performed, the results were output from LightTools as a lookup table tabulating flux (in kW/m^2) at an array of coordinates. For any given simulation, the flux at approximately 10,000 unique coordinates would be generated. On average, a given point corresponds to a surface area approximately 3.4 mm^2. This output

was written to a Microsoft Excel file. After some manipulation of the data (described in the next section), it was written to several text files that could be read into COMSOL.

Data Conversion from LightTools to COMSOL

Due to the manner by which data was generated in LightTools, a custom MATLAB code was written to convert data from the format generated by LightTools to a format that could be read by COMSOL. A typical data file generated by LightTools is an m x n array of flux values. Because the receiver geometries are rotationally symmetric, the locations are given in cylindrical coordinates; the z-coordinate is described by the row number of the array, and the angular coordinate is described by the column number. In every case, the radius as a function of the z-coordinate is known. These values allow a 3-component Cartesian coordinate to be generated from the 2-component cylindrical coordinates. Once this coordinate is determined within the MATLAB code, the flux at the specified location is read from the Excel file, and then the Cartesian coordinates as well as the flux are written to a second file.

The data generated from MATLAB is then imported into COMSOL, and mapped onto a two-dimensional surface of the receiver that exists in three-dimensional space. The locations of element mesh nodes in COMSOL do not align perfectly with the coordinates generated using the MATLAB code. A 3-D linear interpolation is therefore used within COMSOL to determine the flux at coordinates not specified exactly by the MATLAB output. The interpolated flux is converted in COMSOL to a heat flux acting normal to the given surface.

In many cases, the input radiation was modeled as a hemispherical source located at the receiver aperture, rather than a heat flux mapped onto receiver surfaces. In such

cases, this simplification eliminated the need to preform MCRT, allowing for faster iteration using a single computer program. Comparing receivers modeled in this manner to those that used a flux map developed using MCRT models generally resulted in roughly a ±10% difference in receiver performance. We determined this level of error was acceptable in cases when we were only interested in the general trends in receiver performance due to altering a specific parameter. For example, we used this hemispherical source when sweeping across different values of insulation emissivity, as we expect our results to be quite insensitive to the exact temperature profile in the receiver. On the other hand, when determining the efficiency of a receiver, we use the MCRT, as an accurate temperature profile is necessary to obtain the most accurate results.

Thermal-Fluid Modeling

Apart from the heat flux present on the cavity surfaces due to incident light from the HFSS, several governing equations were used to calculate the flow of liquid tin and the heat transfer within the receiver, using finite element analysis. The fluid flow and heat transfer equations for the liquid tin are:

Mass continuity:

$$\frac{\partial u}{\partial x}+\frac{\partial v}{\partial y}+\frac{\partial w}{\partial z}=0 \tag{4}$$

Momentum conservation in the *x*-direction:

$$\rho\left(u\frac{\partial u}{\partial x}+v\frac{\partial u}{\partial y}+w\frac{\partial u}{\partial z}\right)=-\frac{\partial P}{\partial x}+\frac{\partial}{\partial x}\left(\mu\frac{\partial u}{\partial x}\right)+\frac{\partial}{\partial y}\left(\mu\frac{\partial u}{\partial y}\right)+\frac{\partial}{\partial z}\left(\mu\frac{\partial u}{\partial z}\right) \tag{5}$$

(Equations for the *y* and *z* directions are identical, with the exception that the first partial derivative on the right hand side of the equation is taken with respect to either *y* or *z*, and derivatives of *v* or *w* are taken, respectively, rather than the derivative of *u*.)

Conservation of energy:

$$\rho C_p \left(u \frac{\partial T}{\partial x} + v \frac{\partial T}{\partial y} + w \frac{\partial T}{\partial z} \right) = \frac{\partial}{\partial x}\left(k \frac{\partial T}{\partial x} \right) + \frac{\partial}{\partial y}\left(k \frac{\partial T}{\partial y} \right) + \frac{\partial}{\partial z}\left(k \frac{\partial T}{\partial z} \right) \quad (6)$$

The Brinkman number is defined as

$$Br = \frac{\mu U^2}{k(\Delta T)} \quad (7)$$

where U is the magnitude of the fluid velocity, k is the thermal conductivity of the fluid, and ΔT is the temperature difference between the wall and the bulk fluid. This value describes the ratio of heat generated due to viscous dissipation to heat conducted through the fluid. For the simulations detailed in this thesis, 5×10^{-7} is a typical value for the Brinkman number. This value is exceptionally low, due to the low viscosity and velocity of the tin and its high thermal conductivity. Because the Brinkman number is so low, viscous dissipation is negligible in the energy conservation equation.

At the walls, the no-slip condition was used:

$$u = v = w = 0 \quad (8)$$

In both the solid and liquid domains, the conduction governing equation used was

$$\frac{\partial}{\partial x}\left(k \frac{\partial T}{\partial x} \right) + \frac{\partial}{\partial y}\left(k \frac{\partial T}{\partial y} \right) + \frac{\partial}{\partial z}\left(k \frac{\partial T}{\partial z} \right) + q'' = 0 \quad (9)$$

where q'' is the heat flux generated through MCRT.

Radiative heat transfer was modeled according to the Stefan-Boltzmann law (Equation (3)). In both LightTools and COMSOL, all surfaces were modeled using the gray-diffuse approximation. Reradiation from the cavity was included in COMSOL simulations using the hemicube radiation method: each element was able to exchange radiation with other elements in the simulation domain, based on their respective view factors.

The convective coefficient off the surface of the insulation was calculated based on the relation provided by Incropera for a horizontal cylinder[96]. From this relation, the external surface of the insulation was prescribed a convective coefficient of 5.8 W/m^2-K. The emissivity of the insulation was prescribed a nominal value of 0.6, and the ambient temperature was set to 25°C. As will be shown later, the performance of the receivers is highly insensitive to either the convective coefficient or the emissivity.

Because the fluid in question is a liquid metal with a high thermal conductivity that is flowed at a low velocity, the tin temperature at the wall was set equal to the wall surface temperature. Using this boundary condition ensures no discontinuity in the temperature profile and is consistent with how the thermal boundary layer in a fluid is treated at low to moderate Reynolds values. Tin at the inlet was prescribed a uniform velocity profile, while the outlet condition set the pressure of the tin equal to ambient pressure and the shear stress equal to zero. We found that simulation results are identical if a quadratic velocity profile at the inlet is used instead; this result is unsurprising, because conduction and not convection is the dominant mode of heat transfer within the tin.

All COMSOL models included temperature dependent properties, including thermal conductivity, heat capacity, thermal expansion coefficient, viscosity, etc. Solving these governing equations using the finite element method generated a temperature profile, which in turn was used to calculate receiver efficiency and the thermal stresses in the receiver.

Structural Modeling

To calculate stress, thermal strain is first found from

$$\varepsilon_{th} = \alpha \Delta T \tag{10}$$

where α is the coefficient of thermal expansion, and ΔT is temperature of the material minus the reference temperature, which in this case is 25°C.

Total strain is defined as

$$\varepsilon = \frac{1}{2}\left(\frac{\partial u_m}{\partial x_n} + \frac{\partial u_n}{\partial x_m}\right) \tag{11}$$

where $\frac{\partial u_m}{\partial x_n}$ and $\frac{\partial u_n}{\partial x_m}$ are components of the displacement gradient.

The elastic strain, ε_{el} is simply the difference between the total strain and the thermal strain:

$$\varepsilon_{el} = \varepsilon - \varepsilon_{th} = C\sigma \tag{12}$$

where C is the compliance of the material and σ is the stress experienced by the material.

From here, it can be seen that stress in the material is given by

$$\sigma = E\left[\frac{1}{2}\left(\frac{\partial u_m}{\partial x_n} + \frac{\partial u_n}{\partial x_m}\right) - \alpha\left(T - T_{ref}\right)\right] \tag{13}$$

where E, the Young's modulus of the material, is the inverse of C.

Summary

A number of receiver geometries were designed, each with a particular purpose. The U-tube receiver design was created as a simple, easy-to-simulate geometry intended to be used in several studies in which the value of a single parameter was varied. The cone receiver and inverted cone receiver were designed with the intention of shifting the location of the hot spot in the receiver, in order to reduce losses due to reradiation from the cavity. The cup and cup-cone receivers were designed based on what we learned from the first three receivers, and were created to be high performance, low thermal stress receivers.

We also developed a method to run detailed, accurate simulations of our receivers. We first run a MCRT simulation to obtain the flux profile of light on the inner surfaces of the receiver. Converting that profile to a heat flux, we then run a conjugate heat transfer simulation to determine the fluid flow and temperature profiles within the receiver. The temperature profile allows us to calculate the efficiency of a receiver, as well as the thermal stresses that develop within the receiver.

CHAPTER 4: MODELING RESULTS

The modeling described in Chapter 3 comprised two primary analyses. The first was a sensitivity analysis, which determined the factors that were most critical to achieving high receiver efficiency. This analysis was performed using only the U-tube receiver, because the simplicity of the geometry leads to the flow of the tin through the receiver converging roughly ten times faster than through the other geometries. Once these critical factors had been determined, the knowledge gained from the sensitivity analysis was used to perform an analysis of the receiver geometry, which allowed us to design a receiver that was not only thermally efficient, but could withstand the thermal stresses developed within the receiver.

Mesh Convergence

Mesh convergence was the first test performed. Using the U-tube model, the coarseness of the mesh within COMSOL was set to "fine" (67,764 elements), "finer" (288,474 elements), and "extra fine" (736,263 elements). Values obtained for the finer and extra fine meshes were within 1%; thus a finer mesh was used for subsequent simulations.

Table 1. Values of parameters examined for different mesh densities. Percent difference between parameters evaluated for finer and extra fine meshes included.

	Fine	Finer	Extra Fine	% Difference
Average Fluid Velocity (m/s)	0.0916	0.0885	0.0885	0.500
Outlet Temperature (°C)	1768.7	1806.1	1815.5	0.452
Average Cavity Temperature (°C)	1826.2	1861.2	1871.0	0.455

Sensitivity Analysis

A number of parameters were examined for the U-tube sensitivity analysis. To determine what factors could affect the receiver performance, our first step was creating a basic thermal resistance network to understand how heat flows in the system. Figures 13 and 14 depict the different paths heat can follow within the receiver assembly and possible thermal loss mechanisms.

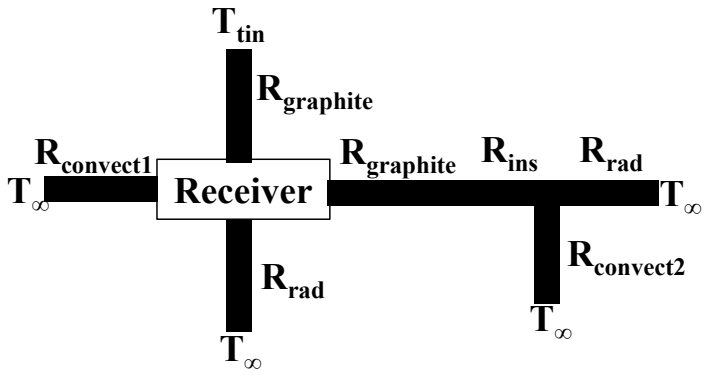

Figure 13. Thermal resistor network for the receiver. The subscript 1 denotes losses from the cavity through the receiver aperture, while a subscript of 2 denotes losses off the surface of the insulation.

From this network, it can be seen that several parameters could potentially dictate how heat is transferred within the receiver. These parameters include the conductivity of various materials, those materials' emissivities, the geometry of the cavity (both dimensions and general shape), which affects how heat is lost through the aperture due to radiation and convection, and the effective convective coefficient off both the surface of the insulation and the surfaces within the cavity. Additionally, by examining Equation (2), it can be seen that both the mass flowrate and the outlet temperature of the receiver can affect the efficiency as well. However, due to conservation of energy, it is evident that the flowrate and outlet temperature are directly coupled, and altering one therefore inevitably alters the other.

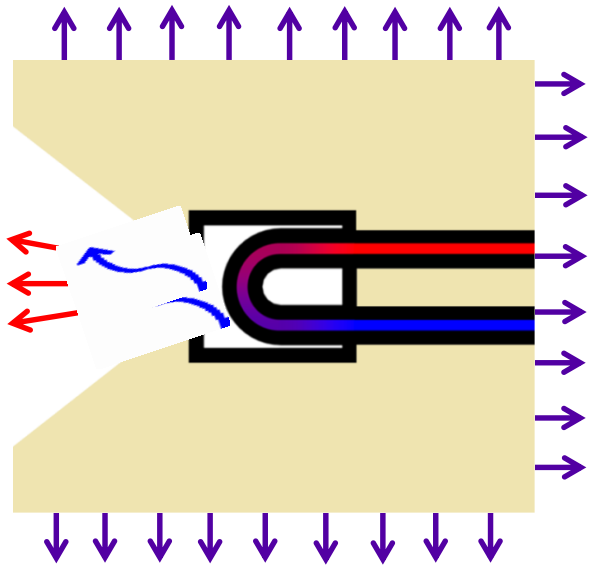

Figure 14. Illustration of potential loss mechanisms in a receiver: cavity reradiation (shown with red arrows), convection from the cavity (shown with blue arrows), and convective and radiative losses off the surface of the insulation (shown with purple arrows).

Tin Flowrate

The tin flowrate through the receiver has a straightforward effect on receiver efficiency. When tin flows faster through the receiver, it keeps the receiver at a lower temperature, thereby reducing the average temperature of the receiver and the associated thermal losses. In this way, more heat is transferred to the tin, and efficiency of the receiver increases. This increase in efficiency can be seen in Figure 15. However, this increase in flowrate (and thus, decrease in the outlet temperature of the tin), negatively impacts the thermodynamic efficiency of any power cycle that uses heat from the tin as its thermal input. Thus, for a given system, the outlet temperature of the receiver should be adjusted to maximize the overall system efficiency, rather than the efficiency of a single component (i.e. the receiver or the power block).

Because the receiver designed for this project is not providing heat to a power cycle, we set a target outlet temperature at 1,350°C. Thus, within the confines of the

target values we have established, receiver efficiency is maximized when the flowrate is such that the outlet temperature is at exactly 1,350°C. A higher outlet temperature would reduce the overall efficiency due to a higher rate of heat loss from the receiver.

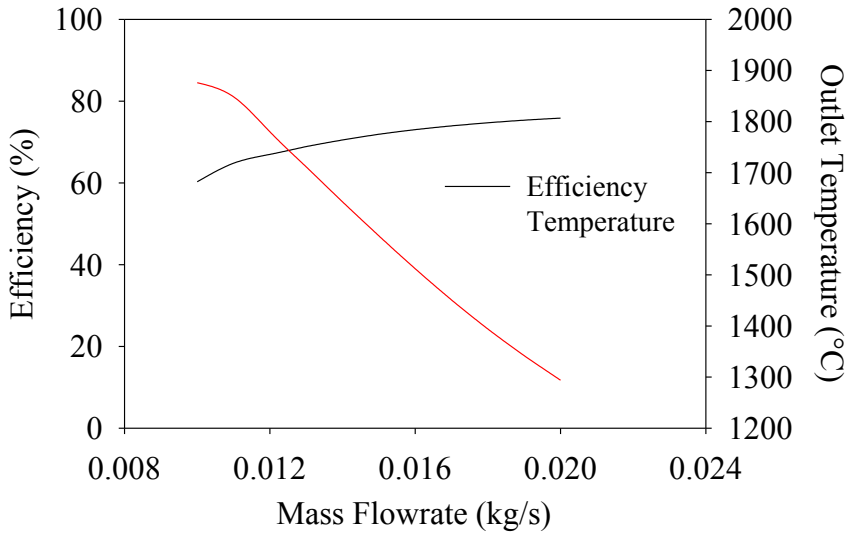

Figure 15. Receiver efficiency and outlet temperature vs. tin flowrate.

Dimensions

Three dimensions were altered for the sensitivity analysis –cavity height, cavity width, and insulation thickness. In every case, when one dimension was altered, every other dimension was held constant. For instance, when the receiver cavity height was increased, the tube portion of the U-tube receiver remained the same size. Thus, in this case, altering the cavity height effectively moved the tube towards or away from the top of the cavity.

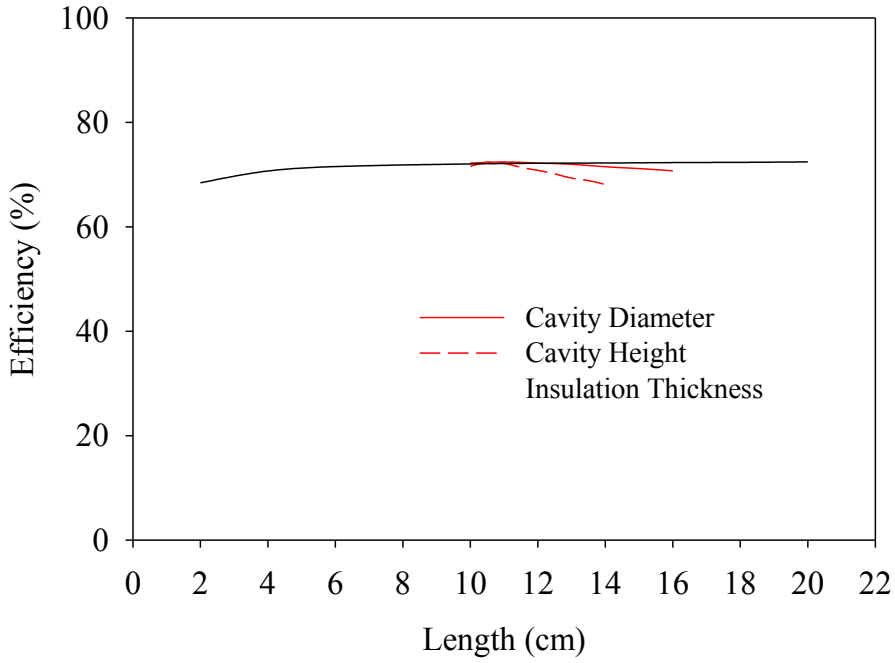

Figure 16. Receiver efficiency vs. cavity width, cavity height, and insulation thickness.

It can be seen in Figure 16 that significantly altering the width or height of the receiver did have some effect on receiver efficiency, but the effect is not pronounced. The drop in efficiency with increasing receiver dimensions is due primarily to the fact that increasing the dimensions of the cavity increases the surface area through which heat can escape to the environment. Furthermore, because increasing the height of the walls moves the tube portion of the receiver further from the aperture the amount of light striking the tube decreases. Instead, the light strikes the walls of the receiver, heating them up and causing them to reradiate more heat back to the environment.

A more surprising result of this parametric sweep is the fact that the performance of the receiver is only weakly dependent on the thickness of the insulation. It would be reasonable to expect that a large amount of insulation is needed to prevent the receiver from losing much of its heat through the walls of the cavity. But beyond a few

centimeters of insulation, there is little benefit to using more insulation. The reason for this is two-fold. First, even when very little insulation is used, its thermal resistance is such that heat lost to reradiation from the cavity is still the dominant loss mechanism; even given an insulation thickness of only of 2 cm, for a 7 kW radiant input, losses from the surface of the insulation were 483 W while losses due to reradiation were 973 W. Second, the effective resistance of the insulation asymptotically approaches a finite value as its thickness approaches infinity. This behavior can be observed by approximating the receiver as a sphere, surrounded by a hollow sphere of insulation. In this case, the thermal resistance, *R*, of the insulation is

$$R = \frac{\frac{1}{r_1} - \frac{1}{r_2}}{4\pi k} \tag{14}$$

where r_1 is the inner radius of the sphere, r_2 is the outer radius, and k is the sphere's thermal conductivity. Because the size of the receiver is fixed, r_1 remains constant, and only r_2 changes in Equation (14). As the insulation thickness approaches infinity, the thermal resistance approaches $(4\pi r_1 k)^{-1}$ and no longer depends on r_2. This asymptotic behavior is supported by results from the parametric sweep; past a thickness of 8 cm, the losses through the insulation vary by less than 3 W (0.043% of the input power).

We elected to use insulation with a thickness of approximately 20 cm. Such a thickness is sufficient to provide the maximum insulation possible for the receiver, and additional insulation leads to space constraints in the experiment. Furthermore, at 20 cm thick, the insulation has a surface temperature of ~50°C on average. Lower thicknesses of insulation lead to unacceptably high surface temperatures (e.g. 130°C average temperature for a 6 cm thickness), which could quickly cause problems in the experiment

– heat from the surface of the insulation could convect or radiate to other components within the experiment that should remain at ambient temperatures. While the total heat loss through the receiver insulation is effectively the same regardless of the thickness, ensuring components near the receiver can be heated at maximum to a few degrees above ambient can be critical, particularly in the case of components such as the seal around the window or the motor used to run the liquid metal pump.

Thermal Conductivity

Prior to our performing a sensitivity analysis, it was not clear whether the thermal conductivities of materials available were sufficiently high to enable a high (i.e. >80%) efficiency receiver. In the case of the receiver itself, a material with a low thermal conductivity would not transfer heat efficiently from the irradiated surface to the HTF. Instead, the heat would simply be reradiated or convected from the irradiated surface. On the other hand, if the thermal conductivity of the insulation is too high, heat lost through it would not be sufficiently reduced.

To alter the conductivity of materials within our simulations, the temperature dependent thermal conductivity was multiplied by a scaling factor. In this way, we preserved the temperature dependence of the conductivity while changing its magnitude. Values presented in Figure 17 are conductivities at room temperature. For reference, the effective composite thermal conductivity of the zirconia and microporous insulations is approximately 0.05 W/m-K[94,95], while the conductivity of the graphite we are using is 102 W/m-K[97] at room temperature.

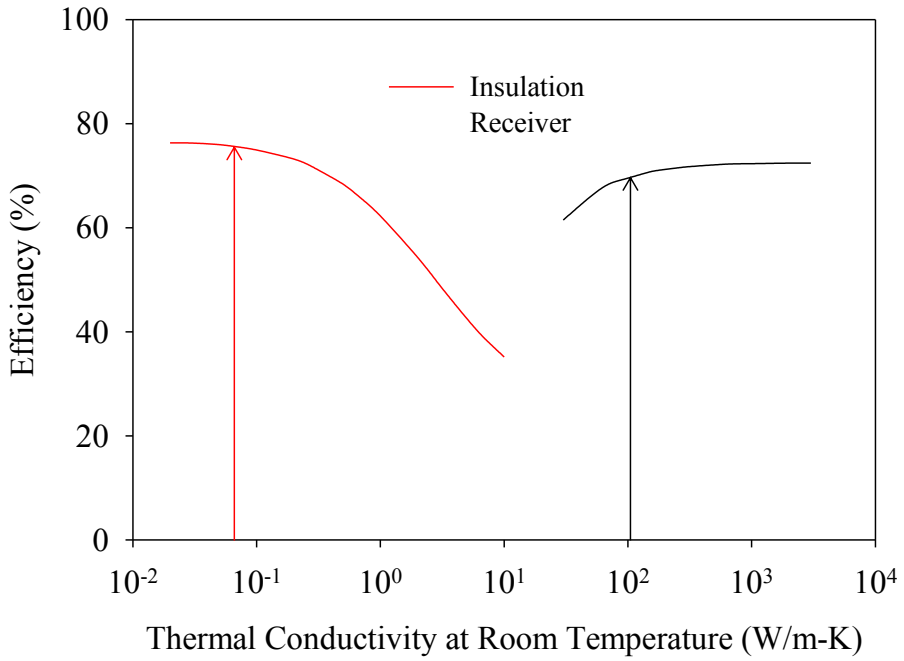

Figure 17. Receiver efficiency vs. insulation conductivity and graphite conductivity. Actual values for each material being used shown using arrows.

From Equation (14), it can be seen that while increasing insulation thickness has diminishing returns, the conductivity of the insulation can drastically affect how much heat is lost from the receiver. This finding is supported by the data in Figure 17. As the thermal conductivity increases above ~0.1 W/m-K, receiver efficiency drops considerably. In the case that the conductivity significantly exceeds this value, heat losses through the insulation become the primary loss mechanism in the receiver.

Conversely, the efficiency of the receiver drops off appreciably when the thermal conductivity of the graphite decreases below ~100 W/m-K. In this case, the thermal resistance between the irradiated surface of the receiver and the surface in contact with tin becomes comparable to the thermal resistance. The radiative heat transfer coefficient is

$$h_{rad} = \varepsilon\sigma(T_{hot}^2 + T_{amb}^2)(T_{hot} + T_{amb}) \quad (15)$$

Assuming an emissivity of 0.8 for graphite, a hot temperature of 1,350°C, and an ambient temperature of 25°C, the resultant effective value of h_{rad} is 237 W/m^2-K. For conduction, the effective heat transfer coefficient can be calculated as

$$h_{cond} = \frac{k}{L} \quad (16)$$

For all the receiver geometries we designed, the thickness of the graphite, L, is 1 cm. At 1,350°C, the conductivity of graphite is approximately 50 W/m-K[98], so the value of h_{cond} is therefore ~5000 W/m^2-K. In this case, the thermal resistance due to conduction is 4.7% of that due to radiation, leading to the vast majority of heat flowing into the tin, rather than back out the cavity. However, if the thermal conductivity of graphite were an order of magnitude lower, the thermal resistance due to conduction would be 47% of the radiative resistance. This fact is worth noting because many refractory materials have conductivities closer to 5 W/m-K than 50 W/m-K, especially at such extreme temperatures. The difference in conductivity between different materials underscores graphite's importance in this design. Very few refractory materials have a sufficiently high thermal conductivity to make an efficient receiver material while also being chemically compatible with molten tin.

Emissivity

The effects due to the emissivity of the surfaces within the cavity were somewhat unexpected. Emissivity values were altered for both the tube itself and the cavity walls, as depicted in Figure 18. One of four values was prescribed for each surface independently: 0, 0.45, 0.8, or 1, for a total of 16 different possible combinations of emissivity. The

values selected are based on the extreme cases for emissivity (0 or 1), as well as approximate emissivity values for both graphite (0.8) and mullite (0.45).

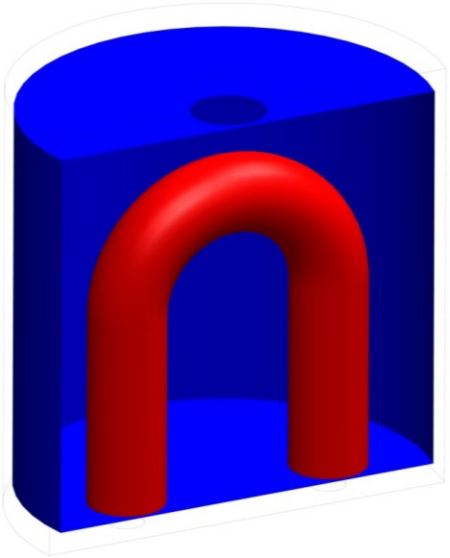

Figure 18. Illustration of the two different groups of surfaces whose emissivities were altered. The "tube" surfaces are shown in red, while the "cavity walls" surfaces are shown in blue.

In these simulations, the emissivity value listed was used for both the MCRT in LightTools as wells as the reradiation in COMSOL. Because a gray approximation was used in the simulations detailed here, absorptivity and emissivity are identical. Thus in this particular case, the decision to use the term "emissivity" rather than "absorptivity" is entirely arbitrary.

Table 2. Receiver efficiency vs. emissivity of the tube and cavity walls. Cell color is based on efficiency, with higher values in green and lower values in red.

ε_{tube} \ ε_{walls}	1	0.8	0.45	0
1	66.8	67.0	67.6	69.2
0.8	67.5	67.1	67.5	69.4
0.45	66.5	66.5	66.6	67.9
0	65.4	65.1	64.4	-0.2

Table 2 gives the efficiency of the U-tube receiver for each of the 16 different emissivity scenarios. It can be seen that the efficiency of the receiver is negative in the case that the emissivities of both the cavity and the tube are zero. The reason for this is straightforward: when both emissivities are set to exactly zero, no light is absorbed by any surface in the receiver, which means the receiver is never heated. In this case, the tin, which flows into the receiver at a temperature above ambient, cools off slightly as it flows through the receiver.

Examining cases where the emissivity of the tube itself is equal to zero, the efficiency of the receiver drops by only a few percent. Though this result is initially surprising, upon inspection, the reason for this behavior becomes apparent. Light entering the receiver will for the most part be absorbed by the walls. A small fraction is lost immediately due to reflecting off the tube, but the amount is only about 1% of the incident light. Once light is absorbed by the cavity walls, the walls to heat up and the heat is in turn conducted to the tube within the receiver. The thermal resistance of the insulation is such that the heat lost through the insulation is within a factor of 2 of the heat lost when the tube is prescribed a non-zero emissivity. Furthermore, because the tube, which has a large view factor to the aperture (and thus, the environment), has an emissivity of zero, it does not radiate heat, thereby reducing losses due to reradiation. However, because there must be a temperature gradient to drive heat from the cavity walls to the tube, the average temperature within the cavity is higher than if the tube had a non-zero emissivity. This higher temperature causes heat to be lost from the receiver more rapidly. The overall effect of these competing trends is that the receiver efficiency is reduced but only slightly.

On the other hand, reducing the emissivity of the walls to zero improves the receiver performance slightly. When the emissivity of the walls is zero, heat cannot be transferred as effectively from the tube, which is being heated directly by light, to the cavity walls, as conduction is the only means by which the heat is transferred. Thus, the cavity walls are at a slightly lower temperature than they would be otherwise, which reduces the amount of heat lost through insulation to the environment.

When the emissivities of all surfaces are non-zero, the receiver efficiency is affected by only about 1%. In this case, all surfaces can absorb thermal radiation, to the extent that the temperature profile in every case is virtually identical.

The optical absorption of an ideal blackbody cavity is independent of emissivity. Because the receiver is a cavity intended to mimic a blackbody cavity, the chance that a ray of light that has entered the cavity will be reflected back out is small; the surface area of the aperture is small compared to the surface area of the cavity itself, so light is much more likely to be absorbed by the receiver than to travel back out the aperture. A rough approximation for the effective emissivity of a cavity can be obtained using

$$\varepsilon_{effective} = 1 - (1 - \varepsilon)^{\left(\frac{A_{aperture} + A_{cavity}}{A_{aperture}}\right)} \tag{17}$$

where A_{cavity} is the surface area of the cavity, and $A_{aperture}$ is the area of the aperture. The derivation of this equation can be found in Appendix B. The ratio of $A_{aperture} + A_{cavity}$ to $A_{aperture}$ is around 28 for the U-tube receiver, so even for a real emissivity of only 0.1, the effective cavity emissivity is estimated as 0.948, according to Equation (17). For a real emissivity of 0.2, the effective emissivity is approximately 0.998. Thus it is reasonable to assume that the ability of a cavity to absorb light is only very slightly dependent upon the actual emissivity of the material from which it is constructed. MCRT

results support this conclusion, as for any geometry, the amount of light reflected back to the environment, regardless of emissivity, was found to be < 5% of the light entering the cavity. The one exception is the obvious case where all surfaces in the U-tube receiver were prescribed an emissivity of zero.

Additional studies were performed on the cone, inverted cone, and cup receivers, in which surfaces in contact with tin and those not in contact with tin had their emissivities varied independently. The efficiency of each receiver in each particular case can be found tabulated in Appendix C. We found that the performance of the receiver in each case was only weakly dependent on emissivity of either set of surfaces.

The effect of the insulation emissivity at the surface of the insulation was also considered, but, as can be seen in Figure 19, it was found that efficiency is highly insensitive to insulation emissivity. Even for an emissivity of zero (and therefore an effectively infinite thermal resistance), heat is removed from the surface of the insulation by natural convection. On the other hand, if the emissivity is set to one, this resistance is still in series with heat conduction through the insulation. From Equation (14), the thermal resistance of the insulation is approximately 2 K/W. For comparison, the thermal resistance of natural convection or radiation near ambient temperatures is about 0.2 K/W. The effect of altering the emissivity, and in turn the radiative resistance, is therefore negligible, because even if radiation off the surface of the insulation is eliminated, the thermal resistance at the surface of the insulation is an order of magnitude lower than the thermal resistance of heat conducted through the insulation. Thus, conduction through the insulation – and not radiation or convection from the surface of the insulation – is the

dominant thermal resistance. A similar effect can be observed when the convective coefficient off the surface of the insulation is altered.

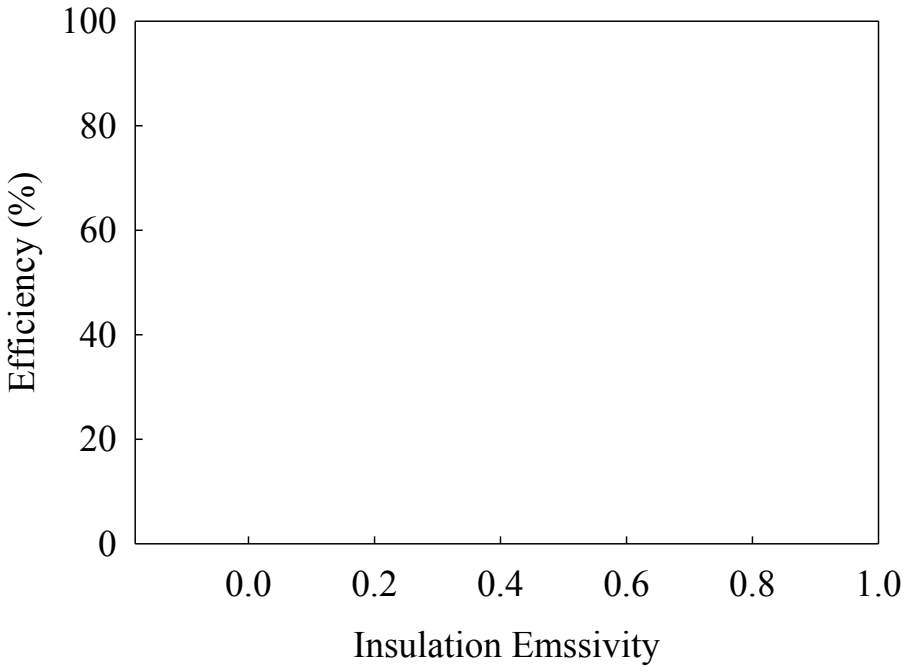

Figure 19. Receiver efficiency vs. emissivity of the insulation.

Convection

Although radiation is the primary concern in this sensitivity analysis due to the manner by which it scales with temperature, convection is still an important effect to consider. The effects of convection both off the surface of the insulation and from the cavity itself lead to additional heat leakage from the receiver.

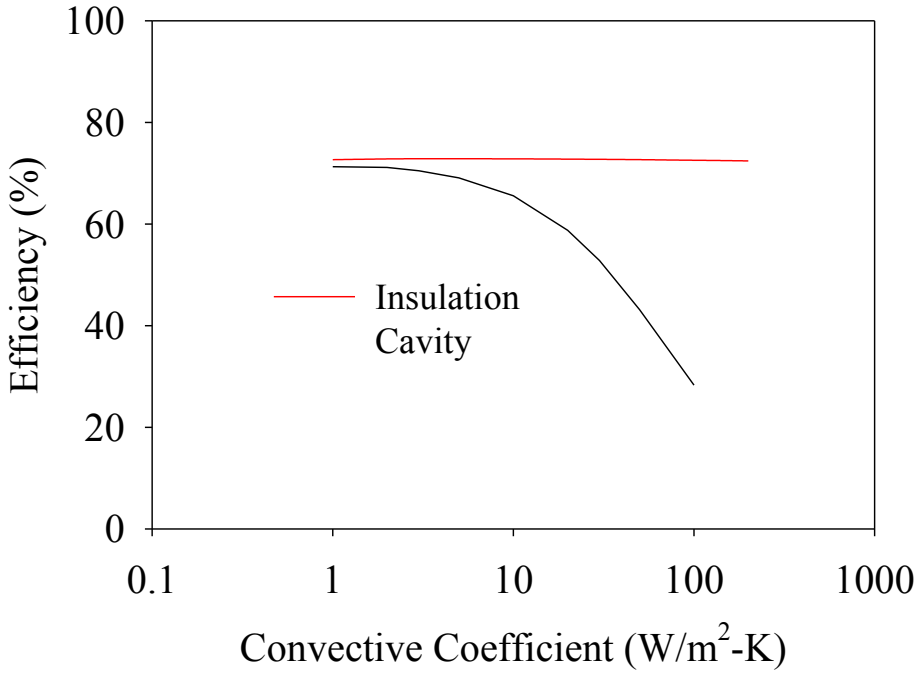

Figure 20. Receiver efficiency vs. convective coefficient of the cavity surface and the insulation surface.

The effect of altering the convective coefficient off the surface of the insulation is minimal, for the same reasons changing the emissivity of the insulation had virtually no effect – namely because the convection off the surface of the insulation is not a limiting thermal resistance, since it is in series with conduction through the insulation. No matter how high the convective coefficient off the insulation surface is, there exists a limit to how much heat will escape through the insulation. In the limit that the convective coefficient approaches zero, radiation off the surface of the insulation still exists, but is an order of magnitude lower thermal resistance than is conduction through the insulation. Thus, the temperature at the surface of the insulation remains more or less constant, and the heat lost through the insulation is essentially unchanged.

The convective coefficient off the surface of the insulation is expected to be approximately 5 W/m^2-K, which is a typical value for natural convection. However, even

if gas were being blown over the insulation leading to forced convection, the change in the performance of the receiver can be seen to be negligible.

Though understanding the effect of convection off the surface of the insulation is straightforward, the effects of convection within the cavity are some of the most difficult to accurately assess. For this sensitivity analysis, we swept across values of an effective heat transfer coefficient, h, to determine the point at which its value would have a significant effect on the receiver performance. It is clear from Figure 20 that even for convective coefficients typical of natural convection (5-10 W/m^2-K), convection from the cavity can lead to a significant drop in the efficiency of the receiver. At higher coefficients, convection causes the efficiency to decrease drastically. However, because gas will not be externally forced in or out of the cavity, this discussion will be limited to h values <10 W/m^2-K, a value which is on the higher side of natural convective coefficients for a gas; it is worth noting however that to avoid effecting a larger convective coefficient, flowing gases near the receiver aperture should be done with care.

The behavior of gases within the cavity differs from typical cases discussed in the literature. Firstly, the temperature difference between the hottest gases in the cavity and ambient gas outside the cavity is in excess of 1300°C. To even obtain a value for the effective Grashoff number within the cavity is difficult to do with any degree of certainty, as the Grashoff number depends on the gas coefficient of thermal expansion and the kinematic viscosity, both of which exhibit large temperature dependences. For example, nitrogen's thermal expansion decreases by 81%, and its viscosity increases by 300% between room temperature and 1,350°C. Therefore the local Grashoff number will vary drastically between locations, and using a single value for the Grashoff number is

essentially guaranteed to introduce a significant degree of error in any values being calculated. Secondly, the geometry in question is a horizontal cylinder with a small hole in one end, and the heating load on the cavity walls is neither constant temperature nor constant heat flux. Due to these irregularities, the case presented here differs significantly from cases in which simple approximations can be applied to determine an effective convective coefficient.

Due to the uniqueness of the problem, accurately determining the heat transported by gas flowing out the receiver aperture in such a situation necessitates the use of CFD. Because of the difficulty in converging CFD simulations in COMSOL, cavity convection was not simulated until the receiver design had been finalized. Once the cup-cone geometry was identified as the receiver we plan to test experimentally, the flow of gas occupying both the volume within cavity and the space immediately outside the cavity was simulated using COMSOL. Boundary conditions were prescribed by setting the temperature at each surface equal to the temperature generated by previous thermal modeling of the receiver. This temperature profile was obtained when simulating effects such as tin flowing through the receiver, radiation, conduction through the insulation, etc., but neglecting cavity convection. At the boundary open to the environment (see Figure 21), the gauge pressure of the gas was set equal to zero, and the temperature to 25°C. A downward volume force equal to the local density times the gravitational constant was applied to the gas occupying the cavity as well, to induce buoyancy driven flow.

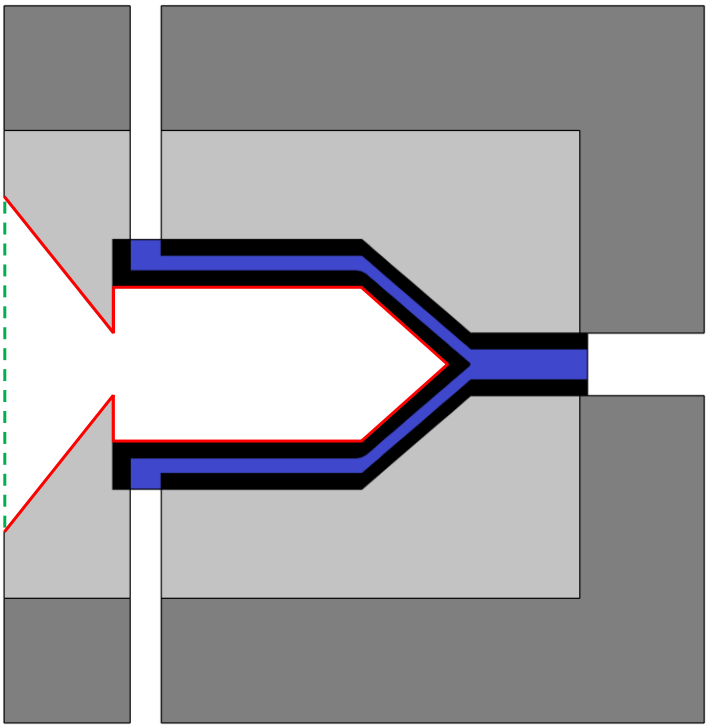

Figure 21. Depiction of boundary conditions used when simulating convection in the cavity. Temperature is prescribed at all surfaces outlined in red, while the dashed green line represents an open boundary condition. A volume force equal to that of gravity is applied acting downwards.

From the CFD simulations, the resultant convective heat flux is approximately 370 W, which corresponds to an effective heat transfer coefficient of 4.47 W/m^2-K on the inner surfaces of the receiver. Cross-sections of the gas temperature and velocity can be found below in Figure 22.

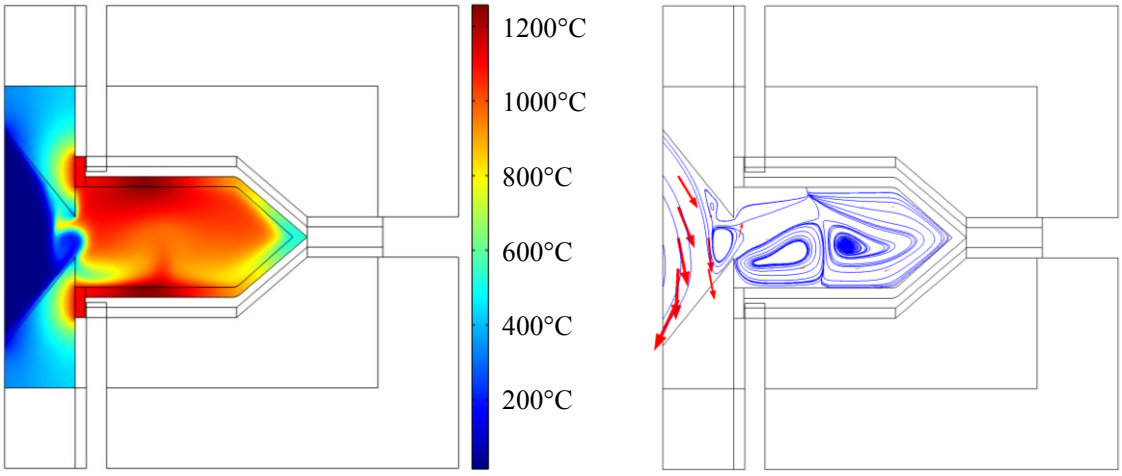

Figure 22. Temperature map of the gas within the receiver as well as solid bodies with which it is in direct contact (left) and velocity profile of gas within the cavity (right). Velocity magnitude shown using red arrows, and streamlines in blue. Gravity acts downwards.

Hot Spot Location

Because radiation scales with the fourth power of temperature, minimizing the view factor between the hottest portions of the receiver and the aperture will significantly reduce reradiative losses. However, the hottest portions are generally also those with a high view factor back to the aperture. This is because the portion of the receiver with a high view factor to the aperture will likely also absorb a high fraction of the incoming light. Thus, minimizing reradiation losses is non-trivial. Indeed, a significant amount of the design work on the receiver was focused around this particular task, and once we completed a sensitivity analysis of the U-tube receiver, every subsequent design was motivated at least in part by attempting to shift the hot spot location. The illustrations of the various receiver designs provided in Figures 7-10 are included below in Figure 23 for convenience.

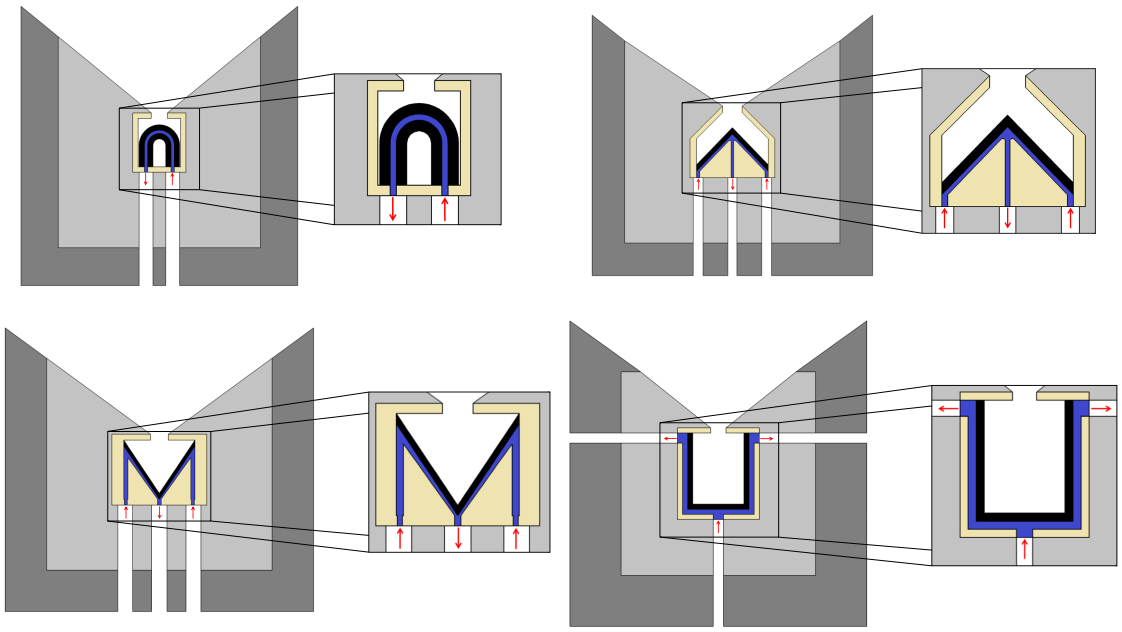

Figure 23. Illustrations of the four initial receiver designs.

We first realized the significance of hot spots when working on the U-tube receiver. Due to its geometry, a high percentage of the light incident upon the cavity heated the portion of the tube near the aperture, creating a hot spot at this location, which can be seen clearly in Figure 24. The hot spot in turn resulted in a significant amount of energy reradiating from the cavity.

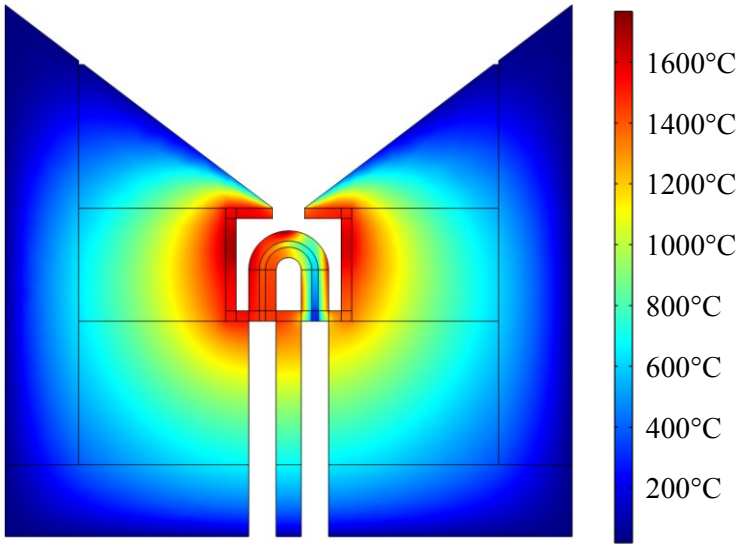

Figure 24. Temperature distribution of the U-tube receiver. Note the portion of the receiver near the top of the U-tube is at a temperature > 1,600°C.

The motivation for the design of the cone receiver was eliminating such a hot spot. Our intent was to cool the tip of the cone by rapidly flowing cold tin towards the tip, then letting it flow down the sides of the cone away from the aperture. Keeping the tip cool would in theory minimize reradiation, because the tip has a high view factor to the aperture. However, after running several simulations of the cone model it was found that the receiver would not work for two reasons: (1) the tin did not sufficiently cool the tip of the outer cone, and reradiative losses were not decreased significantly, and (2) the cold tin created a temperature gradient on the order of 1,000°C/cm near the tip, which we expect would cause failure due to the thermal stresses that would develop.

The design of the cone receiver was revised by reversing the direction of the tin flow. Doing so mitigated thermal stresses to a degree, because the tin is preheated as it flows up the sides of the inner cone. Once the tin reaches the tip of the cone, it is at a temperature close enough to the temperature of the outer tip that thermal gradients are not as extreme (see Figure 25 for the temperature profile). Additionally, a hot spot at the tip of the cone was actually found to be beneficial. This hot spot heats the tin further than in the original design, because it is closer to the tin exit point. In the initial design, for a given flowrate, the temperature of the outer cone near the exit point of the tin was ~1300°C, which limited the exit temperature of the tin to approximately the same temperature. Changing the flow of the tin so it exits the cone near a hot spot of ~1450°C allows the tin to reach temperatures in excess of 1,350°C. Once we discovered this effect, we determined there was an additional principle that should guide the design of the receiver: not only should hot spots have a small view factor to the aperture, but hot spots are actually necessary to achieve high efficiency. This exploitation of hot spots stands in

stark contrast to external receivers used in molten salt CSP plants, which operate at lower temperatures and attempt to keep the flux profile as uniform as possible to minimize thermal stresses. Furthermore, the highest intensity flux should be located near tin exit points, so the tin leaves at the peak temperature.

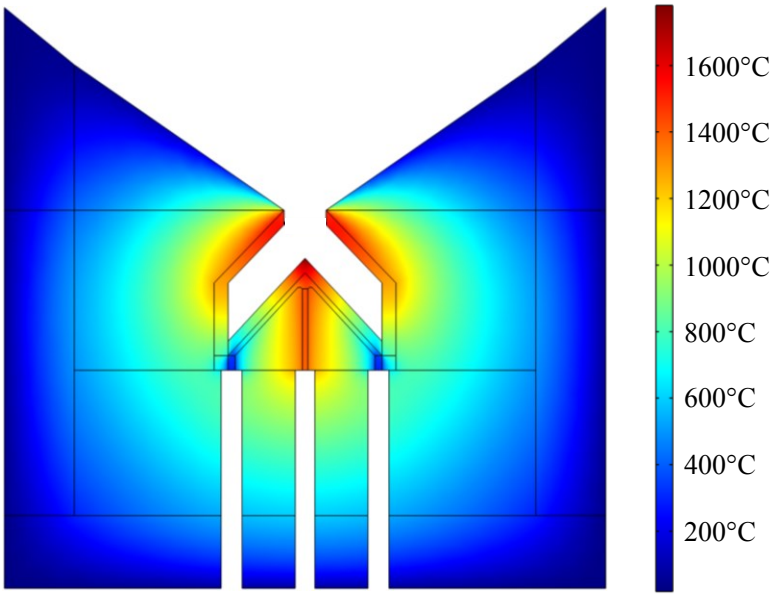

Figure 25. Temperature distribution of the cone receiver after the direction of flow was reversed.

The inverted cone design we developed was intended to reflect these general design principles. In this design, the hot spot of the receiver is near the apex of the cone, which is now far from the aperture. Because of the location of this hot spot (see Figure 26), the view factor is lower than for the standard cone design, and thus heat loss due to reradiation is decreased. However, as in the previous cone design, this design places the hot spot near the exit point of the tin, allowing the tin to reach higher temperatures than it would otherwise. While this receiver was able to achieve an efficiency of 82%, due to the geometry of the receiver, thermal stresses in excess of graphite's tensile strength developed in the receiver, necessitating a different design that manages to locate the hot spot near the exit with a small view factor back to the aperture.

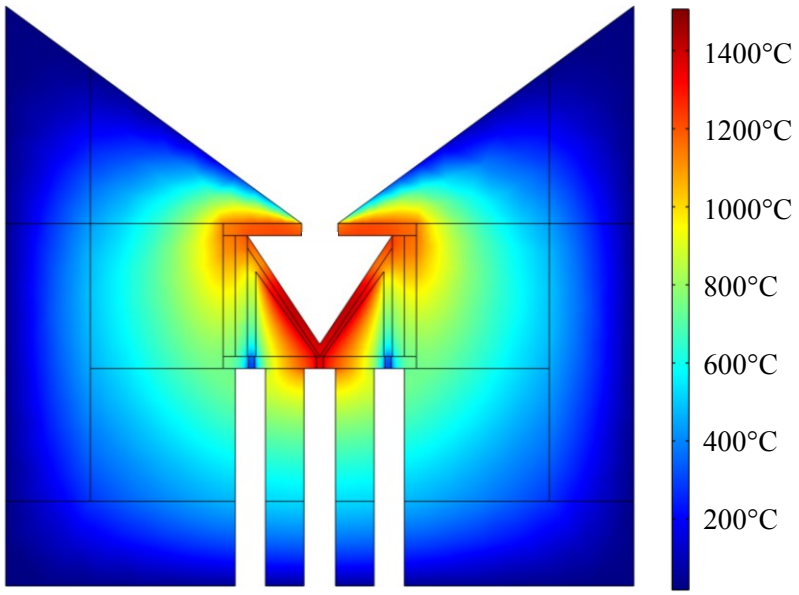

Figure 26. Temperature distribution of the inverted cone receiver.

The solution we developed was the cup receiver. In this design, a hot spot exists on the inner walls close to the lid (see Figure 27). This hot spot lies almost directly on top of the exit point of the tin, allowing the tin to be further heated. However, because the hot spot is so close to the lid but at an almost 90° angle to the aperture, the view factor to the aperture is small, reducing reradiation. The base of the receiver, which has a high view factor to the aperture, is kept cool by the tin flowing into the receiver. Tin is able to cool the base in this case because unlike the tip of the cone receiver, the base is sufficiently far from the aperture. Radiation from the aperture is diffuse enough that the base is not heated faster than the tin can cool it.

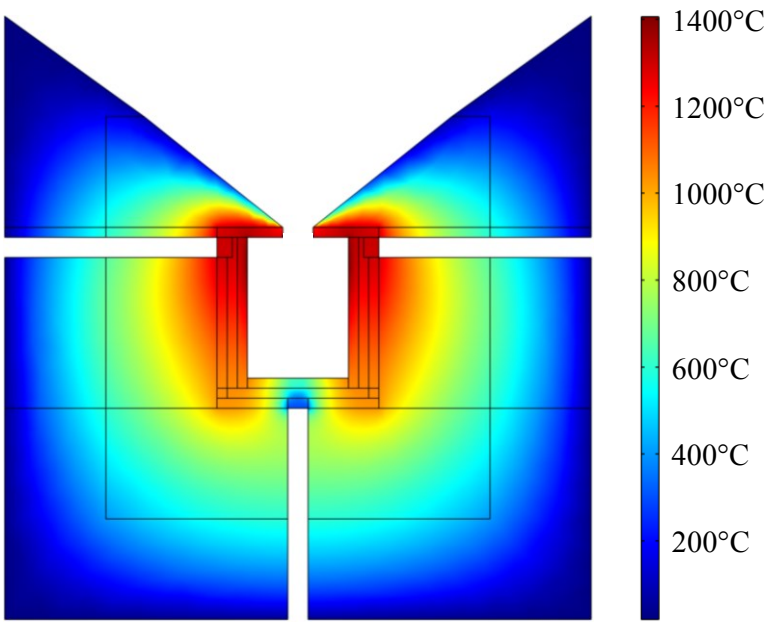

Figure 27. Temperature distribution of the cup receiver.

Cup-Cone Performance

The temperature profile of the cup-cone receiver, provided in Figure 28, is similar to that of the cup receiver and takes advantage of the temperature distribution observed in the cup receiver. The hot spot of the receiver is near the outlets of the receiver, and similar to the cup receiver, this hot spot is located in a location that has a small view factor back to the environment, minimizing reradiation.

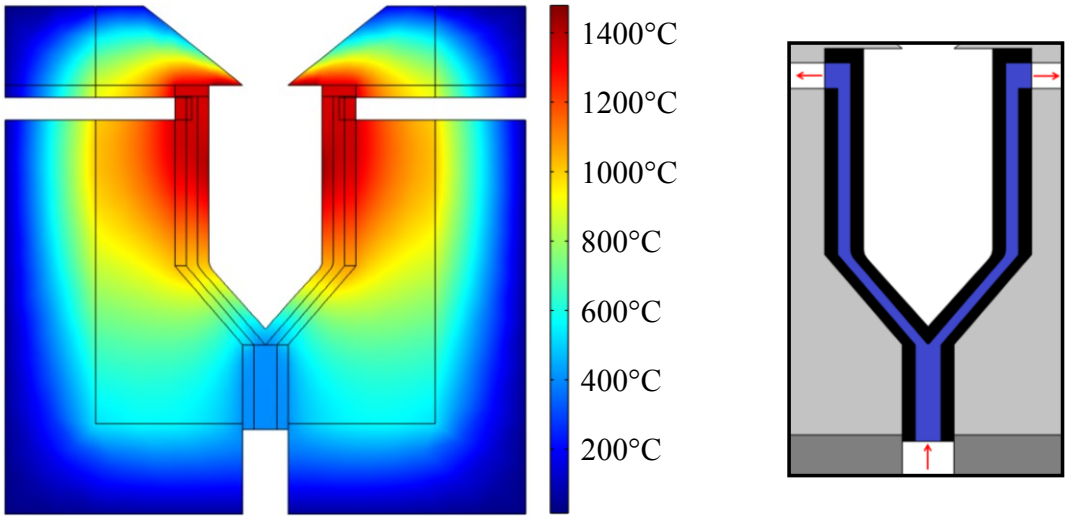

Figure 28. Temperature profile of the cup-cone receiver. The direction of flow through the receiver is provided here again for reference.

Results from cup-cone simulations are tabulated in Tables 3-5 below.

Table 3. Energy balance for the cup-cone receiver based on COMSOL models.

Parameter	Value (W)	% of Total Input
Total heat input	6,250	100
Increase in tin sensible heat	5,357	83.3
Cavity reradiation losses	483.2	7.73
Cavity convection losses	429.7	6.88
Conduction through insulation losses	373.1	5.97
Error (|total input – other values|)	144.1	2.31

Table 4. Temperature of various locations in the cup-cone receiver based on COMSOL models.

Location	Temperature (°C)
Inlet	300
Outlets (average)	1,350
Cavity peak temperature	1,494
Cavity average temperature	1,243
Average insulation outer surface	76.6

Table 5. Other relevant values for the cup-cone receiver based on COMSOL models.

Parameter	Value
Mass flowrate (kg/s)	2.18×10^{-5}
Average tin heat capacity (kJ/kg-K)	0.236
Effective insulation thickness (cm)	20
Effective insulation conductivity (W/m-K)	0.05

The discrepancy in Table 3 of 144.1 W between the total power input and the increase in tin enthalpy plus losses is due to the coarseness of the mesh used. Based on the results presented in Table 3, we estimated the efficiency of the receiver when tested at 1,350°C will be 83.3±2.3%. However, if we can successfully eliminate convection from the cavity, (i.e. drop the value of "cavity convection losses" to zero), the efficiency is expected to climb to 90.2±2.3%. Assuming the discrepancy of 144.1 W is due entirely to an over prediction of the temperature increase of the tin, we still estimate the receiver efficiency to be 81.0%, which is above our benchmark of 80%.

It is worth noting that little can be done to further minimize losses through the insulation. As has been shown already, increasing insulation thickness has virtually no effect. There is also little opportunity to reduce the thermal conductivity of the insulation further, since the zirconia insulation being used is one of the few insulations that can withstand the temperatures achieved by the receiver (>1,350°C), and the insulation's thermal conductivity is very low already (0.2 W/m-K). To the best of our knowledge, there is no other commercially available insulation that would outperform zirconia at 1,350°C. Similarly, the microporous insulation used here has one of the lowest thermal conductivities of any insulation currently available (0.01 W/m-K) for this temperature range, and it can be used up to 1,000°C. Thus, there is no straightforward manner to reduce the effective thermal conductivity of the insulation. Finally, we could attempt to reduce losses off the surface of the insulation. However, as we have demonstrated, doing so would require reducing both the convective coefficient and emissivity of the insulation to virtually zero, which we have no way of doing. We have also optimized the receiver

design, to the point where we do not believe that a significant decrease in cavity reradiation can be realized.

The most effective way of further improving the efficiency would then be to somehow reduce the convection from the cavity, which could be accomplished by using a forced-convective wall, often termed an air curtain, which limits the ability for the hot gas to flow out of the receiver aperture. Additionally, there is the option of using a lower thermal conductivity inert gas, such as krypton or xenon, though such gases are quite expensive compared to gases like nitrogen or argon.

Thermal Stresses

As mentioned previously, thermal stresses are one of the most important factors to consider when developing a receiver geometry. The receiver dimensions are on the order of 30 cm and the temperature change within the receiver is around 1,000°C; thus temperature gradients in the receiver are expected to be 50-100°C/cm. Such gradients may result in stresses in excess of graphite's tensile strength. Furthermore, in many of the initial geometries, this temperature gradient is compounded by the existence of sharp features that can act as stress concentrators.

Due to the number of other factors we investigated, thermal stresses were not initially considered when designing the receiver. Although the receiver must be designed so it is not overstressed when heated, initially we solely considered the thermal performance of the receiver to determine which heat loss mechanisms were most impactful on its efficiency. Once these factors had been quantified, we examined stress within the receivers to determine what factors most affect the structural integrity of the

receivers. Stress profiles for several different receiver geometries can be found in Figure 29 below.

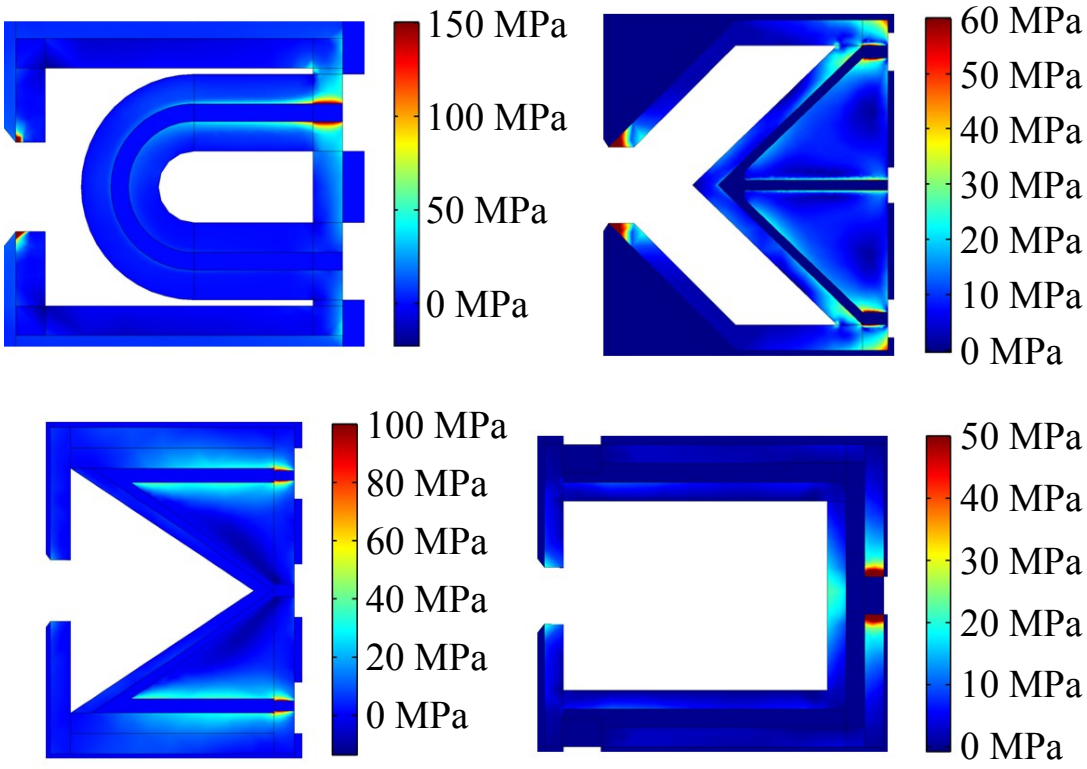

Figure 29. First principle stress profiles of the U-tube, cone, inverted cone, and cup receiver. Positive values indicate tensile stresses, while negative values indicate compressive stresses.

The maximum stress developed in each receiver is tabulated below.

Table 6. Maximum stress developed in each receiver geometry. Efficiency of each receiver is also provided.

Geometry	Maximum Stress (MPa)	Efficiency (%)
U-Tube	325	67.10
Cone	254	82.07
Inverted Cone	110	82.48
Cup	89	82.26

While successive iterations of the receiver resulted in lower maximum thermal stresses, even in the best case, i.e. the cup receiver, the stresses developed are still well in excess of graphite's tensile strength (43.0 MPa[97]). These stresses are most apparent at

two locations: the inlet, where cold tin flows into the receiver, and the aperture, where some light spills onto the aperture rather than passing through it. This localization of stresses can be seen clearly in the cup receiver. To address these issues, we modified the cup receiver, leading to the cup-cone receiver.

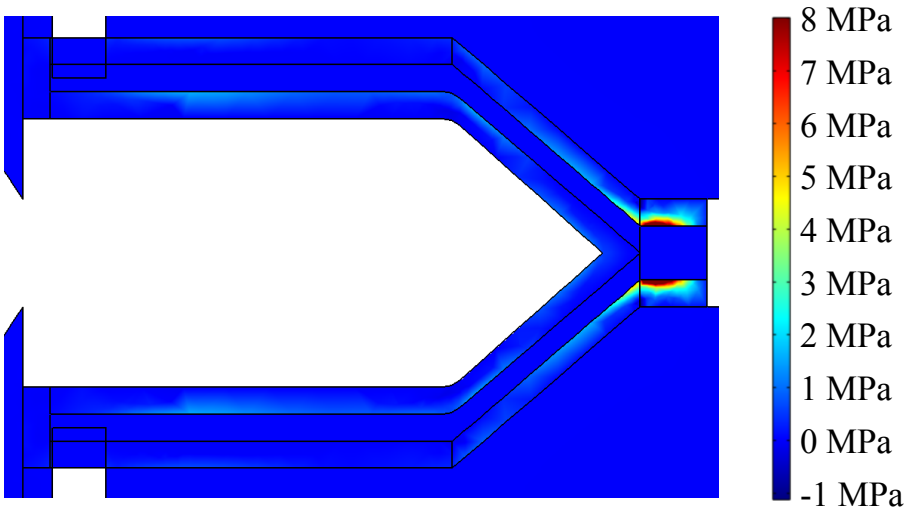

Figure 30 First principle stress profile of the cup-cone receiver. Positive values indicate tensile stresses, while negative values indicate compressive stresses. Note here the difference between the range in stresses for this receiver as compared to those in Figure 29.

The primary difference between the cup and cup-cone designs is the tapered inlet. As seen in Figure 30, this taper reduces thermal stresses near the inlet by an order of magnitude. Additionally, to address the thermal stresses near the aperture, we removed the graphite "lid" on the receiver, electing instead to use rigid insulation as the receiver lid to prevent reradiation.

The maximum stress expected in the cup-cone design is only 10.8 MPa. The tensile strength of the AR-14 graphite from which we fabricated the receiver is 43 MPa, which is 4.0 times the maximum stress developed in the cup-cone receiver, so the receiver is not expected to fail during testing. Furthermore, fatigue is generally not a concern for graphite, particularly when stresses remain below half the tensile strength of

graphite[99], and graphite generally does not creep at elevated temperatures[100]; thus, these two issues are not a concern in the planned experiments.

Summary

Several factors were found to have a significant effect on the performance of cavity receivers, while others had little to no effect. Neither the cavity dimensions nor the thickness of the insulation significantly affects the performance of the receiver. Additionally, modes of heat loss transfer at the surface of the insulation (i.e. convection and reradiation) are not limiting resistances, and the receiver efficiency is highly insensitive to either of these loss mechanisms. Finally, because the ratio of the aperture area to inner receiver surface area is so small, receiver performance is highly insensitive to the emissivity of the inner cavity surface. The exception is the case in which portions of a surface can be made with a reflectivity > 0.9, but doing so poses substantial challenges, particularly at 1,350°C.

While the emissivities of the insulation and cavity material are unimportant, the thermal conductivity of these materials can greatly affect the efficiency of the receiver. Our proposed combination of zirconia and microporous insulation is, to our knowledge, one of the best-performing insulating methods for extreme temperatures. The effective conductivity of these insulations in series minimizes thermal losses through the insulation, so the efficiency penalty is only 5-10%. Electing to construct the receiver out of graphite reduces the receiver efficiency by approximately 6% as compared to using a perfectly thermally conducting material. However, very few other refractory materials exist with a conductivity exceeding that of graphite, and we have determined that

graphite is one of the best commercially available and easily machinable materials from which to construct the receiver, particularly at small scales.

Two other factors that were found to significantly affect the performance of the receiver are convection from the receiver cavity and the location of hot spots within the receiver. Depending on the effective convective coefficient off the inner cavity surfaces, the receiver performance could either be virtually unaffected (if h < ~1 W/m^2-K) or impacted to the point that the receiver could not possibly achieve an acceptably high efficiency (if h > ~10 W/m^2-K). From CFD simulations, the effective convective coefficient is 4.47 W/m^2-K; in this case, convection from the cavity reduces the efficiency of the receiver by ~6%. The location of hot spots within the receiver dictates the performance of the receiver for two reasons. First, a hot spot with a high view factor to the aperture will result in increased losses due to reradiation from the cavity. Second, a hotspot close to the exit point of the tin allows the tin to be heated locally above temperatures achieved in the rest of the receiver. Thus, an optimal receiver geometry should be designed in such a way that hot spots form near the tin outlets but with a low view factor to the receiver aperture.

One final factor to consider is the thermal stresses developed in the receiver, though they do not directly affect the receiver efficiency. Many designs we considered result in stresses that are in excess of graphite's tensile strength. From this, we realized the receiver must be carefully designed to minimize thermal stresses. Various strategies can be employed to do so, including the elimination of sharp features, tapering the inlet region of the receiver, and creating a receiver "lid" made of insulation rather than graphite.

Taking into account all the considerations listed here, we developed the cup-cone receiver geometry, which addresses all the aforementioned issue, particularly locating hot spots in strategic locations and reducing thermal stresses within the receiver.

CHAPTER 5: EXPERIMENTAL SETUP AND PRELIMINARY RESULTS

A number of additional components are necessary to allow us to test the receiver. Once these elements were designed, we could perform initial tests on the receiver to validate the COMSOL simulations described in the preceding chapters and begin to assemble an experiment to test the receiver at high temperatures.

Receiver Setup

Although the geometry of the receiver itself has been determined, other challenges posed by the receiver must be addressed. Recombining flow from the receiver, rigidly supporting the receiver, and preheating the receiver so that tin flowing through the receiver remains molten are all factors to consider.

Outlet Recombination

After flowing through the annular space within the receiver, tin flows out of four separate outlets. It is desirable to maximize the symmetry of flow out of the outlets to keep the angular temperature distribution as uniform as possible. If the outlets are oriented to form a "+" shape, asymmetry would exist between the top, middle, and bottom outlets due to gravity, so instead, these outlets are oriented in an "x" shape (see Figure 31). Using an "x" orientation, a higher degree of symmetry out of the four outlets is achieved – in this case, asymmetry exists only between the top two and bottom two outlets.

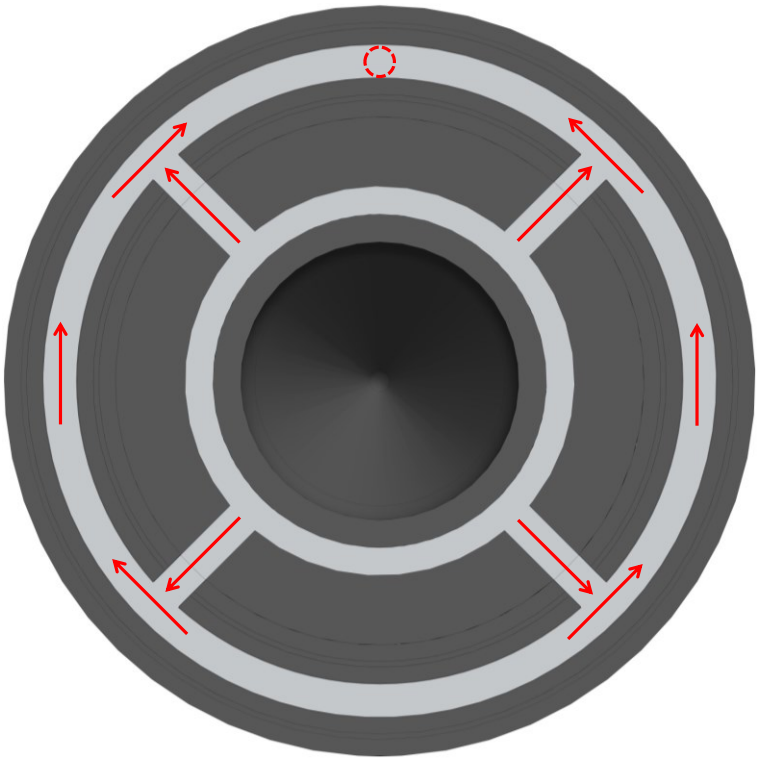

Figure 31. Cross section of the cup-cone receiver outlet network. Graphite is shown in black and tin in gray. Gravity acts downward. Direction of flow shown with red arrows. The recombined yin flows out of the receiver through a pipe located at the dashed red circle.

Once the tin has flowed out of the four outlets, it follows a circular path until it reaches an outlet pipe located at the top of the receiver. The outlet pipe is at the top of the receiver to ensure the receiver will fill entirely with tin, and no gas bubbles remain within the receiver.

Receiver Support

Structurally supporting the receiver is not a trivial matter. The support material should be highly insulating, as a less thermally resistive material will conduct a significant amount of heat away from the receiver, in turn decreasing the receiver efficiency. The material should also be chemically stable with respect to graphite. Any material used should be machinable, as it must be formed to hold the receiver. However, it must remain rigid at 1,350°C. Rigidity is particularly important because the receiver

must be located precisely with respect to the focal point of the HFSS. Materials that creep below 1,350°C, such as steel, would lead to the receiver losing alignment with the HFSS. At best, such misalignment would lead to a lower efficiency; at worst, misalignment could lead to a component of the experiment overheating and failing.

The material we selected to support the receiver is a rigid, machinable, yttria-stabilized zirconia (YSZ) insulation board. The board can be cut using any number of methods, included a CNC mill or a water jet, allowing for precise shapes to be easily machined. To support the receiver, we cut a semicircle from two pieces of rectangular board; the receiver sits in this semicircle (see Figure 32). Because the material is insulating, the supporting insulation located far from the receiver is near room temperature and can therefore be supported with conventional steel brackets.

Receiver Aperture

The "lid" for the receiver is subjected to several constraints, many of them similar to those of the receiver supports. The material is in contact with the portion of the receiver that reaches ~1,400°C and is subjected to the high intensity light that spills onto the surface of the lid near the aperture. It must keep its shape even at extreme temperatures. The material should also be easily machined, as the aperture dimensions must be precise. Too large an aperture will allow an unacceptable level of reradiation to escape from the cavity, while too small an aperture will not allow a sufficient amount of light to enter the cavity. Additionally, an aperture with too steep a taper will lead to some shading effects, because light comes in at an angle from the HFSS. For these reasons, we again elected to fabricate the lid from YSZ.

The lid was designed to sit on an additional zirconia board that served as a support in a manner identical to the receiver.

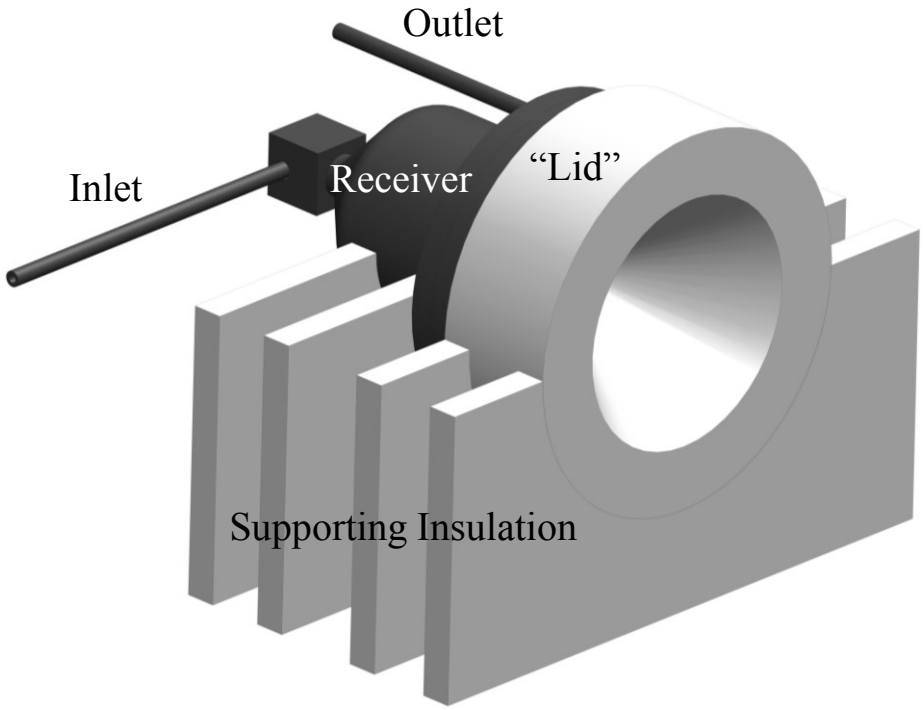

Figure 32. Schematic of the receiver with insulation support and aperture insulation, as well as inlet and outlet pipes.

Preheating the Receiver

When starting the experiment, it is desirable to flow tin through the receiver before turning on the HFSS, in order to prevent portions of the receiver from overheating. However, in this case the receiver must be preheated, or the tin inside it will not be liquid and cannot be pumped. Preheating is challenging, because most heat tapes are encased in a flexible fiberglass covering that becomes glassy above 480°C, beyond which the heat tape usually becomes unusable. Because of this temperature limitation, the heat tape would likely be a one-time use; however it is preferable be able to run multiple receiver tests, while allowing the receiver the cool between tests. To allow for multiple tests, we elected to use cartridge heaters rated for use up to 1,400°C. These cartridge heaters were

wrapped in a Nextel (composed of Al_2O_3, SiO_2, & B_2O_3) fabric covering that is rated up to 1,370°C. The cartridge heaters are not located at the hottest part of the receiver, so it is expected that neither the Nextel covers nor the cartridge heaters will exceed their recommended use temperatures. The coils we selected were sized appropriately so they are long enough to wrap around the receiver without being so long as to overlap ends. By packing soft alumina insulation around the receiver, the coils are held in place next to the receiver.

Compound Parabolic Concentrator Considerations

A compound parabolic concentrator (CPC) is a type of non-imaging optical concentrator. A typical CPC, such as the one depicted in Figure 33, is a reflective, hollow 3-D truncated parabola[101]. Light enters the wider end of the parabola and exits the smaller end. The light entering the CPC is more columnated (i.e. has a lower angular spread) than the light leaving the CPC. However, the concentration of the light is higher at the exit of the aperture. Referring back to Equation (3), more highly concentrated light will lead to an increased maximum attainable receiver efficiency.

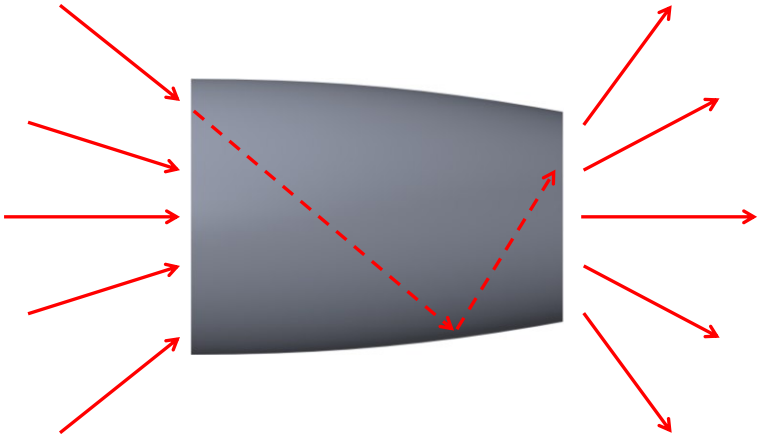

Figure 33. Illustration of a typical CPC. Light rays (shown in red) enter the left side of the concentrator and exit the right side. The path of one such ray within the CPC is shown using a dashed line.

It should be noted a CPC is the optimal geometry to increase optical concentration. Altering the geometry of the CPC by making it, e.g. hexagonal rather than circular, or making the taper straight rather than parabolic, can significantly reduce the maximum attainable increase in concentration[101].

In our application, the CPC is designed so its inlet diameter is equal to the diameter of the receiver aperture when a CPC is not used (4.7 cm). Because the outlet of the CPC is smaller than the inlet however, the effective aperture of the receiver can be reduced, which in turn leads to less reradiation escaping from the receiver and an improved efficiency. It is evident then that, all else being equal, using a CPC is desirable. However, due to thermal management and loss issues that are detailed below, we elected not to use a CPC.

Reflective Compound Parabolic Concentrator Design

Working with our colleagues at the University of Rochester, we designed a reflective CPC specifically for the HFSS detailed in the Monte Carlo Ray Tracing Methods section of Chapter 3, by taking into consideration the angular spread of light

from the seven lamps. This acceptance angle determines the maximum theoretical geometrical concentration ratio of a reflective CPC according to

$$C_{max} = \frac{1}{\sin^2(\theta)} \tag{18}$$

where C_{max} is the concentration ratio and θ is the half angle of the acceptance angle of incident light. For the case where all seven lamps are turned on, the acceptance angle is 48.4°, so the maximum concentration ratio is 1.8. Using a CPC to achieve the maximum concentration C_{max}, light rays reflect on the surface of the CPC an average of 0.986 times. If the CPC is made from a polished aluminum or silver reflector, and assuming no manufacturing related losses (e.g. imperfections in the surface of the CPC), the optical absorption in the CPC is approximately 5%, and losses due to reflection off the CPC are therefore equal to 1 – (0.95 x 0.986) = 3.65%.

The HFSS creates 6.25 kW of light within a disc with a radius of 2.35 cm. Approximating T in Equation (3) as the fluid exit temperature, Figure 34 shows the theoretical maximum receiver efficiency that can be achieved in this case, with and without a CPC. The plot assumes a perfect CPC with 100% reflectivity.

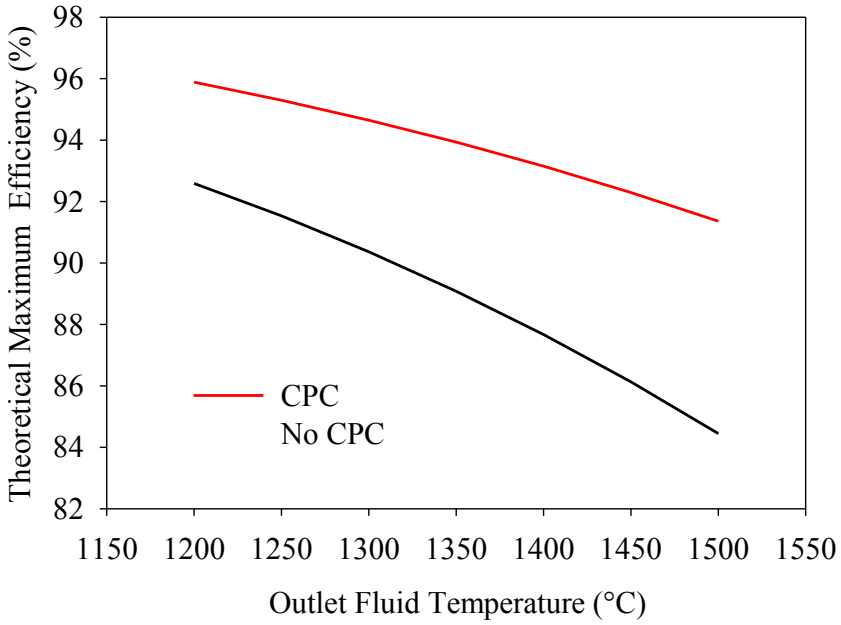

Figure 34. Maximum theoretical efficiency vs. maximum fluid temperature with and without a CPC, assuming perfect reflection.

It can be seen in Figure 34 that at 1,350°C (our target outlet temperature), using a CPC equates to a nearly 5% increase in the maximum theoretical efficiency. However, this value neglects several important considerations. First, the CPC is not perfectly reflective, and would not be entirely free of imperfections. Because the reflectivity of the CPC is only at most ~95%, the light lost due to the CPC would almost certainly exceed 5% of the total light entering the CPC, resulting in a negative impact on receiver efficiency. Second, from Figure 28, it can be seen that the hottest portion of the receiver assembly is the insulation around the aperture. To keep the CPC cool enough to prevent it from melting would require active cooling. Even assuming that a CPC would be feasible to implement, this active cooling would pull away additional heat such that even with a perfect CPC, the efficiency would suffer. For these reasons, we decided not to use a reflective CPC.

It is also worth noting that the estimated increase in efficiency using a CPC is based on the blackbody temperature of the cavity, which is estimated as the HTF exit temperature. However, based on COMSOL simulations, the actual blackbody temperature of the cavity was found be significantly lower, as the exit temperature is the hottest temperature within the cavity, and the flux of reradiated light from the cavity is lower than calculated for Figure 34. According to our modeling, reradiation from the cavity is only 35.6% that of a cavity that is uniformly at 1,350°C, corresponding to an effective cavity blackbody temperature of 981°C. In this case, the disparity between the performance with and without a CPC is even smaller, and the predicted improvement in efficiency is closer to 3.5%.

Refractive Compound Parabolic Concentrator Design

To address the issues presented by a reflective CPC, we considered using a refractive CPC. Refractive CPC's have the same geometry as reflective CPC's, but utilize total internal reflection (TIR) rather than reflection to concentrate light. Whereas a reflective CPC is hollow with reflective walls, a refractive CPC is a monolithic piece of a transparent dielectric material. This material is shaped in such a way that it would fill the empty space within a reflective CPC. By taking advantage of the difference in refractive index between the dielectric and the gaseous atmosphere, the refractive CPC mimics the manner in which a reflective CPC concentrates light with one major difference: because light entering the CPC undergoes refraction, a refractive CPC can achieve the same concentration ratio as can a reflective CPC with a larger acceptance angle than that of a reflective CPC. Alternatively, a refractive CPC can achieve a higher concentration than

can a reflective CPC for a given acceptance angle. In the case of a refractive CPC, the maximum concentration ratio is given by

$$C_{max} = \frac{n^2}{\sin^2(\theta)} \tag{19}$$

where n is the refractive index of the dielectric. Here, it is assumed the CPC is held in a gaseous environment with a refractive index of 1.

When considering a refractive CPC, there are few materials that can be used at the temperatures at which we plan to operate. One option we considered is quartz, with a refractive index of approximately 1.55. However, above 870°C, quartz becomes opaque, as it undergoes a phase transition from α-quartz to either α-tridymite or cristobalite depending on the conditions to which it is subjected[102]. Even assuming we actively cooled the quartz, if the active cooling were to fail in some manner and the quartz began to turn opaque, the incident light would lead to a runaway effect; as the quartz heats and becomes opaque, it would absorb more light, causing it to heat further above 900°C. For this reason, we instead considered making a CPC out of sapphire. Sapphire, the pure, crystalline form of α-alumina, has a refractive index of approximately 1.77, a melting point of 2040°C, and does not undergo a phase transition that causes it to become opaque. Furthermore, sapphire's conductivity of 30 W/m-K at room temperature is much higher than that of quartz. Such a high conductivity would help prevent the sapphire from forming hot spots and would potentially eliminate the need to actively cool it.

While sapphire does possess many ideal properties, it also presents several problems. Sapphire is at most only about 90% transmissive, and adding an anti-reflective coating to the CPC is not feasible, as the CPC would be extremely hot; active cooling is not an option, because sapphire is conductive enough that we would have to remove too

much heat from the system. At a transmittance of 90%, even the boost in performance afforded by the difference in refractive index (an improvement in concentration by about a factor of 3), is not enough to justify sapphire's use. We estimated that at best, the efficiency of the receiver would improve on the order of 1%. Furthermore, sapphire is costly to manufacture, especially because its surface must be polished to a very smooth finish. Between the monetary cost and the time necessary to find a way to incorporate the CPC into the system, we determined that there was too little potential benefit to justify the use of the CPC.

Another material worth considering is aluminum oxynitride (AlON). AlON is a transparent crystalline solid with a thermal conductivity of 12 W/m-K, a melting temperature of 2,150°C, and is stable in inert atmospheres. However, we did not look into using AlON for experiments at the laboratory scale, because the transmission losses are expected to be approximately equal to those of sapphire, so the CPC would still provide little to no benefit.

Gas Curtain

Our entire experiment is contained within a hermetically sealed box, so a window is necessary to allow light to cross the boundary of the box to reach the receiver. Due to the size of the window and the fact that light from the HFSS comes in at a wide angle, the receiver must be located in close proximity to the window, which could allow hot gases to escape the receiver cavity and directly convect to the window or the window seals. This in turn raises concerns about overheating the window's seals, which are not designed to exceed 200°C. Furthermore, because the window is silica, its thermal conductivity is low (1-2 W/m-K), and it is also quite possible that a large temperature

gradient could develop within the window, leading to it cracking. In both cases, a failure would mean a breach in the hermetic seal keeping oxygen out of the experiment, which would be problematic for a number of reasons, such as graphite and tin oxidation. To prevent the window from overheating, we constructed manifolds to create a gas curtain between the window and the receiver. The gas curtain consists of a blower, tubing, two manifolds (one output and one intake), and an intercooler. The manifolds, shown in Figure 35, are machined from a large hollow steel bar. Three tubes lead into each manifold, which helps keep flow along the entire curtain uniform. A slot was cut into each manifold to create a long, thin gas curtain.

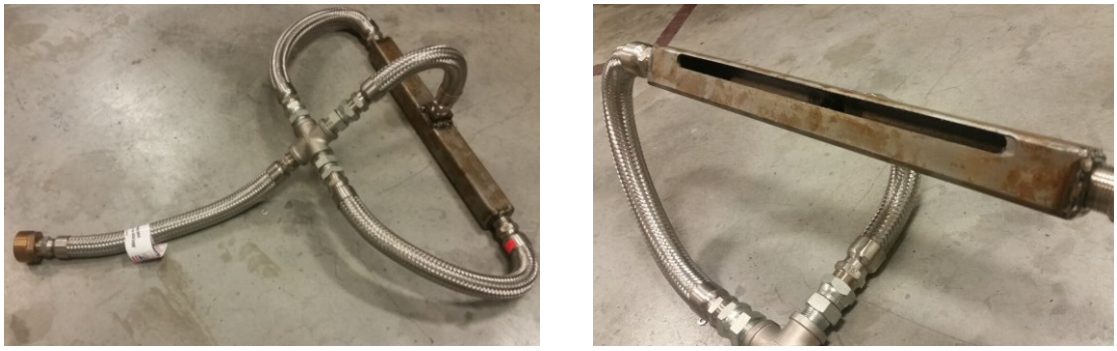

Figure 35. Manifold for the gas curtain. The three connections to the manifold can be seen in the left image, while the slot for gas output/intake can be seen in the right image.

These manifolds are mounted above and below the front face of the receiver. By blowing nitrogen out one manifold and pulling it into the other, a gas curtain can be created in front of the receiver. This concept is illustrated in Figure 36.

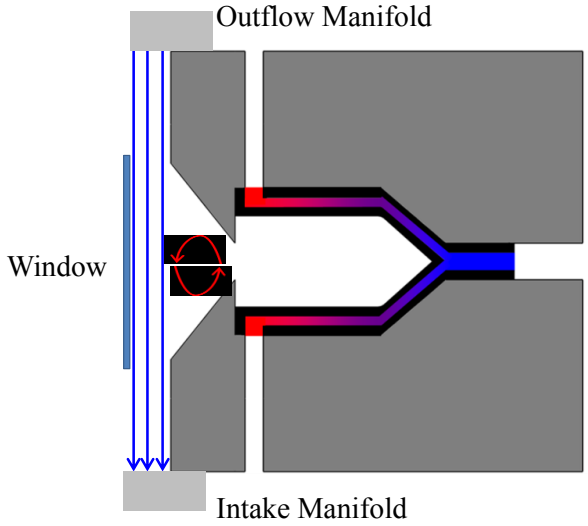

Figure 36. Illustration of how the gas curtain operates. Nitrogen flows from the outflow manifold to the intake manifold to create a streamline (shown in blue) that traps hot gases, preventing them from escaping the receiver.

Receiver Results

While we have yet to test the receiver using the HFSS, we have validated the COMSOL model of the cup-cone receiver subassembly. This validation was obtained using the heating coils that encircle the receiver. By controlling the coils (i.e. determining when and for how long they are turned on), then using COMSOL to reproduced the same heating conditions as the coils, we confirmed that the thermal behavior of the receiver is in good agreement with our models. Because these tests were performed in air, temperatures we kept well below 300°C, to eliminate any possibility of oxidation.

Heat-Up Procedure

Our first validation entailed heating the receiver from ambient temperature to approximately 220°C. During the heat-up procedure, the heating coils were set to independently maintain a temperature of 300°C, as measured by a thermocouple located in close proximity to each coil. However, we could not ensure the coils themselves

maintained a temperature of exactly 300°C. Factors such as overshoot and poor thermal contact between the thermocouples and the coils could very easily lead to a temperature reading not indicative of the actual temperature of the coil.

For this reason, we did not use a temperature boundary condition for the coils when modeling the receiver assembly in COMSOL. Instead, we used the output file generated by LabVIEW to determine each instance when a heating coil was turned on. Because we know the power of each heating coil (500 W), we created a simple input function that approximates the amount of heat generated by a coil at any given instant. Once we had determined this input function, we ran a transient simulation and compared the results with those obtained experimentally, as shown in Figure 37.

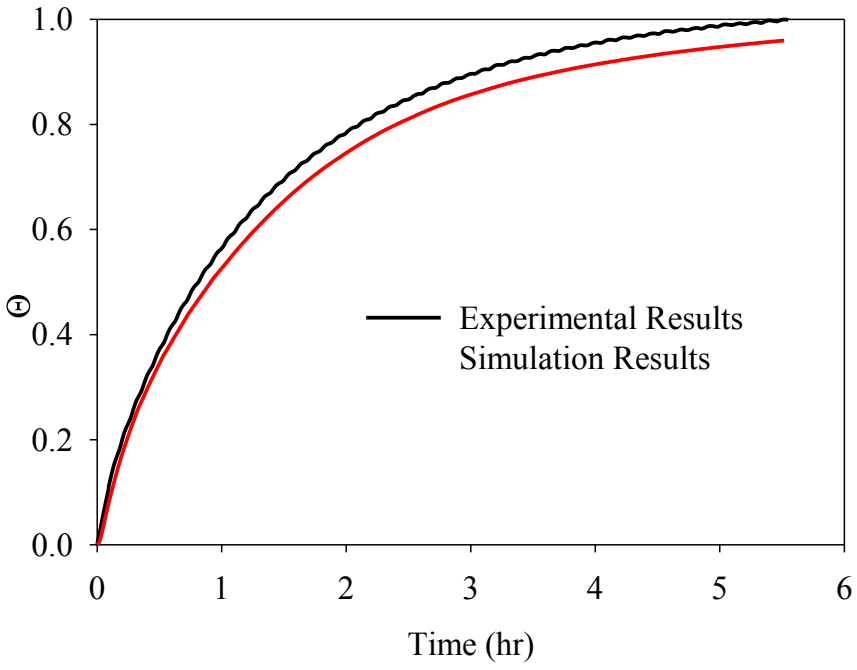

Figure 37. Experimental and simulation results of the heat-up procedure.

The discrepancy in final temperature between experimental and simulation results is 3.9%, which corresponds to a temperature difference of approximately 8°C. For

comparison, the margin of error of the thermocouples used 5°C, which alone could explain most of the discrepancy in the system. Even assuming the thermocouples are perfectly accurate, the discrepancy could be attributed to one or several other factors. The heat capacity of graphite was not measured and is not provided for the AR-14 grade of graphite we used for the receiver. Instead, we used approximated the heat capacity of the graphite based upon the heat capacity of fully dense graphite and the porosity of AR-14, so there is some potential for error due to this approximation. While we assume that the heating coils provide exactly 500 W of power, it is possible that the actual power provided is lower due to e.g. manufacturing imperfections, oxidation of the coils, or variations in the supplied voltage. In this case, if the coils provided 20 W (4%) less than they are supposed to, the entire discrepancy in temperature can be accounted for. Alternatively, it is possible that the effective convective coefficient estimated within the cavity is inaccurate. To approximate the convective coefficient, we scaled the convective coefficient at 1,350°C (4.5 W/m^2-K) by the difference in temperature to the ¼ power. As an example, at 200°C, the effective convective coefficient would be $4.5\left(\frac{200-25}{1,350-25}\right)^{1/4}$, or 2.9 W/m^2-K. It is worth noting the initial value of 4.5 W/m^2-K is itself an estimate based on fluid dynamics simulations, as described in Chapter 4. Finally, it is possible that the insulation allowed more heat to leak from the receiver than expected. It is also likely that more than one of these sources of error contributes to the discrepancy presented here. However, the agreement is sufficient and thus further quantification of these sources of uncertainty was not pursued.

Cool-Down Procedure

Once the heat-up procedure was completed, we held the receiver at steady-state for approximately 48 hours. After this time, the aperture to the receiver was plugged with insulation to eliminate any effects due to natural convection through the aperture, and the receiver was allowed to cool. By plugging the aperture and allowing the receiver to cool, we eliminated the two most likely sources of error in our simulation of the receiver heating up. Natural convection within the cavity no longer has an effect on the overall temperature of the receiver, and because the receiver is cooling, at no point are the heating coils turned on. As can be seen in Figure 38, the results obtained for the cool-down procedure agree quite well with those generated using COMSOL.

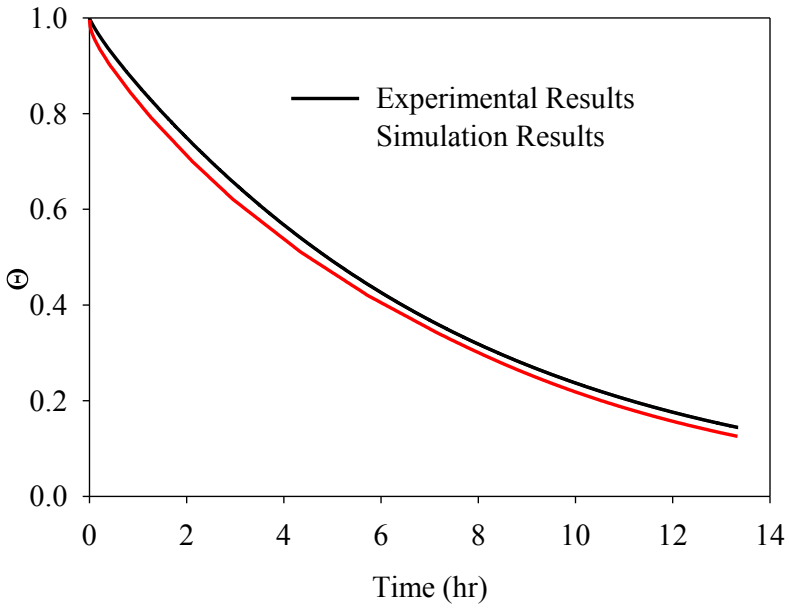

Figure 38. Experimental and simulation results of the cool-down procedure.

At the end of the simulation (~13.5 hours), the difference in predicted and measured temperature was less than 3°C, which is within the margin of error of the thermocouples used. Such agreement, both from the heat-up and the cool-down procedures, provides strong evidence that our simulations accurately model the physics

within the receiver. However, there is one portion of the physics that we modeled that was not tested using either transient simulation, namely reradiation from the cavity. To validate our treatment of the cavity reradiation, we performed additional validation while the receiver temperature was at steady state.

Cavity Reradiation Validation

To validate our modeling of cavity reradiation, while the receiver was at its steady-state temperature of approximately 220°C, we inserted a thermocouple into the cavity and allowed it to reach thermal equilibrium. We also measured the depth of insertion of the probe. The aperture was not plugged with insulation during this portion of the experiment, nor was it modeled as such when comparing to simulations. Our results were compared with those obtained from a COMSOL simulation, the results of which are shown in Figure 39.

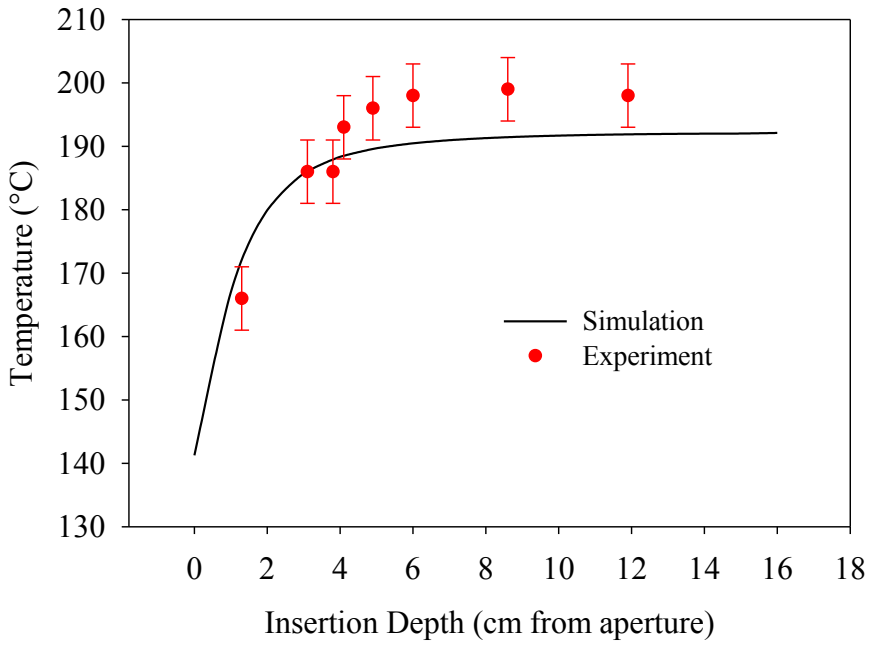

Figure 39. Experimental measurements and simulation results of cavity temperature at various locations.

We have included the error bars due to the uncertainty in the readings generated by the thermocouples (± 5°C). The discrepancy between measured and predicted results can also be ascribed in part to neglecting convection within the simulation. We expect convection from the receiver cavity would further heat the thermocouple slightly, which is consistent with the observed error in Figure 39. Furthermore, ensuring the thermocouple was perfectly aligned with the receiver proved difficult, so it is possible the location of the thermocouple tip was up to ~5 mm from where we expected it to be.

While the temperature does not match perfectly, the degree of accuracy displayed here is sufficient to validate how we treated reradiation within the cavity. Not only are the temperature measurements within 10°C of the predicted temperature, but the trend in temperature as a function of insertion depth is consistent between the simulated and experimental data. That this data matches up so well with COMSOL simulations is quite encouraging; at 1,350°C, radiation is generally the dominant mode of heat transfer, so our ability to accurately model radiation is critical to obtaining meaningful results.

Summary

Many components have been designed to create a full receiver sub-assembly. An outlet network was created to recombine flow from four individual outlets into a single stream. The recombination scheme maximizes the symmetry of the design, and eliminates gas bubbles within the receiver. Both the receiver support material and the receiver "lid" are constructed from rigid, insulating yttria-stabilized zirconia. This material minimizes heat losses without deforming at high temperatures. The receiver is wrapped with two heating coils, capable of handling temperatures up to 1,370°C. These

coils can used to preheat the receiver, which allows us to flow tin through the receiver before the HFSS is turned on.

Though we initially planned to use a CPC to further increase the concentration of light entering the receiver, after extensive analysis, we determined a CPC, whether reflective or refractive, would at best lead to a ~1% improvement in receiver efficiency, though it is very possible it would have a negative impact on the efficiency.

We have designed a gas curtain to reduce the flow of hot gases from the receiver cavity. By employing the gas curtain to reduce these convective losses, we expect to improve the efficiency of the receiver. Even in the case that the gas curtain does not improve the receiver efficiency, it may be necessary to reduce the amount of heat transferred from the receiver to the window, which is in close proximity to the receiver.

Several tests have been performed at temperatures below 300°C that validate our COMSOL modeling. Transient results from both heating and cooling the receiver are in close agreement between simulation and experiment, which indicates the effective thermal resistances within the COMSOL model are very close to the actual thermal resistances in our assembly. Furthermore, the temperature within the cavity due to reradiation from the inner cavity surfaces matches closely with the temperature profile predicted by COMSOL, further validating the model.

CHAPTER 6: UTILITY SCALE CONSIDERATIONS

While many of the findings presented here are useful for designing a receiver to test using a HFSS, several significant differences exist between design criteria for a small scale receiver and a utility scale receiver. Factors such as thermal stresses, optical concentration, and material selection must be reconsidered, as the effects at large scale are considerably different than those at small scales. However, the analysis presented for a small scale receiver was instrumental in determining what factors must be considered at large scales in the first place.

Here, we present some initial concepts of what a high temperature solar thermal receiver might look like at utility scale. Many of these concepts are still being refined, and there are several issues which have yet to be resolved. However, the ideas are provided here in their current state, with the intention to continue to improve their feasibility.

Heliostat Field Considerations

While concentrations in the range of 3,000-5,000 suns are attainable with a HFSS, reaching such concentrations when using a heliostat field is considerably more difficult. Current CSP plants operate at concentrations of approximately 800-1,000 suns, and there is not much that can be done to the heliostat field to increase concentrations further, due to limitations on tracking accuracy at reasonable costs. However, secondary concentration can be used to attain higher concentrations of sunlight.

Concentrations cannot be increased much beyond 1,000 suns primarily due to the fact that the sun subtends a solid angle of 6.7×10^{-5} steradians. Because the size of the

disc is non-zero, any image of the sun spreads in size after reflecting off a mirror. In the case of a flat mirror, the image increases in size by approximately 1 m per 100 m traveled[103]. Thus, a heliostat 1 m in diameter located 200 m away from the tower would create an image 3 m in diameter on the tower. For the largest CSP plants, the furthest heliostats are approximately 1 km from the tower, and the heliostats themselves are approximately 10x10 m. In this case, the minimum spot size of the heliostats on the receiver is about 20 m.

Such a large spot can quickly become an issue when attempting to reach extreme temperatures, since it decreases the concentration of incident light. Referring back to Equation (3), it is evident that achieving a high efficiency at extreme temperatures necessitates extremely high fluxes. In the limit that the weighted average blackbody temperature of the cavity is 1,350°C, a flux of approximately 4,000 suns is necessary to reach 90% efficiency.

By using an arguably optimistic estimate on the other hand, the temperature of the receiver could instead be assumed to vary linearly between the inlet and outlet temperatures. The average energy emitted by such a receiver, q''_{rad} can be found using the Stefan-Boltzmann law and the expression for average value of a function over an interval. That is,

$$q''_{rad} = \frac{\int_{T_{inlet}}^{T_{outlet}} \sigma T^4 dT}{T_{outlet} - T_{inlet}} \tag{20}$$

Assuming T_{inlet}=300°C and T_{outlet}=1,350°C, then q''_{rad}=121 kW/m^2, so 90% efficiency can be achieved with a flux of only ~1,200 suns. However, this estimate accounts only

for losses due to reradiation, and a DNI equal to 1,000 W/m^2. Factoring in other losses, efficiency will drop further, necessitating higher fluxes on the receiver.

It is not inconceivable that a receiver could be designed to reach temperatures of around 1,200°C with an efficiency of 85-90%. However, such analysis is outside the scope of this thesis. The remainder of this chapter will limit itself to discussing how to improve what may be broadly interpreted as a cavity receiver, with the intention of reaching temperatures of ~1,400°C.

To achieve the extreme concentrations necessary to efficiently operate at >1,200°C, both a smaller spot size and secondary concentration are necessary. We have determined that a spot size no greater than 3 m in diameter is best to achieve concentrations of ~5,000 suns; reaching such concentrations with a larger spot size is impractical, as sunlight in this case becomes too diffuse. Additionally, due to the spreading of the sun's image as it travels from heliostats to the tower, a small diameter heliostat field is necessary, as well as heliostats which themselves are much smaller than the current 10x10 m heliostats used in current CSP plants. We have developed an initial concept for a heliostat field capable of achieving higher concentrations and small spot sizes. The design of this field relies on Otherlab's Sunfolding heliostat design[104,105]. These heliostats are approximately 20x20 cm, which creates a much smaller spot size. In addition, for the proposed LMHTF based infrastructure, we propose a 500 m diameter field, which means the maximum spot size on the tower is approximately 3 m in diameter. An image of a single Sunfolding heliostat is included below in Figure 40.

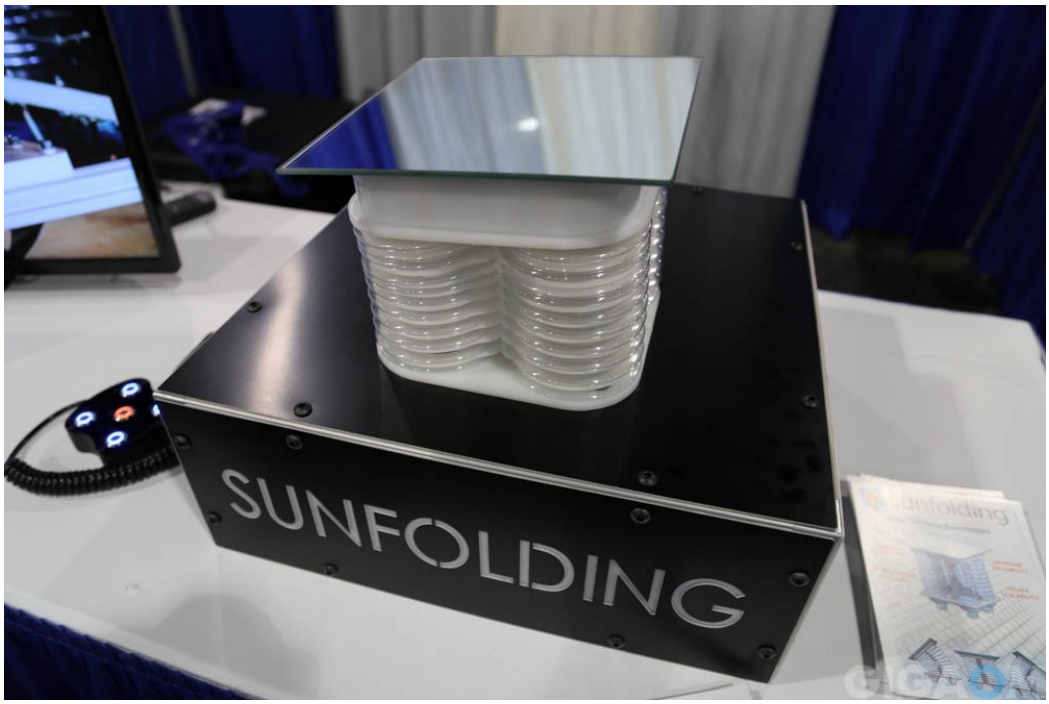

Figure 40. Sunfolding heliostat[106].

Compound Parabolic Concentrator Analysis

Before designing a receiver, we first wanted to ensure it is possible to reach a concentration of ~5,000 suns by using Equation (19). First, some simplifying assumptions are made about the heliostat field. We assume there are several "panels" of CPC's, with each panel subtended by a sector of the field. It is also assumed that in addition to a maximum radius for the heliostat field of 250 m, there is a minimum radius of 25 m. This ratio of maximum to minimum radius is determined heuristically, based on existing heliostat field designs. Using data from the System Advisor Model[107], we estimate the tower should be approximately 25 m tall, which results in an acceptance angle of at least 39° (shown as θ_{min} in Figure 41) subtended by the tower, no matter how many panels are used.

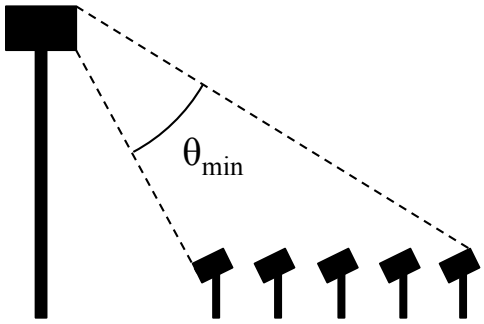

Figure 41. Illustration of the minimum angle achievable, for a given heliostat field and tower dimensions.

From this analysis, we determined the heliostat field should be divided into six sectors, each of which subtends a 60° wedge of the field. Subdividing the field in this manner means the maximum concentration attainable with existing heliostat technology and a reflective CPC is ~4,000 suns, and is ~12,500 suns with a refractive CPC, based on Equation (19). Using Sunfolding heliostats rather than existing heliostats, we expect attainable concentrations to increase by 50%.

While acceptably high concentrations can be achieved using only a reflective CPC, thermal management of the concentrators poses a problem. If a reflective CPC is in direct radiative "contact" with the receiver, a thermal management issues exist similar to those at the laboratory scale: the CPC can overheat, causing it to warp or melt. For this reason, a refractive CPC, made from a refractory material would be preferable. However, a refractive CPC is not without its drawbacks, as discussed in Chapter 5. Because the CPC accepts light from such a wide angle, the reflective losses off the surface of the CPC are considerable. Adding an AR coating necessitates keeping the front face of the CPC below of a temperature of ~200°C, and sapphire has a high thermal conductivity compared to most high-temperature materials. Furthermore, the CPC's will be directly exposed to the hottest portion of the receiver, as this is the portion that most benefits from

high concentrations of light. Thus, the issue of keeping the AR coating cool becomes substantial. We are still working to develop a solution to this problem but do not believe it to be insurmountable. Potential solutions include forgoing an AR coating and reducing the acceptance angle, or actively cooling the CPC's by blowing nitrogen over them.

One potential design employing CPC's is similar to that proposed by Schmitz *et al*.[108], who demonstrated the feasibility of a design using a panel of reflective CPC's to achieve concentrations of 1,300-1,600 suns. We have developed an initial design, which relies on hexagonal reflective CPC's to provide a small amount of initial concentration before light reaches the refractive CPC. These reflective CPC's are necessary because circles do not tessellate, and there is a considerable fraction of light (at least 9.3%) that would strike the area between CPC's and would essentially be lost. Because insulated refractive CPC's are located between the reflective CPC's and the receiver, keeping the reflective CPC's cool becomes a much simpler task. The ideal means by which to cool the CPC's is as-yet undetermined.

To reduce heat lost from the receiver, the refractive CPC is encircled with a layer of insulation. However, a small gap must be left between the insulation and the CPC. Because the index of refraction of the insulation is greater than 1, if the gap were not present, much of the light within the CPC would not undergo TIR, and would instead heat the insulation. The CPC is held in place by supports that have minimal contact with the CPC, because these supports are another location light could potentially be coupled out of the CPC, rather than undergoing TIR. An image of this multi-stage CPC can be found below in Figure 42.

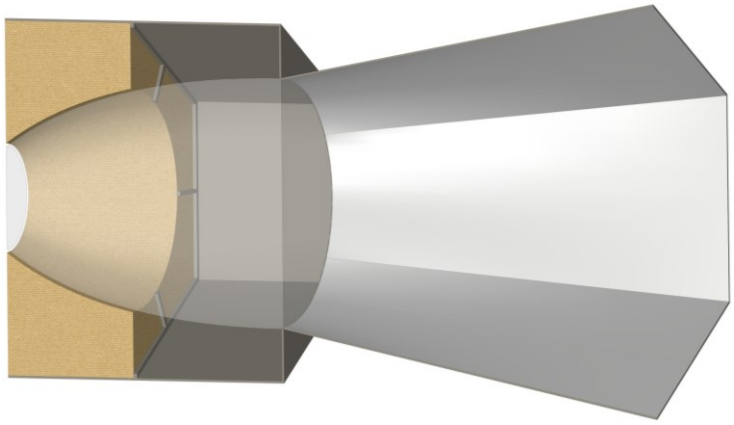

Figure 42. CPC assembly. The reflective stage is on the right, while the refractive stage can be seen on the left. The brown material surrounding a portion of the refractive CPC is insulation. Note the slight gap between the insulation and the refractive CPC.

Receiver Concepts

There exist many possible geometries for a utility scale cavity receiver. We have performed some design work on a few different potential receiver design concepts, which are presented here. Every concept relies on secondary concentration, achieved by a panel of the CPC's shown in Figure 42. The panels are placed around the receiver in a circular manner, as depicted in Figure 43. All light from a sector of the heliostat field would strike a single panel. The cluster of CPC's on that panel is designed to be larger than the spot size created by the heliostat fields, so all the light striking the tower can be collected.

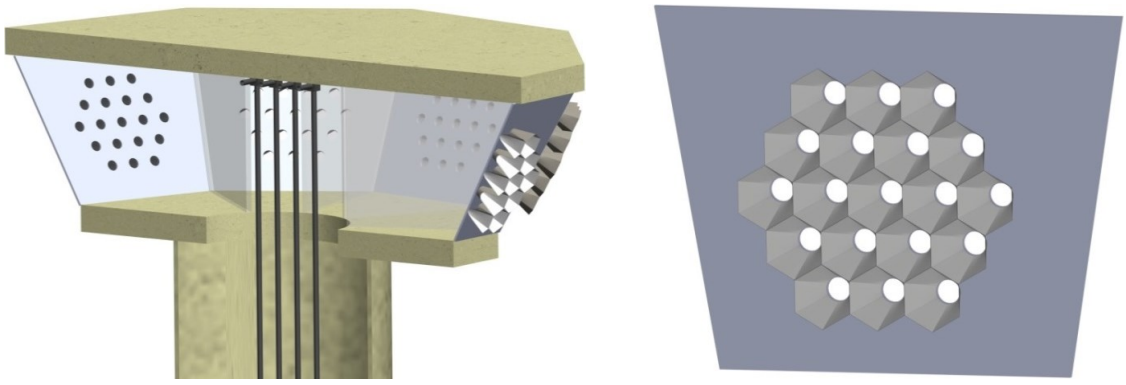

Figure 43. Depiction of a possible configuration for a cavity receiver (left), with a single CPC panel shown (right). Graphite pipes carrying tin are located at the center of the receiver and are heated by light coming in through the CPC panels.

One concept for a receiver is simply to surround several graphite pipes with these panels, which is the design shown in Figure 43. Another possible configuration for the receiver is to design several actual cavities, each of which absorbs light from a single panel. These cavities would be composed of banks of tubes, as creating the receivers from a single piece of graphite would be prohibitively expensive. This design is depicted in Figure 44 below. The advantage to this design is that the cavities would be modular, so in the event that a receiver were to fail, the plant could continue operation (albeit not at full capacity) until a scheduled shutdown.

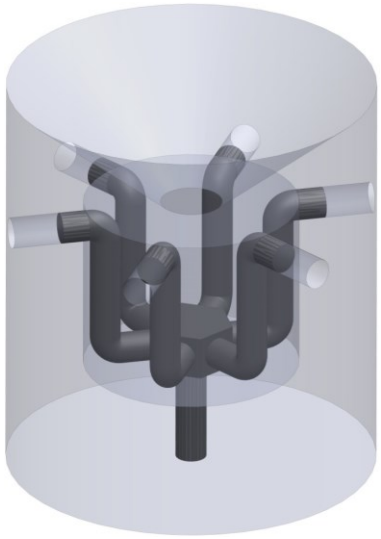

Figure 44. Modular receiver geometry. Graphite is shown in black, and the semi-transparent material surrounding the graphite is zirconia insulation.

Transient Considerations

One of the primary concerns regarding receiver performance is thermal stresses that develop due to transient effects. The most abrupt of these effects would be due to clouds passing overhead during a bright summer day. In this case, the radiative flux incident upon the receiver would effectively drop from 5,000+ suns to 0 in as little as 1-2 seconds. Such an abrupt change in the thermal input of the system could conceivably

create a large thermal shock in the receiver, leading to its failure. To test whether thermal shock would be problematic at scale, we performed transient simulations of the receiver depicted in Figure 44. The dimensions of the receiver are approximately 1.2 m in diameter x 1.3 m in height.

In this receiver design, tin enters the base of the receiver at 400°C and exits through six pipes, each with an outlet temperature of 1,350°C. To simulate a cloud coverage event, we first ran a COMSOL simulation to determine the temperature profile when the receiver operates at steady-state. Using these results as initial conditions, we then ran a transient simulation in which we instantly set the heat input to zero. Following this simulation, we ran a second simulation to determine the stresses at each point in time of the transient simulation. The maximum stress experienced by the receiver at any point was found to be only 7.33 MPa, considerably below the tensile strength of graphite. We therefore do not anticipate the receiver to fail due to thermal shock, issues with graphite fatigue, or creep, for reasons outlined in Chapter 2.

Structural Considerations

Not only does graphite have a low tensile strength (40-60 MPa) compared to many structural materials, but it is a brittle material, and very small displacements can cause components to fail catastrophically. For this reason, there are somewhat unique constraints placed on our system design. We generally want to avoid any design that includes large aspect ratio parts that have to support their own weight, as well as any features that can act as stress concentrators. Thus, long, slender tubes should be avoided where possible, as well as geometries that include sharp corners or other such features.

We have not yet performed extensive structural analysis of any of the designs presented here.

Summary

A utility scale receiver is still constrained by many of the same requirements as a laboratory scale receiver, but additional factors must be considered as well. Heliostat fields must be optimized for a given receiver, though we have not yet performed such an optimization. However, we have identified Otherlab's Sunfolding heliostat concept as a promising candidate to allow us to use secondary concentrators to achieve fluxes in excess of 5,000 suns. These fluxes can be achieved using a refractive CPC subtended by a 60° sector of the heliostat field. Two-stage CPC's, which first use a reflective then refractive stage, allow CPC's to be tessellated to reduce light spillage, while still achieving sufficiently high fluxes. Various geometries, including a bank of tubes or a modular design, are potential candidates for a utility scale receiver. Based on results obtained from COMSOL simulations, we believe even the largest thermal stresses due to transient effects are well below the fracture strength of graphite.

CHAPTER 7: CONCLUSIONS

CSP with integrated TES delivers dispatchable electricity similar to coal and natural gas but with no greenhouse gas emissions. Unfortunately, current molten salt CSP TES plants operating at 565°C with a 40% efficient power block cost approximately twice as much to produce electricity as do fossil fuel-based plants. Increasing operating temperatures to 1,350°C by using molten metal enables a 60% combined cycle efficiency and can potentially lead to significant cost reductions. The two main technical challenges with molten metal CSP are material compatibility and receiver efficiency.

We have developed a detailed model of a lab scale cavity solar receiver and performed a sensitivity analysis to determine what factors most affect its performance. The receiver performance is fundamentally limited by the concentration of light being emitted into the receiver. Receiver performance can be improved by using geometries that reduce the amount of reradiation emitted from the receiver cavity, as well as by locating hot spots near the exit point of the HTF. Furthermore, thermal conductivity is a critical parameter to consider. Both the receiver walls and the HTF should have a high (>10 W/m-K) conductivity to effectively transfer heat from the surface of the cavity to the HTF. Additionally, the insulation surrounding the receiver should have a low (<0.3 W/m-K) conductivity to prevent heat loss through the walls of the receiver. Convection from the cavity can also be a significant loss mechanism, though its effects are difficult to accurately quantify. There is however potential to reduce convection from the cavity by using a gas curtain or CPC.

Thermal stresses within the receiver can be substantial; indeed, they can easily exceed levels the receiver can tolerate by a factor of 5 or more. For this reason, the receiver geometry should minimize stress concentrators, and the receiver should be designed to minimize thermal gradients.

The receiver geometry we selected locates hot spots near the exit path of the tin, which allows the tin to be heated an additional ~50°C. These hot spots have a relatively small view factor back to the aperture of the receiver, which minimizes radiative losses. The aperture itself is constructed from a rigid foam-like insulation, rather than a stiff, rigid ceramic like graphite, and the inlet region of the receiver is tapered; both of these features reduce the thermal stresses developed in the receiver by an order of magnitude, ensuring the receiver will not fail due to thermal stresses.

Our COMSOL simulations indicate that an efficiency of 83% can be achieved with our cup-cone receiver with acceptably low thermal stresses. Work is under way to experimentally validate these predictions. Thermal experiments at lower temperatures match simulation data well, indicating that our models are accurate. In particular, we have demonstrated accurate estimation of the effective thermal resistance of the insulation surrounding the receiver, and our treatment of reradiation within the receiver cavity matches closely with experimental data.

When extending the results of this analysis to the design of a utility scale receiver, several differences are worth noting. Among these is the fact that the design of the receiver is now strongly dependent upon the cost of the materials being used. Furthermore, achieving concentrations of sunlight high enough to reach 1,350°C with an efficiency of greater than 80% requires improving current heliostat field designs. Thermal

stresses in a large scale receiver are still important to consider, but because the length scale is an order of magnitude larger, thermal stresses are generally not as significant at small scales.

APPENDIX A: ADDITIONAL HIGH FLUX SOLAR SIMULATOR DETAILS

The HFSS consists of seven identical xenon arc lamps and elliptical mirrors that are placed within the disc created by a 48.4° field of view of the CPC. Since each mirror's aperture is circular in shape, there is dead space in between the mirrors from which no light radiates. The 48.4° field of view is equivalent to 2.11 sr. One lamp spans an angle of 15.28° which is equivalent to 0.222 sr; in total, the seven lamps span 1.56 sr – only 73.5% of the total 2.11 sr solid angle a CPC designed for the HFSS could accept. Thus, if the same CPC and thermal system were to be used in the sunlight, a parabolic mirror could be designed to fit within the 48.4° field of view of the CPC and the system would be able to accept light from the total 2.11 sr solid angle, creating a higher performing system.

The angular spread of the sun is 0.5°. The maximum angular spread of the xenon arc when the light reaches the elliptical primary is 1.77°. This discrepancy is compounded when the light passes through the CPC; due to the law of conservation of étendue, the area of light is compressed to a small size while the angular range of light is spread out by a factor equal to the geometrical concentration. The difference in radiance between the HFSS's Osram xenon arc lamps and the actual sun leads to a variation in performance.

The distribution of flux is determined by the HFSS, and has been modeled in LightTools to match the HFSS's flux profile at both the University of Florida and the University of Minnesota. The model includes the seven Osram xenon arc lamps and their

ray data as measured by Zemax in their Radiant Source Model, with corresponding elliptical mirrors, a secondary CPC, and the cavity and receiver.

The spectrum of the xenon arc lamps must also be taken into consideration, because each wavelength interacts with materials differently. Each material examined in this report has specific reflection, absorption, and transmission properties that vary with wavelength. For the model in LightTools, the Radiant Source model used was a 6,000 W xenon bulb used, and the xenon arc lamp spectrum was applied to some of the simulations. For other simulations in which total power was the variable of interest, we used a gray approximation. The integral of these weighted values results in a percent absorption or reflection for the total power hitting a given material.

APPENDIX B: DERIVATION OF THE APPROXIMATE EFFECTIVE EMISSIVITY FOR A BLACKBODY CAVITY

Consider a single ray of light that passes through an aperture into a blackbody cavity. Upon striking a surface, the probability of the ray being reflected, rather than absorbed, is $P = (1 - \varepsilon)$. As a simplification, assume that when the ray is reflected inside the cavity, it has an equal chance of striking any other location inside the cavity, regardless of cavity geometry. In this case, the probability of the ray "striking" the aperture (i.e. being reflected out of the cavity) upon reflection is $Q = \frac{A_{aperture}}{A_{aperture}+A_{cavity}}$. On average then, the number of reflections that will occur before a ray is reflected out of the cavity is $1/Q$. In this case, the total probability a ray is reflected out of the cavity, rather than being absorbed, becomes $P^{1/Q}$. To calculate the probability a ray is not reflected out of the cavity, the value is simply $1 - P^{1/Q}$, which can be written as $1 - (1 - \varepsilon)^{\left(\frac{A_{aperture}+A_{cavity}}{A_{aperture}}\right)}$. This value (the probability the ray is not reflected out of the cavity, but instead absorbed) is by definition the effective absorptivity of the cavity.

APPENDIX C: FULL DATA FOR THE RECEIVER GEOMETRY ANALYSIS

Below are tables for each of the cases simulated in which flux was imported from the University of Rochester. Receiver material (shown as graphite in Figures 7-10) for each case is the same across rows in the following tables, while cavity material (shown as mullite in Figures 7-10) for each case is the same across columns. The effective emissivity of ZrC-W was modeled as 0.45, while the effective emissivity of graphite was modeled as 0.8.

U-tube Data

Table 7. Efficiency of the U-tube receiver with a CPC at 7,000 W incident light concentrated to 10,000 suns.

receiver \ cavity	ε=1	graphite	ZrC-W	ε=0
ε=1	66.76	67.03	67.57	69.18
graphite	67.51	67.10	67.51	69.41
ZrC-W	66.47	66.49	66.60	67.87
ε=0	65.36	65.14	64.37	-0.22

Note that when both the receiver and cavity are entirely reflective (ε=0), efficiency drops to a negative value, as no heat is absorbed from the sun, and a small amount of heat is lost through conduction from the cavity to the environment.

Receivers other than the U-tube receiver were tested in four different: the input power was either 7,000 W or 9,000 W, and either a perfect reflecting CPC was used, or it was not.

Cone Data

Table 8. Efficiency of the cone receiver with a CPC at 7,000 W incident light concentrated to 10,000 suns.

cavity / receiver	graphite	ZrC-W
graphite	84.96	85.74
ZrC-W	83.52	83.98

Table 9. Efficiency of the cone receiver without a CPC at 7,000 W incident light concentrated to 5,500 suns.

cavity / receiver	graphite	ZrC-W
graphite	82.07	84.90
ZrC-W	81.69	82.25

Table 10. Efficiency of the cone receiver with a CPC at 9,000 W incident light concentrated to 5,200 suns.

cavity / receiver	graphite	ZrC-W
graphite	81.53	81.88
ZrC-W	80.42	82.57

Table 11. Efficiency of the cone receiver without a CPC at 9,000 W incident light concentrated to 3,200 suns.

cavity / receiver	graphite	ZrC-W
graphite	61.74	84.43
ZrC-W	82.14	85.44

Inverted Cone Data

Table 12. Efficiency of the inverted cone receiver with a CPC at 7,000 W incident light concentrated to 10,000 suns.

cavity / receiver	graphite	ZrC-W
graphite	85.24	85.51
ZrC-W	81.52	82.15

Table 13. Efficiency of the inverted cone receiver without a CPC at 7,000 W incident light concentrated to 5,500 suns.

cavity / receiver	graphite	ZrC-W
graphite	82.48	82.84
ZrC-W	77.77	78.24

Table 14. Efficiency of the inverted cone receiver with a CPC at 9,000 W incident light concentrated to 5,200 suns.

cavity / receiver	graphite	ZrC-W
graphite	53.12	53.08
ZrC-W	71.26	71.65

Table 15. Efficiency of the inverted cone receiver without a CPC at 9,000 W incident light concentrated to 3,200 suns.

cavity / receiver	graphite	ZrC-W
graphite	76.30	76.44
ZrC-W	69.77	69.81

Cup Data

Table 16. Efficiency of the cup receiver with a CPC at 7,000 W incident light concentrated to 10,000 suns.

cavity / receiver	graphite	ZrC-W
graphite	75.66	75.37
ZrC-W	76.94	77.50

Table 17. Efficiency of the cup receiver without a CPC at 7,000 W incident light concentrated to 5,500 suns.

cavity / receiver	graphite	ZrC-W
graphite	68.86	72.69
ZrC-W	73.59	74.16

Table 18. Efficiency of the cup receiver with a CPC at 9,000 W incident light concentrated to 5,200 suns.

cavity / receiver	graphite	ZrC-W
graphite	71.94	71.90
ZrC-W	71.37	71.22

Table 19. Efficiency of the cup receiver without a CPC at 9,000 W incident light concentrated to 3,200 suns.

cavity / receiver	graphite	ZrC-W
graphite	66.45	66.64
ZrC-W	65.95	66.09

APPENDIX D

While much attention has been given to the various aspects of designing the receiver, a large amount of ancillary equipment is necessary to test the receiver. This appendix will discuss these ancillary components, and the experimental challenges associated with their design.

There are a number of such ancillary components. We have included a description of many of these components. The details of several other components can be found in reference [50], but they are briefly described here.

Additional Experimental Components

Because tin is being flowed in a closed-loop, one of the most obviously necessary components of our system is a series of heat sinks to continuously remove the heat added to the system by the HFSS. If tin is to consistently enter the receiver between 300-400°C, it must be cooled at a rate of approximately 6 kW (equal to the increase in sensible heat of the tin as it flows through the receiver). The goal of the heat sinks is simply to cool the tin, and unlike a heat exchanger, exergy preservation is of no importance. Thus to enhance the rate of heat transfer, the cold side of the heat sinks is kept close to ambient temperature (~25°). We designed two separate heat sinks – one to cool tin from 1,350°C to ~800°C, and a second to cool tin from ~800°C to 300°C. To avoid thermally stressing the high temperature heat sink, it was designed to radiate heat from the hot side to the cold side. The low temperature heat sink consists of a graphite plenum through which tin flows in direct contact with a steel plenum, through which heat transfer oil flows. These

heat sinks also include cartridge heaters, which can be used to add heat back to the tin in the case that the heat sinks over perform.

When gluing together graphite pipes, it is critical to ensure that the pipes are not blocked by excess glue. To accomplish this, cylinders of tin are created to "plug" the pipes. Using these plugs prevented glue from filling the pipes, and the tin plugs simply melt when it is time to pump tin through the pipes.

To address possible tin leaks from our system, we used a galvanized steel collection pan. This pan is a large flat sheet of steel with the edges bent upwards. Tin that hits the steel solidifies, both because it is cooled by the pan and because it alloys with the zinc coating the steel to form a Sn-Zn compound with a higher melting point.

Layout of Full Experimental Setup

Because the experiment takes place in a sealed box, the tin used must be constantly recirculated through the experiment. Additionally, the experiment is entirely self-contained, so any components to be used with the experiment must be located within the box and operate without direct human contact. Figure 45 below shows all the main components within the box. The flow path of the tin is as follows: reservoir → pump → receiver → high temperature heat sink → low temperature heat sink → flowmeter → reservoir.

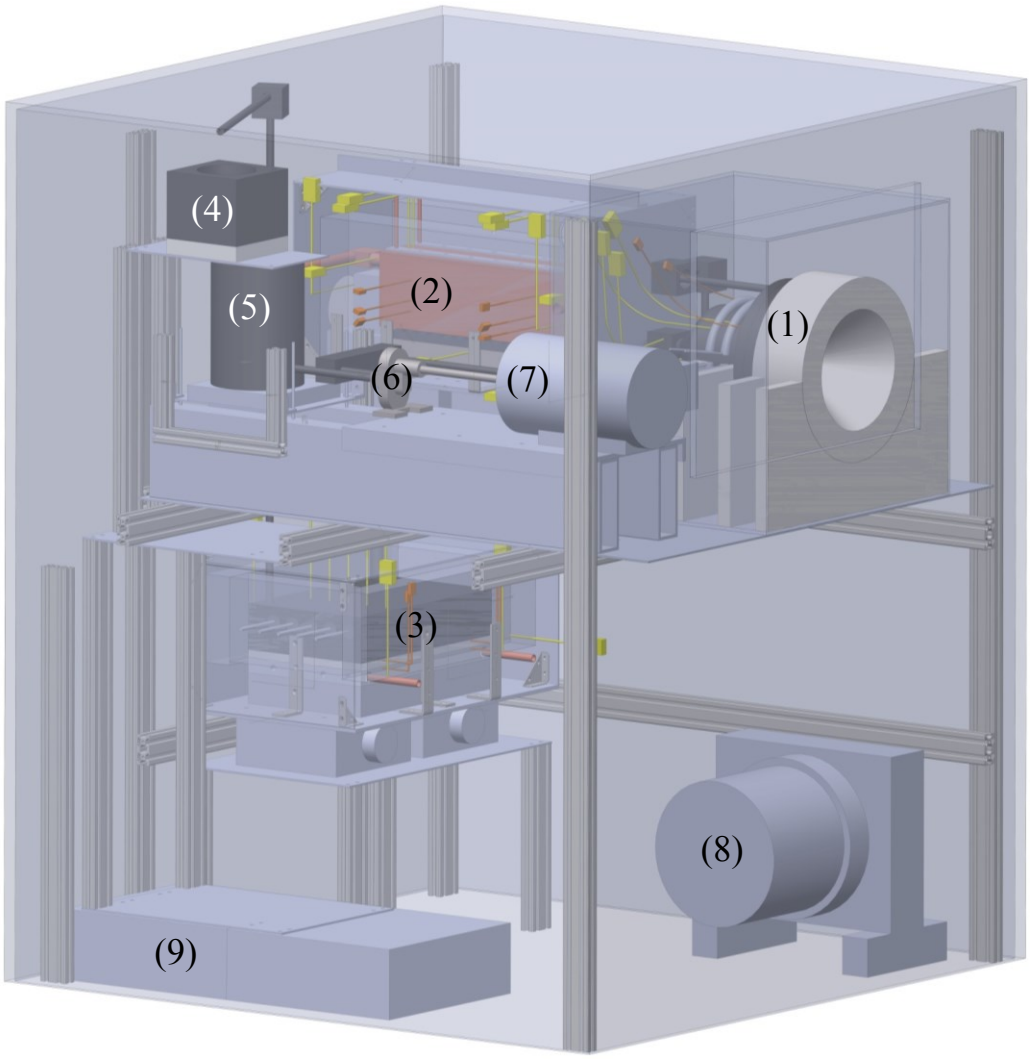

Figure 45. Layout of all major components of the experiment. Components are (1) the receiver, (2) high temperature heat sink, (3) low temperature heat sink, (4) flowmeter, (5) tin reservoir, (6) pump, (7) pump motor, (8) nitrogen fan cooler, (9) scales upon which the flowmeter sits. The entire experiment is housed inside a large, hermetically sealed steel box. Some structural members have been removed to avoid obscuring components listed here.

These components serve various purposes within the experiment. The reservoir is necessary because when the pump is stopped, some tin will drain from the highest locations in the loop, and the reservoir can hold this additional tin. It also supplies extra tin, in case some tin is lost through a slow leak. The purpose of the pump and the motor is to move tin continuously through the system at a controllable flow rate. As mentioned previously, the heat sinks are necessary to remove the heat input into the tin by the HFSS

and prevent a thermal runaway. The flowmeter allows us to determine the rate at which tin flows; this flowrate is measured indirectly using scales. More information about the method by which flowrate is measured can be found in the section "Flowmeter Design" later in this chapter. One additional component necessary for the experiment is a fan cooler. This cooler has cold oil flowing through it, which is pumped in from outside the box and cools nitrogen within the box. The fan cooler is necessary, because despite our best efforts, some heat will escape into the gas atmosphere within the box. The fan cooler allows us to prevent components within the box (such as the scales, motor, and box seals) from overheating due to convection of nitrogen from high temperature components.

Mechanical Support Frame

In addition to constructing many system components from graphite, the piping network connecting these components was constructed from graphite. However, because graphite is a very stiff, brittle material, even slightly displacing a pipe could potentially crack either the graphite or the glue connecting pieces of graphite, which would in turn lead to tin leaking from the system. To address this issue, we wrapped graphite pipes in heat tape and insulation, then lashed them to aluminum structural supports. The insulation prevented the aluminum from overheating, and attaching the pipes to the aluminum prevented them from moving.

The aluminum supports used are extruded 80/20 structural aluminum. We did not attach these supports directly to the nitrogen containment box, because doing so would require punching holes in the walls of the box, which is a potential location for a nitrogen leak to form. Instead, we constructed a mechanical support frame (MSF) from 80/20 aluminum. (The aluminum extrusion comprising this MSF can be clearly seen in Figure

45.) Not only does this MSF allow us to attach rigid support for various pipes in our experiment, but it also serves as a support structure for the “hot table”, upon which the reservoir, pump/motor, receiver, and high temperature heat sink sit. An image of the MSF can be found in Figure 46.

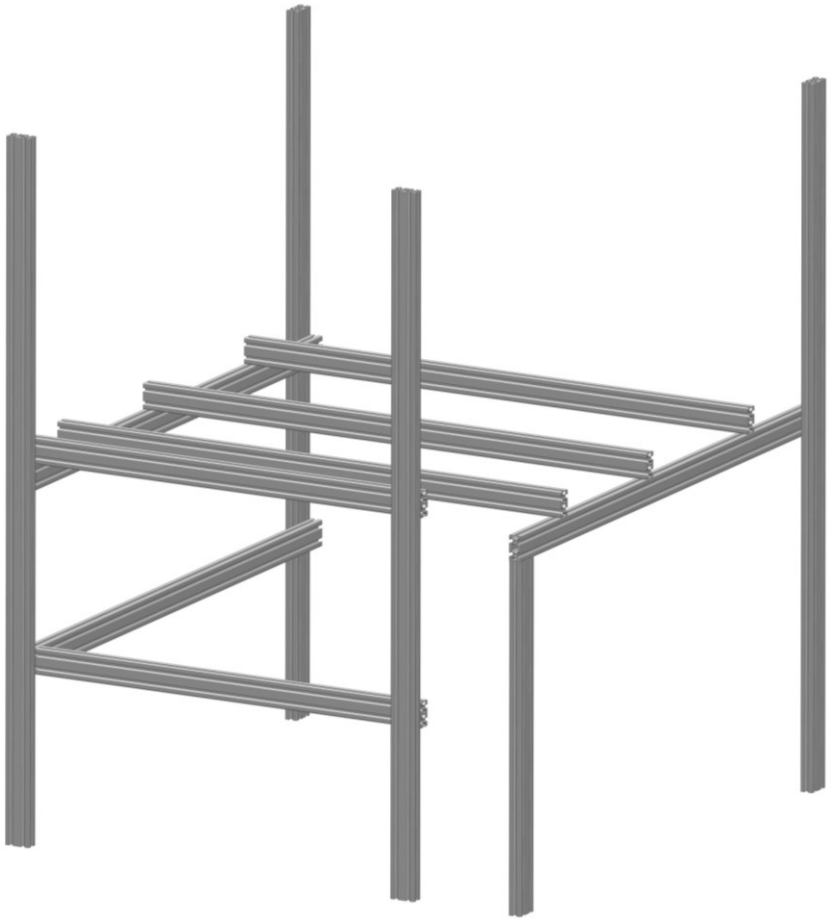

Figure 46. MSF design.

The orientation of the MSF is the same as in Figure 45.

Window Coatings

The HFSS at Georgia Tech delivers approximately 6.25 kW of heat, predominantly in the visible and infrared regions of the EM spectrum (see Figure 47). While the window we will be using is transmissive in these regions, it is expected to

absorb or reflect 5-10% of the incident light, which amounts to 300-600 W of heat. These losses impact the performance of the receiver negatively, as less heat goes in to heating the tin.

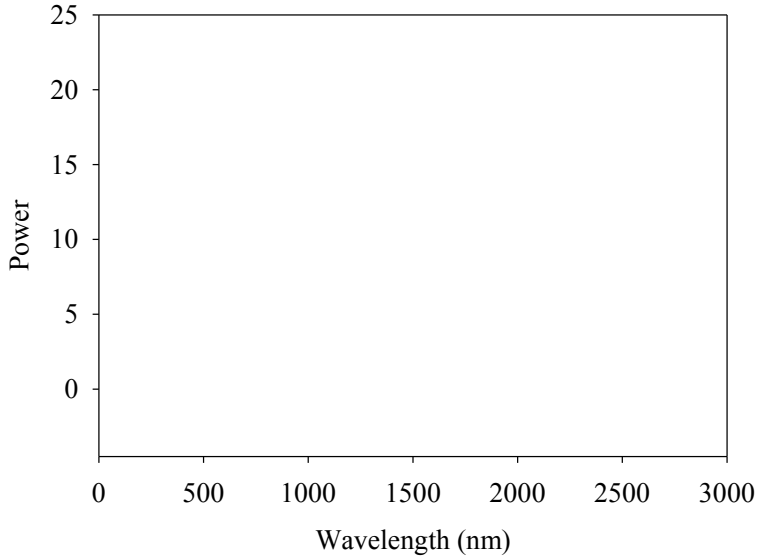

Figure 47 Emitted power from a xenon arc lamp as a function of wavelength. Power is given in arbitrary units.

To reduce the fraction of light absorbed and reflected by the window, we coated it with #289EX 400-1700 nm anti-reflection (AR) coating from Evaporated Coating Inc. (ECI). The coating is a broadband AR coating that significantly reduces the light reflected in the most critical region of the spectrum, as seen in Figure 48.

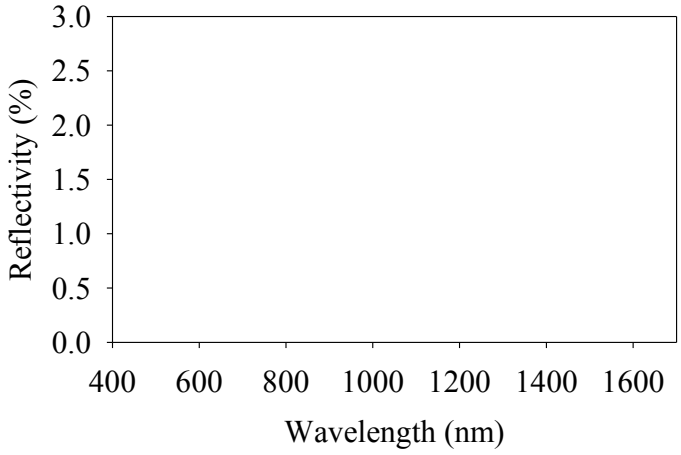

Figure 48. Reflectance of the AR coating selected for our experiment. Data taken from ECI's website[109].

To determine the optimal coating for our system, we compared the reflectance of several coatings to the emission of the xenon arc lamps provided in Figure 47. By multiplying 1-ρ (where ρ is reflectance) by the intensity at each wavelength and integrating the result from 400-1700 nm (the range specified for the coating), the total power transmitted through the window can be obtained. Following this procedure, over the range from 400-1700 nm, the average power transmitted through the coating we selected is 98.63%.

This analysis assumes the absorptance of the coating to be zero in every case. Regardless, the analysis presented here will select the best coating so long as absorptance is constant among the different coatings being considered. Absorptance was not considered because data was not provided for any of the coatings considered. In any case, we expect the absorptance to be low and to therefore have a minimal impact on the performance of the coating.

Flowmeter Design

Because the flowrate of the tin appears in the expression for receiver efficiency, it is crucial to know the mass flowrate as accurately as possible. But making this measurement turned out to be one of the more difficult design challenges in the experiment, because of the extremely low flowrates at which we will be operating and the high molten metal temperature. Knowing the inlet and outlet temperatures of the tin to and from the receiver and the input power from the HFSS, a simple energy balance can be used to show that the mass flowrate of the tin must be approximately 0.022 kg/s. With liquid tin's density of 6950 kg/m^3, this flowrate corresponds to an average linear velocity of approximately 8 cm/s. At such low speeds, a typical magnetic metal flowmeter would not be able to accurately measure the flowrate of the tin. (In any case, the magnets would also likely be heated to well over their Curie temperature and cease to work).

We also avoided a flowmeter design that requires moving parts. Because of the temperatures and conditions at which we are operating, we determined that moving parts were too likely to fail. Flowmeters based on momentum conservation were also ruled out, again because the flowrate of tin was low enough that obtaining an accurate signal would be virtually impossible.

Our solution to these issues was a flowmeter that operates based on Torricelli's law. The flowmeter (shown in Figure 49) is a block of graphite with a large cylinder bored out of it. At the bottom of the block is a small hole through which tin can flow. The higher the flowrate of tin, the higher the steady state height of tin in the flowmeter. An overflow outlet is included as well, so the flowmeter can drain quickly if it gets too full at higher flow rates. By placing the flowmeter on a scale, the amount of tin in the flowmeter

can be determined, which in turn allows us to calculate the tin flowrate. The calculations necessary to do make this determination are described in detail in the following section.

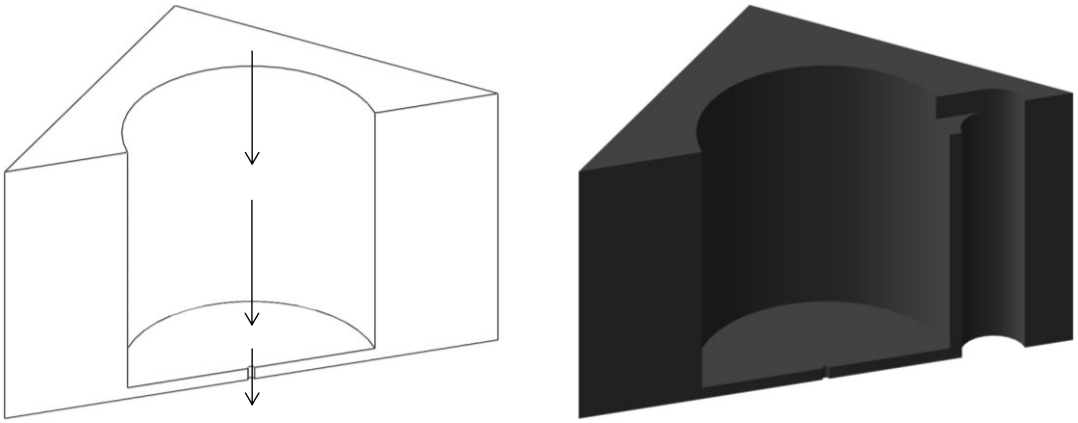

Figure 49. Trimetric cross sectional view with depiction of the flow path of tin through the flowmeter (left) and cross section showing the overflow outlet (right). The large cylindrical cutout is intended to partially fill with tin, while the small cylindrical cutout allows tin to drain from the flowmeter.

Analytical Determination of Flowrate

We initially modeled the flowmeter using Bernoulli's equation and a few simple relations. The derivation relating the mass of tin in the flowmeter to the flowrate is presented here.

Bernoulli's equation, written in terms of pressure head, is given as

$$(h_2 - h_1) + \left(\frac{P_2 - P_1}{\rho g}\right) + \left(\frac{v_2^2 - v_1^2}{2g}\right) = 0 \tag{21}$$

The difference between h_2 and h_1 is the total height of tin in the flowmeter, measured from the bottom of the outlet hole to the top surface of the tin. The two pressures are equal, as both surfaces are free surfaces. Because the cross sectional area at the top surface of the tin is several orders of magnitude larger than the cross sectional area at the outlet, v_2 is negligible. Thus, the equation can be simplified to

$$h = \left(\frac{v_1^2}{2g}\right) \tag{22}$$

where h is the total height of the tin in the flowmeter and v_1 is the velocity of the tin at the outlet. This relation is commonly referred to as Torricelli's law. Outlet velocity can be related to the mass flowrate with knowledge of the density of tin and the cross sectional area of the outlet. Knowing the geometry of the flowmeter, the height of the tin can be related to the total mass of tin in the flowmeter. Using simple substitutions, an expression relating mass and mass flowrate can be obtained:

$$\dot{m} = \frac{r^2}{D}\sqrt{8\pi m\rho g} \tag{23}$$

where $\dot{m}$ is the mass flowrate of the tin, r is the radius of the outlet, D is the diameter of the cylindrical bore, m is the mass of the tin in the flowmeter, and ρ is the density of tin. It should be noted that this expression assumes the bottom of the flowmeter is thin, i.e. the height of tin in the outlet region of the flowmeter is negligible when solving for the flowrate. However, Equation (23) can be easily modified to include the outlet region if the thickness is non-negligible.

To test the validity of Equation (23), which relates the flowrate of tin to the mass of the flowmeter, we solved the equation as a differential equation for m. The solution assumes that the flowmeter starts with some initial mass of liquid, m_0, and once the flowmeter is allowed to drain, no more fluid is added to it. The equation we obtained is

$$m = \frac{1}{4C}\left(-4\sqrt{Cm_0}t + 4Cm_0 + t^2\right) \tag{24}$$

where C is defined as $\frac{D^2}{8\pi\rho r^4 g}$.

Once we derived Equation (24), it was a simple matter to validate it experimentally. We created a flowmeter from a steel cup filled with water and allowed it

to drain. We then compared the data we obtained with the drain curve predicted by Equation (24). The results can be found in Figure 50 below.

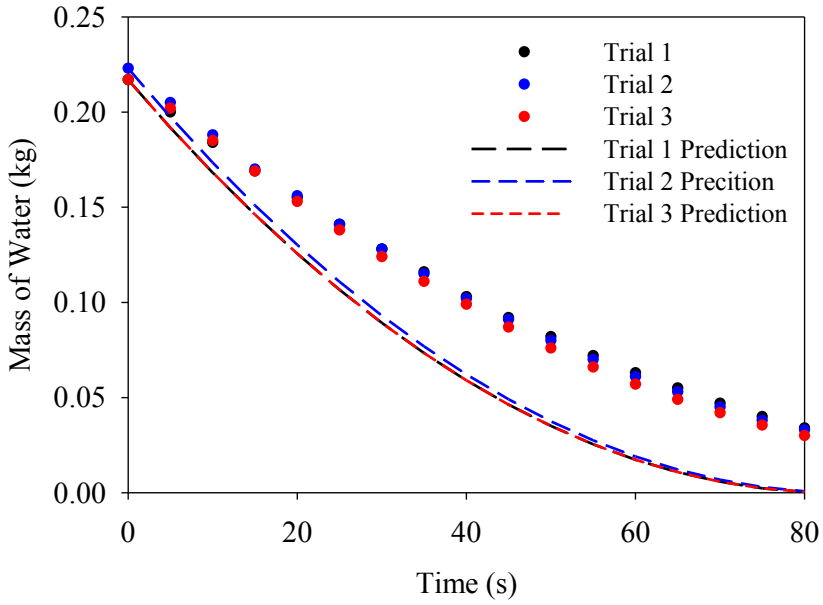

Figure 50. Experimental and predicted drain curves created using water.

It is evident from Figure 50 that the predicted behavior of the drain curve is not in good agreement with the experimental data. For the data presented in Figure 50, the analytically predicted value of C in Equation (24) is 8,050 s^2/kg, while the value obtained from curve fitting is 18,180 s^2/kg. From the Navier-Stokes equation, we can eliminate water's viscosity as an explanation for this discrepancy – the effect due to hydrostatic pressure at the flowmeter outlet is about 20 times as strong as the viscous effects. (See Appendix E for this derivation.) We hypothesize the discrepancy is due to surface tension effects. Due to the diameter of the outlet hole (2.8 mm), the effects of surface tension are expected to be significant and cause water to drain more slowly than expected from the outlet. Furthermore, since tin has a comparable surface tension to density ratio at 300-400°C to water does at 25°C, this effect is not unique to water and cannot be neglected.

Empirical Determination of Flowrate

After some consideration, we developed a simpler, more accurate empirical method using the same flowmeter design, which allows us to ignore any compounding effects such as surface tension or viscosity that may invalidate Bernoulli's law. If fluid flow in the system ceases (i.e. if the pump is turned off), fluid still within the flowmeter will continue to drain. In this case a "drain curve" can be obtained by plotting the mass of fluid within the flowmeter as a function of time. When examining a drain curve, the flowrate at any instant is equal to the slope of the curve at that instant. Thus, an expression relating mass to mass flowrate can easily be derived. By fitting to empirical data to a second order polynomial and taking the derivative of the resultant expression with respect to time, we now have a simple way to relate the mass and the mass flowrate of any given fluid.

We used this method to measure the mass flowrate at steady state with water flowing into the flowmeter. The flowrate was also found by draining the flowmeter into a bucket, and measuring the difference in mass of the buck over a given interval of time. This method afforded us a simple but reliable and accurate method of determining the actual flowrate of the water. Comparing values measured in this manner to those predicted by empirically relating mass to mass flowrate, we found that our method typically underpredicts the flowrate of water by 2-4%.

By switching our mass vs. flowrate relation from an analytically derived expression to one that has been empirically determined, we were able to greatly reduce the error of our measurements. Figure 51 shows the instantaneous flowrate of water measured over the course of 75 seconds using the flowmeter and an empirically

determined relation. Also shown is the average flowrate over the same span of time; this flowrate was determined by measuring the total water that passed through the flowmeter over the course of the measurement, then dividing by 75 seconds.

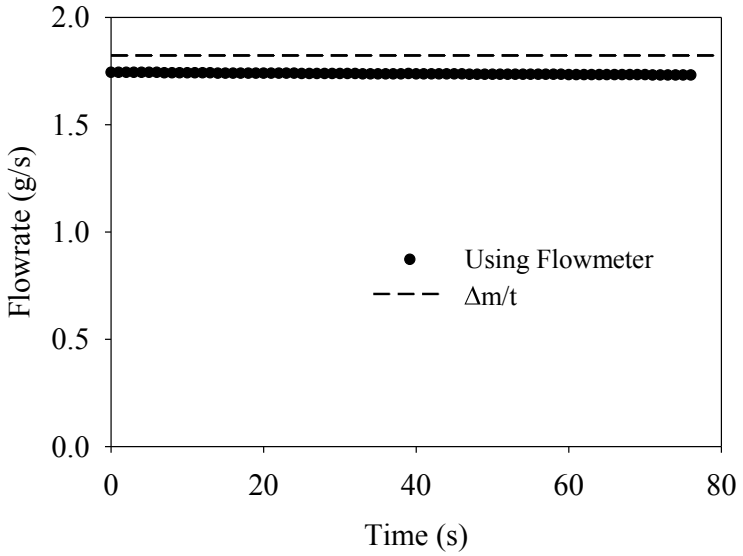

Figure 51. Experimental and predicted drain curves created using water. The dashed line shows the average flowrate determined by dividing the total mass of water that was flowed through the flowmeter by the amount of time it took for that water to flow. The dots show the predicted flowrate at any given instant based on the relation obtained from drain curves.

Comparing the results of these two methods yields an error of 3.4%. While a smaller error would be preferable, given the constraints of our experiment, this method is acceptably accurate.

Pump Characterization

We are using a metal mechanical pump with a ceramic coating to pump tin in our experiment, since the maximum temperature seen by the pump is 400°C. We characterized the pump to determine how precisely our controls allow us to flow tin at low flowrates. For this characterization, we constructed a simple setup, illustrated in Figure 52, in which we pumped tin up a vertical standpipe, which had a horizontal

section at the top to drain the tin into a container placed on a scale. We determined the mass flowrate of tin in the same manner as when we validated the water flowmeter; by measuring the mass at several instances and dividing by the amount of time between measurements, a simple and accurate determination of the mass flowrate could be obtained.

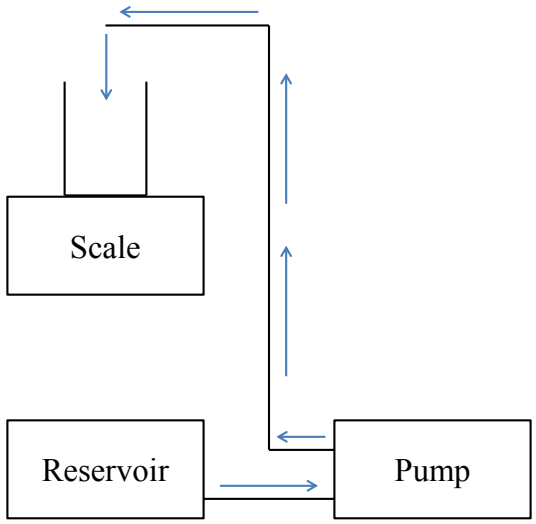

Figure 52. System setup to test pumping capabilities. The direction of flow for the tin is shown with blue arrows.

The raw data was processed to determine a relation between the flowrate and the electrical signal controlling the motor.

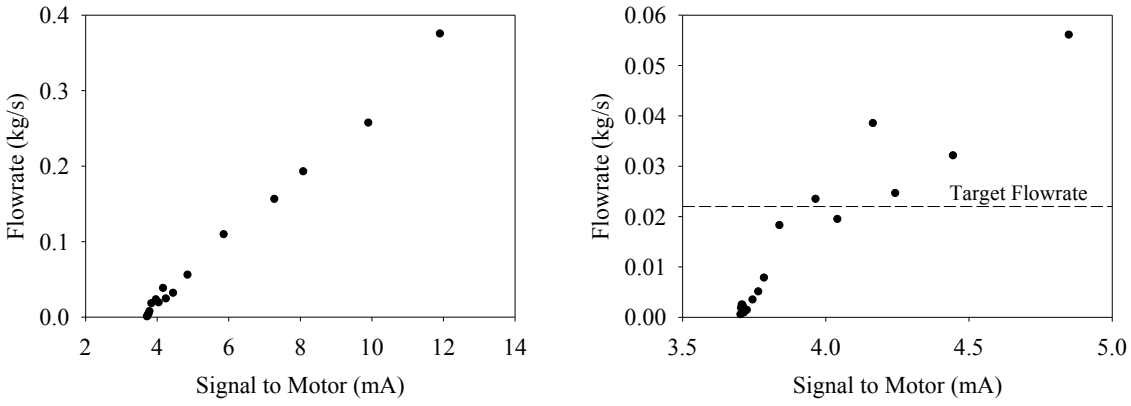

Figure 53. Flowrate vs. signal to motor. The graph on the right is a zoomed-in version of the data in the lower-left portion of the graph on the left.

Figure 53 shows the results obtained from post-processing the data. From the left graph, it is evident that we can pump tin well in excess of our target flowrate (0.022 kg/s); values more than ten times the target flowrate were achieved at the highest motor signal. From the graph on the right, it is apparent that while we have control over the flowrate of our system, the accuracy with which we can flow tin is questionable. However, the thermal mass of the receiver is quite large, so as long as the *average* flowrate is equal to the target flowrate, the flowrate at any given instant can deviate by values of 50% or more. This is because the flowrate through the annular region of the receiver is approximately 1 mm/s. Any deviation in the velocity of the tin over the course of a few seconds will have a minimal impact on the temperature profile of the receiver, so long as the flowrate is adjusted to compensate for this error. Because of the large thermal mass of the receiver and the fact that the dwell time of the tin in the receiver is so large, a deviation in the flow of the tin over the course of a few seconds will have little effect on the temperature of the receiver.

Graphite Reaction Bonding Procedure

Over the course of several months, we refined our procedure for gluing graphite components together. This refinement was necessary for two reasons. Firstly, in some cases, too much glue would be used, resulting in blockages forming. Secondly, in other cases the glue would not form a bond of sufficiently high quality, and the joint formed would leak. To address the issue of a blockage, we developed a method to create "plugs" of tin that would prevent glue from filling the cross section of the graphite pipes. More details about tin plugs can be found in Wilk's thesis[50].

To ensure we can form bonds that do not leak, we have modified the process for gluing joints. The glue used is Cotronics 931 Graphite Adhesive, which consists of two components: a black powder and a liquid binding agent. While the suggested mixing ratio is 100:35 powder to binder by weight, we have reduced this ratio slightly, in an attempt to compensate for the high humidity of the air in our lab. We also ensure that the surfaces to be glued are roughened, because of the manner in which the glue bonds to graphite. By roughening the surface, the total surface area to which the glue may adhere is increased substantially. Furthermore, doing so creates features on the surface of the graphite, such as grooves and ridges, to which the glue will more easily adhere.

When gluing components, we have determined that a gap between graphite parts of approximately 0.5 mm is optimal. This gap is sized so the glue does not have to span such a large distance that it forms voids, but there exists enough of a gap that the glue is not simply forced out of the gap, because the two components being glued are in direct contact with no room between them for the glue.

Repairing Leaking Joints

Despite the detailed procedure we follow when bonding graphite parts together, components do occasionally leak. To patch leaks, we developed a straightforward procedure to repair any areas where glue is not dense enough to stop the flow of tin. The glue around the leak is first removed with a dental pick, leaving a small groove to be filled with glue. We then add more glue to the area where the original glue was picked away. When picking away the glue, we make the groove as deep as our tools allow, plugging as much of the leak path as possible and in turn minimizing the chance of the leak re-forming.

Packing Insulation

Much of the insulation in our system is zirconia and/or alumina fiber, which has a consistency similar to unwoven cotton. While we initially assumed that leaving the insulation uncompressed would lead to the lowest possible thermal conductivity, this is not in fact the case. Data provided by Zircar Zirconia[95] indicates that compressing the insulation actually decreases its thermal conductivity. This effect is particularly pronounced at elevated temperatures.

It is our understanding that the reason for this decrease in thermal conductivity is due to the reduction in the size of gas pockets. The Rayleigh number of gas in a pocket decreases with the third power of pocket size, so convective transport of heat through the insulation is greatly reduced.

When preparing components of the system, we pack the insulation so its density is 2-4 x that of unpacked insulation. Doing so ensures that the thermal conductivity is reduced, particularly at higher temperatures where thermal losses are largest. When wrapping pipes in insulation, our procedure is as follows. We first wrap the length of the pipe with heat tape, making sure the electrical leads are sufficiently far from the heat tape so as to ensure they do not overheat and fail. Next, we affix thermocouples to the pipe to allow us to monitor the pipe's temperature. We then take a sheet of insulation and wrap it around the pipe, compressing the insulation as we do so. Finally, we take a long braided piece of fiberglass and wrap it around the insulation to hold everything in place. The ends of the pipe, as well as the electrical and thermocouple leads, protrude from the insulation, so that the heat tape and thermocouples can be plugged in and the pipe glued to other components in the system.

Nitrogen Containment System

As mentioned previously, we must conduct our experiment in an inert environment. For simplicity, we selected nitrogen as the inert gas to use in our system. We then constructed a large steel box to house our experiment in a nitrogen environment. The box footprint is 4x4 ft and the height is 5 ft. The exterior of the box consists of evenly-spaced steel ribs, with a sheet of steel lining the inside of these ribs. The ribs provide structural support, while the steel sheet allows us to form a hermetic seal. At the edges of the box, we used a combination of vacuum grease and silicone-based RTV-blue gasket maker. One "wall" of the box is actually a door to the box as well, which is sealed using a similar strategy. We added several pull-action toggle clamps to the door, and both the door and the door frame were lined with a rubber strip coated in vacuum grease. Pictures of these various sealing methods are included in Figure 54 below.

Figure 54. Various methods used to seal the nitrogen containment box: RTV coating on the edge of the box (left). RTV coating around the window frame (center). Toggle clamp to seal the door, with a vacuum grease coated, orange rubber strip visible (right).

To pass wires, such as those used for power cords and thermocouples, through the steel walls, we installed cord grips and sealed the cord grips using RTV. A similar strategy was employed to transport fluids such as nitrogen and cooling oil across the boundary. Both these methods can be seen in Figure 55 below.

Figure 55. Methods for bringing cords and pipes across the nitrogen barrier without compromising the seal. RTV is used extensively to ensure the seal is hermetic.

When we remove oxygen from the box we are able to achieve partial oxygen pressures $P_{O_2} < 10^{-18}$ atm. Given the dimensions of the box and the partial pressure, this corresponds to a total of approximately 5 x 10^7 atoms of oxygen in the nitrogen box. The P_{O_2} is so low that it prevents any significant oxidation of the components in the system, which can be seen by considering the limiting case in which all of the O_2 in the box oxidizes a single portion of one component. With so few atoms, available, 5 x 10^7 atoms corresponds to about 10^{-14} g of tin or about 10^{-15} g of graphite oxidizing. Thus, suppressing the P_{O_2} below 10^{-18} atm ensures that the system integrity will be maintained throughout the experiment.

Purging Oxygen from the Nitrogen Containment Box

While we designed the nitrogen containment box to keep the P_{O_2} at extremely low values, we still needed to devise a method to displace existing oxygen in the box with nitrogen. We accomplish this reduction in P_{O_2} in two steps. In the first step, we pump pure nitrogen into the box, while opening a small conduit for gas to escape. In this manner, we slowly replace oxygen in the box with nitrogen. This procedure reduces the P_{O_2} to approximately 10^{-4} atm over the course of a few hours. However, past this point, adding more nitrogen does very little to reduce P_{O_2}. The procedure described here causes the P_{O_2} to drop asymptotically, and the rate of reduction in P_{O_2} at 10^{-4} atm is so low as to be essentially negligible. At this point, we employ the second stage of our strategy, and use a tin getter, shown in Figure 56, to consume the remaining oxygen in the box. The getter is a simple device, consisting of a crucible of solid tin with a stir rod protruding from it that is in turn attached to a motor. Once the P_{O_2} reaches 10^{-4} atm, we melt the tin in the crucible and activate the stir rod. The getter tin is quickly oxidized (see Figure 57), which causes the P_{O_2} to drop to about 10^{-18} atm.

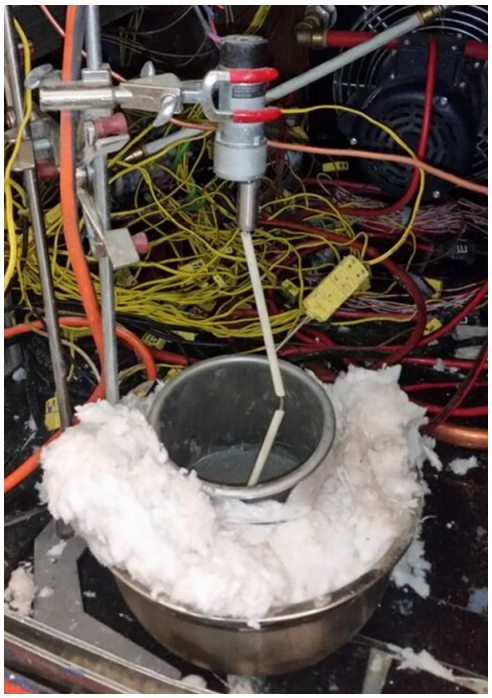

Figure 56. Picture of the getter. Insulation around the crucible is visible, as is the crucible itself, the stir rod, and the motor. Oxidized tin can be seen inside the crucible.

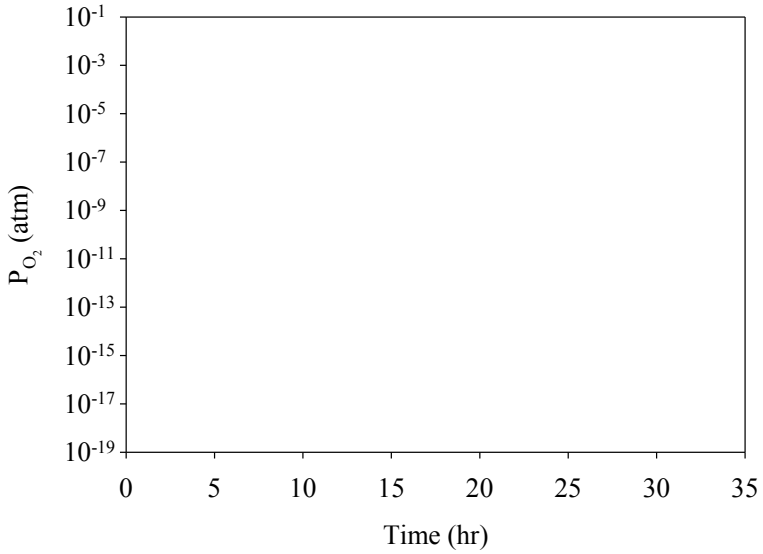

Figure 57. P_{O_2} in the nitrogen containment box during a purge, in which nitrogen is continually being flowed into the box to remove oxygen. At ~10^{-4} atm, the getter is turned on, and the result is the P_{O_2} in the box dropping precipitously.

Scale Drift

Our initial design of the flowmeter assembly placed the scale in much closer proximity to the graphite flowmeter. Because of this close proximity, the temperature of the scale increased substantially above the ambient temperature of 25°C. When this increase happened, we observed that, holding everything else constant, the weight measured by the scale decreased, indicating that the scale's reading was affected by temperature. This tendency was replicated several times, which resulted in redesigning the flowmeter to locate the scale far from anything that would be heated above ambient temperatures.

Control System

To monitor and record all the data in our experiment and to control active components of the experiment such as the pump and heat tapes, we created a control system using National Instrument's software LabVIEW. The specific capabilities of this system are described here.

Thermocouple Readings

The largest portion by far of the control system is its ability to convert thermocouple voltages to a temperature reading. Because our experiment is sealed within a box, it is difficult to visually monitor what is happening. However, we have dozens of thermocouples affixed to various components to monitor temperatures. The thermocouples we are using are primarily K-type, with a maximum service temperature of 1,260°C. However, if the thermocouples are not hermetically sealed, their maximum use temperature is around 800°C, because they will otherwise experience "green rot" in a

nitrogen atmosphere[110]. To measure temperatures in excess of 1,260°C, we used B-type thermocouples.

Thermostat Controllers

To preheat our system, we use both heat tapes and heating coils. To ensure these heaters do no overheat the system, we created thermostats within LabVIEW. These thermostats are very simple to operate, and each individual thermostat controls either a single or a group of heat tapes or heating coils. Each thermostat is controlled by a specific thermocouple. If the temperature reading of that thermocouple is below the setpoint specified by the user, power will be supplied to the heat tape(s)/heating coil(s) until the temperature exceeds that of the setpoint.

Miscellaneous Capabilities

We added several other capabilities to the control system, which allow us to collect data and control various aspects of the experiment. The control system is designed to record every piece of data to a string, which is outputted to a text file along with a timestamp. As described in "Flowmeter Design" earlier in this appendix, a weight measurement must be recorded to determine a flowrate for the tin. We have configured our system to work with two different scales, the Ohaus Ranger 3000- R31P15, and the Detecto APS10, both of which have a resolution of 0.5 g and a maximum weight capacity of 15 kg. The control system is also used to control the pump motor, by sending a 4-20 mA signal to a variable speed drive, which in turn communicates with the motor. We also configured the control system to read a conditioned signal from a pulse flowmeter, though we did not use this capability at any point.

APPENDIX E: APPROXIMATION OF VISCOUS EFFECTS IN THE WATER-BASED FLOWMETER

Near the outlet of the flowmeter, fluid flow is expected to be rotationally symmetric, and the flowmeter operates at steady state, so terms with a θ dependency or a time dependency are equal to zero. The Navier-Stokes can then be written in cylindrical coordinates for fluid flowing in the *z*-direction as

$$\rho\left(u_r\frac{\partial u_z}{\partial r}+u_z\frac{\partial u_z}{\partial z}\right)=-\frac{\partial P}{\partial z}+\mu\left[\frac{1}{r}\frac{\partial}{\partial r}\left(r\frac{\partial u_z}{\partial r}\right)+\frac{\partial^2 u_z}{\partial z^2}\right]+\rho g_z \tag{25}$$

where ρ is the fluid density, u_r is the fluid velocity in the *r*-direction, u_z is the fluid velocity in the *z*-direction, P is the pressure of the fluid, μ is the dynamic viscosity of the fluid, and g_z is the force of gravity in the *z*-direction. Examining this equation, u_r is approximately zero at the outlet. Similarly, $\frac{\partial u_z}{\partial z}$ (and consequently, $\frac{\partial^2 u_z}{\partial z^2}$) is approximately zero, because mass continuity must hold within the exit region of the fluid. Thus, the resultant equation is

$$\frac{\partial P}{\partial z}=\mu\frac{1}{r}\frac{\partial}{\partial r}\left(r\frac{\partial u_z}{\partial r}\right)+\rho g_z \tag{26}$$

and the two terms that affect the change in pressure (and therefore the flow of the fluid through the outlet) are $\mu\frac{1}{r}\frac{\partial}{\partial r}\left(r\frac{\partial u_z}{\partial r}\right)$ and ρg_z. As a simple approximation, the fluid can be assumed to flow through the outlet with the same velocity profile as through a pipe: $u_z(r)\approx v_0\left[1-\left(\frac{r}{r_0}\right)^2\right]$ where v_0 is twice the average velocity of fluid flowing through the flowmeter outlet. Using this approximation, the first term on the right hand side of Equation (26) can be simplified to $\frac{-4\mu v_0}{{r_0}^2}$. Typical values in the case of the water

flowmeter described in this thesis are μ=9x10^{-4} Pa-s, v_0=0.3 m/s, and r_0=1.5 mm. Evaluating, $\frac{-4\mu v_0}{{r_0}^2}$≈500 Pa/m, while ρg_z≈10,000 Pa/m. Thus the hydrostatic pressure term dominates the viscous term.

APPENDIX F: DESIGN OF A WATER-BASED CALORIMETER

While much attention has been given to the receiver and the auxiliary components designed to allow for testing the receiver, we also designed a calorimeter intended to characterize the HFSS. While the calorimeter has not been tested, a large amount of work has gone into its design, and it was fabricated for testing.

We created a calorimeter for two purposes. Most importantly, it was intended to be used to determine the total power of the light emitted by the HFSS. The second purpose was validating simulations we had performed in COMSOL. To this end, we designed the calorimeter as a cavity "receiver" made of aluminum that uses water as the working fluid. The design of the receiver is virtually identical to the graphite "cup" receiver design (see Figure 58). Water is flowed at a sufficiently high flowrate that we do not risk it boiling.

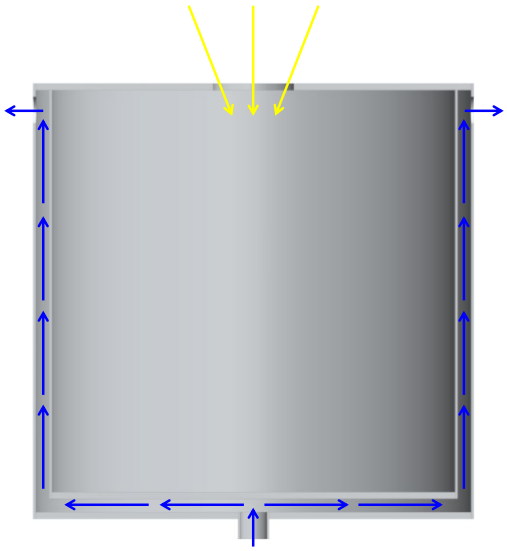

Figure 58. Calorimeter schematic. Direction of water flow is shown with blue arrows, and light entering the receiver is shown with yellow arrows.

Here, the aperture of the calorimeter is much larger than that of the graphite receiver (5 cm vs. 2.35 cm). We elected to make the aperture so large because we wanted to determine the total amount of energy emitted by the HFSS. This amount includes any spillage that would strike the area around the aperture of the graphite receiver. We determined that if desired, we could also put a plate with a smaller hole in it over the aperture to effectively reduce the size of the aperture. Because the cavity of the receiver must remain below 100°C to avoid boiling water anyway, reradiation is not a concern; at such temperatures, its effect is completely negligible. We painted the inside of the cavity black as well, to minimize reflection losses.

While the total radiant energy entering the cavity can be determined with relative ease, we devised several additional experiments that would allow us validate many of our simulations. We determined the best means to accomplish this validation would be to place thermocouples at several locations along the receiver. By moving the receiver towards or away from the HFSS, we could effectively change how light from the HFSS is distributed in the receiver cavity, leading to a difference in local temperature readings. We ran several simulations, with the receiver located in different positions relative to the focal point of the HFSS. By selecting specific points on the calorimeter and plotting the temperature at that point versus the location of the calorimeter with respect to the HFSS, trends emerge in the temperature distribution. The difference in predicted temperature profile can be seen in Figure 59 below.

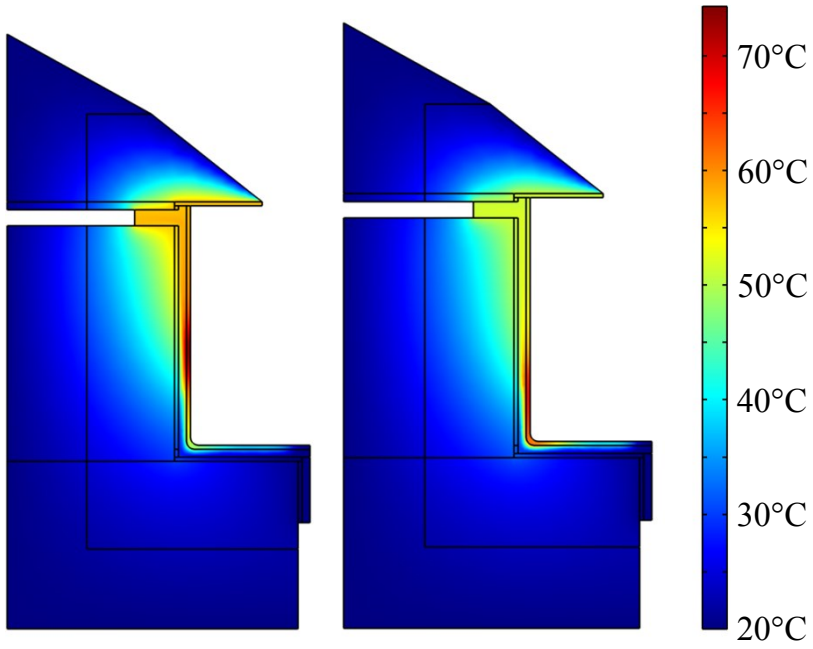

Figure 59. Temperature cross section of one-half of the calorimeter. The temperature map on the left is the predicted temperature distribution when the aperture is located at the focal plan. The profile on the right is the prediction when the aperture is located 5 cm towards the HFSS from the focal plane.

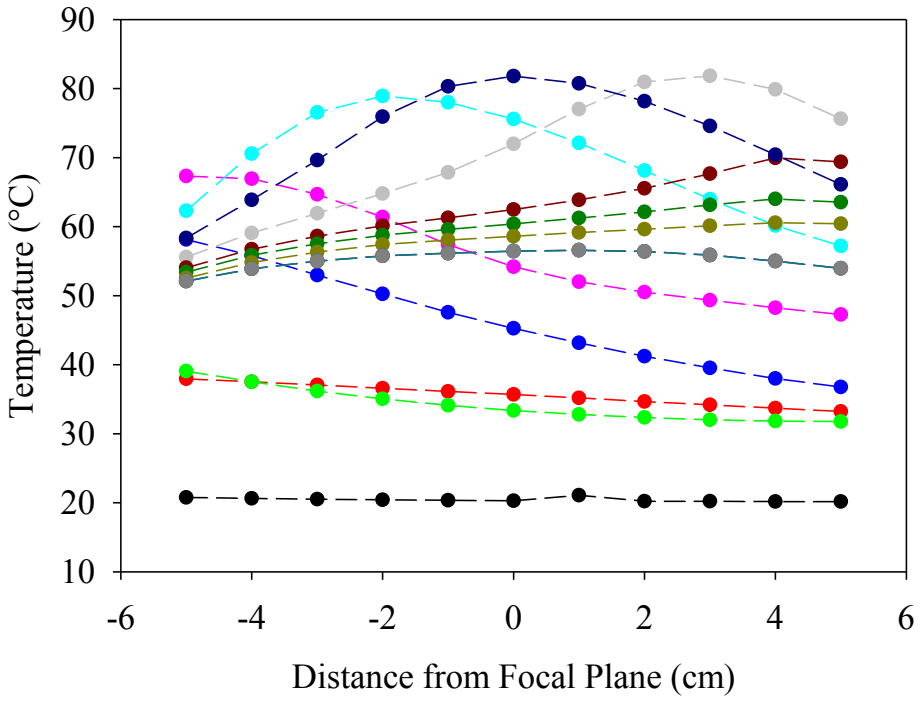

Figure 60. Predicted temperature of various locations on the calorimeter as a function of calorimeter position with respect to the focal plane.

It can be seen in Figure 60 that some very clear, predictable trends emerge in the temperature distribution of the calorimeter. For instance, the hottest portion of the receiver (represented by the light blue, dark blue, and gray curves) can be seen to have a distinct maximum temperature that is dependent on the location of the calorimeter. Based on how closely the results align with these predictions, we can determine the degree of accuracy of our simulations.

We built the calorimeter, to the point that it was ready to be tested using the HFSS. To create the cavity of our calorimeter, we used two aluminum pots in a configuration similar to that used with the two pieces of the graphite receiver. We affixed waterproof thermocouples to the outer surface of the inner pot using JB Weld SteelStik, as shown in Figure 61. A small hole was cut in the large pot so the leads of the thermocouples could be attached to a DAQ. At the exit port for the thermocouple wires, the wires passed through a 90° brass elbow, which was filled with RTV silicone blue to prevent water from leaking through the port. A lid was fabricated for the two pots from a thick piece of aluminum. The pots were each screwed to the lid, which held the two pots in place with respect to each other. Four holes were cut in the lid as outlets for the water, and a hole was cut in the base of the larger pot to serve as an inlet for the water. The inside of the smaller pot was also painted with a high temperature black paint, which increased its effective absorptivity. Additional silicon blue was used to seal all connections to ensure the assembly was watertight. The assembled calorimeter can be seen in Figure 62.

Figure 61. Aluminum pot used as the inner surface of the calorimeter with thermocouples attached. The pot is connected to the lid, and two of the outlets in the lid can be seen at the bottom of the picture.

Figure 62. Completed assembly of the calorimeter. The connections on the four outlets can be seen on the right side of the image, as well as part of the piping that recombines the outlet flow back into a single stream. The aperture is also visible on the right.

Unfortunately, when we attempted to test the calorimeter, the water pressure within the calorimeter became too high, causing the entire assembly to fail catastrophically (see Figure 63). Due to the length of time it took to construct the calorimeter, we determined it would be better not to reconstruct the calorimeter. This decision was also because Dr. Loutzenheiser's group has characterized the HFSS, and we have validated our simulations, as detailed in Chapter 5.

Figure 63. Image of two points of failure of the calorimeter. The two screws shown were screwed through the outer pot and into the calorimeter lid. In the image on the left, the screw can be seen to have sheared completely, while on the right, the aluminum around the screw hole failed.

REFERENCES

1. Pachauri, R.K., et al., *Climate Change 2014: Synthesis Report. Contribution of Working Groups I, II and III to the Fifth Assessment Report of the Intergovernmental Panel on Climate Change.* 2014.

2. Pitz-Paal, R., et al. *Development Steps for Concentrating Solar Power Technologies With Maximum Impact on Cost Reduction: Results of the European ECOSTAR Study*. in *ASME 2005 International Solar Energy Conference*. 2005. American Society of Mechanical Engineers.

3. *http://www.mistbreaker.com/sustainability/possible-power-solar-tower/*.

4. Breyer, C. and A. Gerlach, *Global overview on grid-parity.* Progress in photovoltaics: Research and Applications, 2013. **21**(1): p. 121-136.

5. Jean, J., et al., *Pathways for solar photovoltaics.* Energy & Environmental Science, 2015. **8**(4): p. 1200-1219.

6. Carnegie, R., et al., *Utility scale energy storage systems.* 2013.

7. Kolb, G.J., et al., *Power tower technology roadmap and cost reduction plan.* SAND2011-2419, Sandia National Laboratories, Albuquerque, NM, 2011: p. 7.

8. Lin, C.-H., et al., *Optimization of photovoltaic penetration in distribution systems considering annual duration curve of solar irradiation.* Power Systems, IEEE Transactions on, 2012. **27**(2): p. 1090-1097.

9. Tonkoski, R. and L.A. Lopes, *Impact of active power curtailment on overvoltage prevention and energy production of PV inverters connected to low voltage residential feeders.* Renewable Energy, 2011. **36**(12): p. 3566-3574.

10. Denholm, P. and M. Mehos, *Enabling greater penetration of solar power via the use of CSP with thermal energy storage.* Solar Energy: Application, Economics, and Public Perception, 2014: p. 99.

11. l'énergie, A.i.d., *Energy technology perspectives 2012: Pathways to a clean energy system*. 2012: OECD/IEA.

12. IEA, *Energy Technology Perspectives 2015*. 2015: OECD Publishing.

13. Wilcox, S. and C. Gueymard, *Spatial and temporal variability of the solar resource in the United States.* Washington, DC: NREL/DoE [National Renewable Energy Laboratory/Department of Energy], 2010.

14. Pacheco, J., et al., *Summary of the Solar Two: Test and Evaluation Program. 2000.* SANDIA Labs: Alburquerque, 2000.

15. Behar, O., A. Khellaf, and K. Mohammedi, *A review of studies on central receiver solar thermal power plants.* Renewable and Sustainable Energy Reviews, 2013. **23**: p. 12-39.

16. Margolis, R., C. Coggeshall, and J. Zuboy, *SunShot vision study.* US Dept. of Energy, 2012.

17. Müller-Steinhagen, H. and F. Trieb, *Concentrating solar power.* A review of the technology. Ingenia Inform QR Acad Eng, 2004. **18**: p. 43-50.

18. Pacheco, J.E., C. Moursund, and D.W. Dale Rogers, *Conceptual design of a 100 MWe modular molten salt power tower plant*. 2011, eSolar, Inc., Burbank, CA.

19. Zhang, H., et al., *Concentrated solar power plants: Review and design methodology.* Renewable and Sustainable Energy Reviews, 2013. **22**: p. 466-481.

20. Kaushik, S., V.S. Reddy, and S. Tyagi, *Energy and exergy analyses of thermal power plants: A review.* Renewable and Sustainable Energy Reviews, 2011. **15**(4): p. 1857-1872.

21. Khaliq, A. and S. Kaushik, *Second-law based thermodynamic analysis of Brayton/Rankine combined power cycle with reheat.* Applied Energy, 2004. **78**(2): p. 179-197.

22. Rolf, B., N. Henrik, and W. Judy, *Combined-cycle Gas and Steam Turbine Power Plants.* 1999.

23. Bradshaw, R. and D. Meeker, *High-temperature stability of ternary nitrate molten salts for solar thermal energy systems.* Solar energy materials, 1990. **21**(1): p. 51-60.

24. Bradshaw, R.W. and N.P. Siegel. *Molten nitrate salt development for thermal energy storage in parabolic trough solar power systems*. in *ASME 2008 2nd International Conference on Energy Sustainability collocated with the Heat Transfer, Fluids Engineering, and 3rd Energy Nanotechnology Conferences*. 2008. American Society of Mechanical Engineers.

25. Dunn, R., P.J. Hearps, and M.N. Wright, *Molten-salt power towers: newly commercial concentrating solar storage.* Proceedings of the IEEE, 2012. **100**(2): p. 504-515.

26. Raade, J.W. and D. Padowitz, *Development of molten salt heat transfer fluid with low melting point and high thermal stability.* Journal of Solar Energy Engineering, 2011. **133**(3): p. 031013.

27. DeVan, J. and R. Evans III, *Corrosion Behavior of Reactor Materials in Fluoride Salt Mixtures.* ORNL/TM-328, Oak Ridge National Laboratory, Oak Ridge, TN, 1962.

28. Misra, A.K. and J.D. Whittenberger, *Fluoride salts and container materials for thermal energy storage applications in the temperature range 973 to 1400 K*. 1987, National Aeronautics and Space Administration, Cleveland, OH (USA). Lewis Research Center.

29. Olson, L.C., et al., *Materials corrosion in molten LiF–NaF–KF salt.* Journal of Fluorine Chemistry, 2009. **130**(1): p. 67-73.

30. Williams, D., L. Toth, and K. Clarno, *Assessment of candidate molten salt coolants for the advanced high temperature reactor (AHTR)*. 2006: United States. Department of Energy.

31. Li, C.-J., et al., *Survey of Properties of Key Single and Mixture Halide Salts for Potential Application as High Temperature Heat Transfer Fluids for Concentrated Solar Thermal Power Systems.* AIMS Energy, 2014. **2**(2): p. 133-157.

32. Sanz-Bermejo, J., J. Gonzalez-Aguilar, and M. Romero. *Performance Analysis of Direct Steam Generation-Central Receiver Systems*. in *ASME Turbo Expo 2012: Turbine Technical Conference and Exposition*. 2012. American Society of Mechanical Engineers.

33. Bugge, J., S. Kjær, and R. Blum, *High-efficiency coal-fired power plants development and perspectives.* Energy, 2006. **31**(10): p. 1437-1445.

34. Ho, C.K. and B.D. Iverson, *Review of high-temperature central receiver designs for concentrating solar power.* Renewable and Sustainable Energy Reviews, 2014. **29**: p. 835-846.

35. Weitzel, P.S. *Steam Generator for Advanced Ultra Supercritical Power Plants 700C to 760C*. in *ASME 2011 Power Conference collocated with JSME ICOPE 2011*. 2011. American Society of Mechanical Engineers.

36. Wright, I., et al., *Materials issues for turbines for operation in ultra-supercritical steam.* Research sponsored by the US Department of Energy, Office of Fossil Energy, Advanced Research Materials Program, under Contract DE-AC05-00OR22725 with UT-Battelle, LLC, 2004.

37. Becker, M., et al., *Theoretical and numerical investigation of flow stability in porous materials applied as volumetric solar receivers.* Solar energy, 2006. **80**(10): p. 1241-1248.

38. Ries, H. and W. Spirkl, *Inherent limitations of volumetric solar receivers.* Journal of Solar Energy Engineering, 1996. **118**: p. 151.

39. Garcia-Casals, X. and J.I. Ajona, *The duct selective volumetric receiver: potential for different selectivity strategies and stability issues.* Solar energy, 1999. **67**(4): p. 265-286.

40. Kribus, A., et al., *A multistage solar receiver:: The route to high temperature.* Solar Energy, 1999. **67**(1): p. 3-11.

41. Pitz-Paal, R., et al., *Experimental and numerical evaluation of the performance and flow stability of different types of open volumetric absorbers under non-homogeneous irradiation.* Solar Energy, 1997. **60**(3): p. 135-150.

42. Karni, J., et al., *The DIAPR: a high-pressure, high-temperature solar receiver.* Journal of solar energy engineering, 1997. **119**(1): p. 74-78.

43. Ries, H., A. Segal, and J. Karni, *Extracting concentrated guided light.* Applied optics, 1997. **36**(13): p. 2869-2874.

44. Karni, J., et al., *The "porcupine": a novel high-flux absorber for volumetric solar receivers.* Journal of solar energy engineering, 1998. **120**(2): p. 85-95.

45. Hischier, I., et al., *Heat transfer analysis of a novel pressurized air receiver for concentrated solar power via combined cycles.* Journal of Thermal Science and Engineering Applications, 2009. **1**(4): p. 041002.

46. Siegel, N.P., et al., *Development and evaluation of a prototype solid particle receiver: on-sun testing and model validation.* Journal of Solar Energy Engineering, 2010. **132**(2): p. 021008.

47. Bertocchi, R., J. Karni, and A. Kribus, *Experimental evaluation of a non-isothermal high temperature solar particle receiver.* Energy, 2004. **29**(5): p. 687-700.

48. Bertocchi, R., *Carbon particle cloud generation for a solar particle receiver.* Journal of solar energy engineering, 2002. **124**(3): p. 230-236.

49. Yang, Z. and S.V. Garimella, *Thermal analysis of solar thermal energy storage in a molten-salt thermocline.* Solar energy, 2010. **84**(6): p. 974-985.

50. Wilk, G., *Economic and Experimental Investigation of Molten Metal Concentrated Solar Power*, in *Mechanical Engeineering*. 2015, Georgia Institute of Technology.

51. Boerema, N., et al., *Liquid sodium versus Hitec as a heat transfer fluid in solar thermal central receiver systems.* Solar Energy, 2012. **86**(9): p. 2293-2305.

52. Schiel, W.J. and M.A. Geyer, *Testing an external sodium receiver up to heat fluxes of 2.5 MW/m 2: Results and conclusions from the IEA-SSPS high flux experiment conducted at the central receiver system of the Plataforma Solar de Almeria (Spain).* Solar energy, 1988. **41**(3): p. 255-265.

53. Hasnain, S., *Review on sustainable thermal energy storage technologies, Part II: cool thermal storage.* Energy conversion and management, 1998. **39**(11): p. 1139-1153.

54. Pacio, J. and T. Wetzel, *Assessment of liquid metal technology status and research paths for their use as efficient heat transfer fluids in solar central receiver systems.* Solar Energy, 2013. **93**: p. 11-22.

55. Brasunas, A.D.S., *Liquid metal corrosion.* Corrosion, 1953. **9**(3): p. 78-84.

56. Chopra, O.K., et al., *Liquid-metal corrosion.* Fusion Science and Technology, 1985. **8**(2P1): p. 1956-1969.

57. DiStefano, J. and E. Hoffman, *Corrosion mechanisms in refractory metal-alkali metal systems*. 1963, Oak Ridge National Lab., Tenn.

58. Liu, X., et al., *Liquid metal corrosion of 316L, Fe3Al, and FeCrSi in molten Zn-Al baths.* Metallurgical and Materials Transactions A, 2005. **36**(8): p. 2049-2058.

59. Lynch, S. and P. Trevena, *Stress corrosion cracking and liquid metal embrittlement in pure magnesium.* Corrosion, 1988. **44**(2): p. 113-124.

60. Manly, W., *Fundamentals of Liquid Metal Corrosion ★*. Corrosion, 1956. **12**(7): p. 46-52.

61. Zhang, J., P. Hosemann, and S. Maloy, *Models of liquid metal corrosion.* Journal of Nuclear Materials, 2010. **404**(1): p. 82-96.

62. Singer, C., et al., *Assessment of solar power tower driven ultrasupercritical steam cycles applying tubular central receivers with varied heat transfer media.* Journal of solar energy engineering, 2010. **132**(4): p. 041010.

63. *http://www.solarreserve.com/en/technology/molten-salt-tower-receiver*.

64. Fang, J., N. Tu, and J. Wei, *Numerical investigation of start-up performance of a solar cavity receiver.* Renewable Energy, 2013. **53**: p. 35-42.

65. Fang, J.-B., et al., *Thermal performance simulation of a solar cavity receiver under windy conditions.* Solar Energy, 2011. **85**(1): p. 126-138.

66. Harris, J.A. and T.G. Lenz, *Thermal performance of solar concentrator/cavity receiver systems.* Solar energy, 1985. **34**(2): p. 135-142.

67. Yu, Q., Z. Wang, and E. Xu, *Simulation and analysis of the central cavity receiver's performance of solar thermal power tower plant.* Solar Energy, 2012. **86**(1): p. 164-174.

68. Li, X., et al., *Thermal model and thermodynamic performance of molten salt cavity receiver.* Renewable Energy, 2010. **35**(5): p. 981-988.

69. Zhang, Q., et al., *An experimental study: Thermal performance of molten salt cavity receivers.* Applied Thermal Engineering, 2013. **50**(1): p. 334-341.

70. Falcone, P.K., *A handbook for solar central receiver design*. 1986, Sandia National Labs., Livermore, CA (USA).

71. Garcia, P., A. Ferriere, and J.-J. Bezian, *Codes for solar flux calculation dedicated to central receiver system applications: a comparative review.* Solar Energy, 2008. **82**(3): p. 189-197.

72. Gauché, P., T.W. von Backström, and A.C. Brent, *CSP Modeling Methodology for Macro Decision Making-Emphasis on the Central Receiver Type.*

73. Steinfeld, A., *Solar hydrogen production via a two-step water-splitting thermochemical cycle based on Zn/ZnO redox reactions.* International Journal of Hydrogen Energy, 2002. **27**(6): p. 611-619.

74. Krueger, K.R., *Design and characterization of a concentrating solar simulator*. 2012, UNIVERSITY OF MINNESOTA.

75. Bird, R.E., *A simple, solar spectral model for direct-normal and diffuse horizontal irradiance.* Solar energy, 1984. **32**(4): p. 461-471.

76. *http://me.umn.edu/labs/solar/facilities/hfss.shtml*.

77. *http://www.metalprices.com/metal/tin/lme-tin-cash-official*.

78. Kearney, D., *Overview on use of a Molten Salt HTF in a Trough Solar Field*. 2003: National Renewable Energy Laboratory.

79. Boggs, W.E., *The Oxidation of Tin III. The Mechanisms of Oxidation of Pure Tin and Their Dependence on Time and Oxygen Pressure.* Journal of The Electrochemical Society, 1961. **108**(2): p. 124-129.

80. Cho, S., et al., *Oxidation study of pure tin and its alloys via electrochemical reduction analysis.* Journal of electronic materials, 2005. **34**(5): p. 635-642.

81. Grigoriev, A., et al., *Surface oxidation of liquid Sn.* Surface science, 2005. **575**(3): p. 223-232.

82. Xiaowei, L., R. Jean-Charles, and Y. Suyuan, *Effect of temperature on graphite oxidation behavior.* Nuclear Engineering and design, 2004. **227**(3): p. 273-280.

83. *http://cronkitenewsonline.com/2012/03/one-year-after-fukushima-aps-says-palo-verde-is-safe/*.

84. Rose, A., *Calculation of critical stress intensity factors of nuclear graphite from small specimen tests.* Carbon, 1985. **23**(4): p. 387-393.

85. Hove, J.E., *Graphite as a High Temperature Material.* Trans. AIME, 1958. **212**: p. 7.

86. Eto, M., T. Arai, and T. Konishi, *The fatigue strength of graphite and carbon materials for HTTR core components*. 1998, Japan Atomic Energy Research Inst., Tokyo (Japan).

87. de Vahl Davis, G., *Laminar natural convection in an enclosed rectangular cavity.* International Journal of Heat and Mass Transfer, 1968. **11**(11): p. 1675-1693.

88. Markatos, N.C. and K. Pericleous, *Laminar and turbulent natural convection in an enclosed cavity.* International Journal of Heat and Mass Transfer, 1984. **27**(5): p. 755-772.

89. Cormack, D., L. Leal, and J. Imberger, *Natural convection in a shallow cavity with differentially heated end walls. Part 1. Asymptotic theory.* Journal of fluid Mechanics, 1974. **65**(02): p. 209-229.

90. Patterson, J. and J. Imberger, *Unsteady natural convection in a rectangular cavity.* Journal of Fluid Mechanics, 1980. **100**(01): p. 65-86.

91. Autio, G.W. and E. Scala, *The normal spectral emissivity of isotropic and anisotropic materials.* Carbon, 1966. **4**(1): p. 13-28.

92. Balloy, D., et al., *Corrosion mechanisms of steel and cast iron by molten aluminum.* Metallurgical and Materials Transactions A, 2010. **41**(9): p. 2366-2376.

93. Rams, J., et al., *Electroless nickel coated short carbon fibres in aluminium matrix composites.* Composites Part A: Applied Science and Manufacturing, 2007. **38**(2): p. 566-575.

94. *http://www.microthermgroup.com/high/EXEN/site/adv_microthermvspyrogel.aspx*.

95. *http://zircarzirconia.com/technical-documents/thermal-conductivity-zircar-zirconia-fibrous-insulation/*.

96. Bergman, T.L., F.P. Incropera, and A.S. Lavine, *Fundamentals of heat and mass transfer*. 2011: John Wiley & Sons.

97. *https://www.ohiocarbonblank.com/index.php?file=graphitematerial_detail&url=ar-14*.

98. Uher, C., *4.3.2 Temperature dependence of thermal conductivity of graphite*, in *Thermal Conductivity of Pure Metals and Alloys*, O. Madelung and G.K. White, Editors. 1991, Springer Berlin Heidelberg. p. 430-439.

99. Leichter, H. and E. Robinson, *Fatigue Behavior of a High-Density Graphite and General Design Correlation.* Journal of the American Ceramic Society, 1970. **53**(4): p. 197-204.

100. Blackstone, R., *Radiation creep of graphite. An introduction.* Journal of Nuclear Materials, 1977. **65**: p. 72-78.

101. Winston, R., J.C. Miñano, and P.G. Benitez, *Nonimaging optics*. 2005: Academic Press.

102. Bansal, N.P. and R.H. Doremus, *Handbook of glass properties*. 2013: Elsevier.

103. Chen, Y., et al., *Non-imaging, focusing heliostat.* Solar Energy, 2001. **71**(3): p. 155-164.

104. *http://www.sunfolding.com/*.

105. Pfahl, A., *Survey of heliostat concepts for cost reduction.* Journal of Solar Energy Engineering, 2014. **136**(1): p. 014501.

106. *https://gigaom.com/2015/02/19/theres-a-new-renaissance-emerging-for-energy-innovation/*.

107. Blair, N., et al., *System advisor model, sam 2014.1. 14: General description.* NREL Rep. No. TP-6A20-61019, Natl. Renew. Energy Lab. Golden, CO, 2014: p. 13.

108. Schmitz, M., et al., *Assessment of the potential improvement due to multiple apertures in central receiver systems with secondary concentrators.* Solar Energy, 2006. **80**(1): p. 111-120.

109. *http://www.evaporatedcoatings.com/anti-reflection-coatings-for-glass*.

110. Desmarais, R. and J. Breuer, *How to select and use the right temperature sensor*. 1997: Society of Manufacturing Engineers.